Direct Probes Of The Intergalactic Medium During The Epoch Of Reionization

Hannah Fronenberg, McGill Space Institute
McGill University, Montreal
August, 2021

A thesis submitted to McGill University in partial fulfillment of the requirements of the degree of

Master of Science, Physics

Abstract

The Epoch of Reionization remains a poorly understood time in our universe's history. It is during this epoch that the first stars and galaxies formed and the intergalactic medium (IGM) became ionized by UV photons emanating from these galaxies. Observation of the 21 cm line, a hyperfine transition line of hydrogen, is a direct probe this era and would provide us with direct observations of the Universe before the formation of luminous objects, would allow us to place constraints on fundamental cosmological parameters, and would deepen our understanding of large-scale structure formation. However, there exist many challenges in making these observations a reality. At the redshifts of interest, the 21 cm line suffers from bright foreground contaminants meaning instruments need to be well-calibrated and careful foreground subtraction must be performed. These requirements are difficult to execute to high precision and without being subject to modelling biases, and as such, some have looked to use complimentary probes to bolster a 21 cm detection. This thesis explores two such methods. The first method is to make use of cross-correlations to measure a cross-spectrum instead of the 21 cm auto-spectrum. We build and end-to-end simulation pipeline which includes both instrument and foreground modelling in order to place constraints on the effectiveness of the 21 cm – [CII] cross-spectrum in estimating the 21 cm power spectrum during reionization. The second method is to turn to astrophysical probes of the IGM. We explore whether, and to what precision, the dispersion measures of high redshift fast radio bursts can reveal reionization history.

Abrégé

L'époque de réionization reste très peu comprise dans l'histoire de l'Univers. C'est à cette période que les premières étoiles et galaxies se sont formées et que l'ionisation du milieu intergalactique a eu lieu grâce aux photons émanant de ces dernières. L'observation de la raie 21cm d'hydrogène, une transition hyperfine de l'atome d'hydrogène, est une preuve directe de cette époque. Son étude précise permettra d'obtenir des observations directes de l'Univers avant la formation de ces objets lumineux. Elle permettra également d'obtenir de nouvelles contraintes sur les paramètres cosmologiques fondamentaux et d'avoir une meilleure compréhension de la formation des structures à grandes échelles. Cependant, beaucoup de problématiques persistent pour faire de ces observations une réalité. A un certain décalage vers le rouge, la raie 21cm est fortement contaminée par des composants très lumineux de premier plan. Les instruments de mesure doivent donc être calibrés et des procédés précis de soustraction de ces contaminants doivent être utilisés. Ces conditions sont difficiles à mettre en oeuvre pour réaliser des mesures de haute précision sans être soumis à des biais de modélisation. C'est pourquoi certains ont cherché à utiliser des sondes complémentaires pour renforcer la détection et l'étude de la raie 21cm d'hydrogène. Cette thèse traite deux de ces méthodes. La première réside sur l'utilisation des corrélations croisées pour mesurer le spectre croisé par rapport à un spectre seul. Nous construisons une simulation complète qui inclut à la fois l'instrument et la modélisation de l'avant-plan afin d'imposer des contraintes sur l'efficacité du spectre croisé 21 cm – [CII] pour estimer le spectre de puissance 21 cm pendant la réionisation. La deuxième méthode consiste à se tourner vers les sondes astrophysiques de l'IGM. Nous examinons si, et avec quelle précision, les mesures de dispersion des sursauts radio rapides à haut décalage vers le rouge peuvent révéler l'histoire de la réionisation.

Acknowledgements

While for many a Master's degree is simply a stepping stone, for me this degree has, in its own way, been formative. Given the current global crisis, which began at the start of my second semester at McGill and which persists to the time of this thesis' submission, this degree proved to be more challenging than anticipated. Some describe the last year as character building, but for me it has been character revealing. Despite an isolating year and a half, the character of the members of this department are such that their fervour for research and kindness in the darkest of times, permeates any zoom call, regardless of the quality of the internet connection. And so, special thanks are due.

First, to my supervisor Adrian Liu, without whom this thesis would surely not exist, and my love of cosmology not flourished. The fact that this thesis managed to come to completion and more importantly that I remain excited and motivated about my future in this field given the working conditions of this past year, is truly a testament to what a wonderful person he is. I imagine it was not easy to keep up the group's morale, but somehow Adrian did it and I am grateful. Still too, my outlook on science and the field of cosmology has been shaped by the entire department, but I would like to personally thank Robert Brandenberger, Jordan Mirocha, Saraubh Singh, Heliudson Bernando, Vahid Kamali, and really our entire cosmology group for continually teaching me not only what is to do good science, but also what it means to be a good scientist. I also owe huge thanks to my thesis examiner, Matt Dobbs, whose expertise and insight made this final version far superior to manuscript that initially landed on his desk. Michael Pagano, my academic older brother, who not only carried me through my first semesters at McGill, but also through my very first publication, I cannot thank you enough for being my mentor and friend.

To my parents who have always been my biggest supporters and closest friends, I cannot thank you enough for the education you provided me with which led me here, and for the constant support in pursuing my dreams.

Table of Contents

List of Figures

List of Tables

Chapter 1

Introduction

1.1 The Current Cosmological Climate

While theoretical advancements were well underway throughout the 20th century, there lacked certain experimental development to measure the cosmological parameters set by the Friedman, Lemaitre, Robertson, and Walker (FLRW) model and predicted by the lambda cold dark matter (ΛCDM) model. These models together assume we live in a homogeneous and isotropic universe where general relativity holds out to large scales, and that the expansion of the universe is driven by dark energy, or a cosmological constant, denoted by Λ [50, 78, 132, 157]. In addition, the universe's matter content is composed mostly of cold dark matter (CDM) which does not interact, except gravitationally, with baryonic matter [119]. During recent decades, the field of cosmology has entered what some call the era of precision measurement. Observations of the cosmic microwave background (CMB), large-scale galaxy surveys, measurements of primordial chemical abundances, gravitational lensing, and most recently, gravitational wave interferometry, has given us a clearer picture of the universe we live in [1, 14, 31, 119, 123]. Indeed, we live in a spatially flat universe dominated by a cosmological constant leading to today's accelerated expansion [120]. Our matter content is indeed dominated by dark matter, and we have constrained the age of the observable universe to 13.772 ± 0.040 Gyr [123].

Measurement of the CMB temperature power spectrum and the matter power spectrum have given us an intimate look at early moments after the Big Bang when the universe was hot and dense, and when matter and radiation were coupled in the original primordial soup. But as the universe expanded and cooled, matter and radiation decoupled and the photons streamed freely until we observed them as the cosmic microwave background. The power spectrum of these CMB photons had encoded in them not only the curvature and the composition of our universe, but the amplitude of the primordial fluctuations that served to seed all of the rich structure we observe at late times [123]. Galaxy surveys have made subsequent measurements of both the curvature and the dark energy content of the universe, independently from CMB measurements [151]. Still, the CMB can provide us with additional information. For example, still-to-be-improved B-mode polarization measurements are of particular interest. B-modes refer to the divergence-less component of CMB radiation while E-modes refer to the curl-less component. The primordial gravitational wave background can source B-mode polarization and the precise tilt of its spectrum is indicative of the early universe paradigm, whether inflationary or otherwise. Another such example is that careful analysis of the Sunyaev-Zel'dovich effect on the CMB can help us learn about large scale clustering [147]. Galaxy clusters leave a distinct fractional change on the CMB's apparent brightness through inverse Compton scattering, providing a redshift independent way to study the gas properties of these large scale overdensities.

While we have been able to learn a great deal about these early times from precision measurements, and likewise have been making observations of the local universe for millennia, the vast majority of the volume of our universe remains unexplored. In figure 1.1, the inner red, green, and yellow portion indicates redshifts at which we have performed large scale galaxy surveys. The black line at the periphery denotes CMB observations. But what about the in-between? In particular, a large gap in our understanding of large scale structure is understanding the formation of structure itself: How did the first stars and galaxies form and what were their properties? How did this first generation of galaxies change their surrounding environment? It is believed that the universe underwent a transition where the first stars' UV photons ionized the surrounding neutral hydrogen left over from recombination in the intergalactic medium (IGM). This epoch of reionization (EoR) is poorly constrained and understood, yet remains fundamental to our understanding of the evolution of our universe. It is theorised that the first stars ignited from the collapse of molecular hydrogen clouds around 100 million years after the Big Bang (i.e. $z \sim 20$). The end of this cosmic dawn would mark the beginning of reionization which would last until $z \sim 7$ when the IGM is completely ionized [94].

Despite the desire to learn about this dynamic time, how does one observe these far away sources that lie far beyond the parallax limit and far beyond the resolving limit of current generation galaxy surveys? Luckily, the universe's most abundance element, hydrogen, has the capability of helping us map out much of the unobserved universe. 21 cm cosmology aims to map out the universe's neutral hydrogen through the observation of the 21 cm photon. This photon, with emission wavelength 21 cm, is the result of a spontaneous hyperfine spin-flip transition in neutral hydrogen which occurs approximately every 11 million years. While the spontaneous transition is rare on the timescales of human laboratory experiments and has never been observed tabletop, the large volumes of cosmological surveys makes this 21 cm signal abundant. In figure 1.1, the blue cyan region denotes the redshifts at which we can observe this hydrogen line. Similar to the CMB, 21 cm cosmology can probe pre-galactic times, yet has the added benefit of being a signal that is continuously emitted so long as neutral hydrogen is around. 21 cm cosmology, therefore, aims to map out the universe in 3-dimensions, which historically has been referred to as 21 cm tomography. The 21 cm signal has already been observed at $0.057 < z < 1.12$ by the Green Bank Telescope (GBT) and the Parkes radio telescope through cross-correlations with galaxy surveys.

While 21 cm cosmology will, in due time, revolutionize the study of the epoch of reionization (EoR), there remains some hesitation as to the feasibility of making such a detection due to systematics which will be discussed at length in subsequent chapters. As such, some have looked to use complimentary probes to bolster a 21 cm detection. Two alternative methods will be explored in this thesis. The first such method is to make use of a second line that is correlated with the 21 cm line thus making it possible to measure a cross-spectrum instead of the 21 cm auto-spectrum. One such line is the ionized carbon [CII] line which has a distinct correlated signal to the 21 cm line [39]. The second such

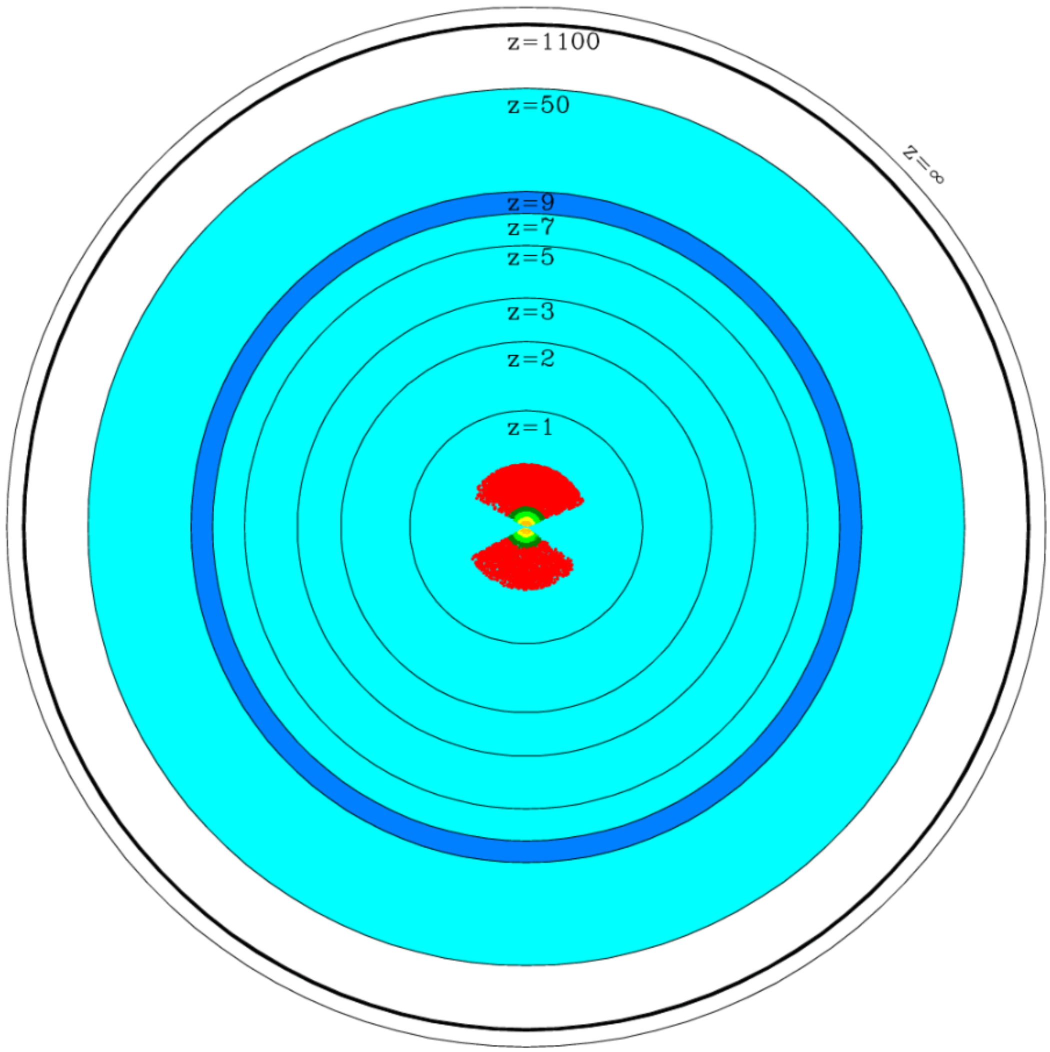

Figure 1.1: A model of the comoving volume of our universe where we are located in the center. The yellow, green, and red regions denote redshifts at which large scale galaxy surveys have been performed. The black line at the periphery denotes CMB observations at $z \sim 1100$. The light and dark blue regions denote redshifts at which 21 cm observations can be made. This figure is reproduced from Mao et al. 2008 [96].

method is to turn to astrophysical probes of the IGM such as the dispersion measure (DM) of Fast Radio Bursts (FRBs).

1.2 Roadmap

The goal of this thesis is twofold. Firstly, I build an end-to-end simulation pipeline for 21 cm and [CII] observations, including realistic foreground contaminants, in order to place constraints on the cross-spectrum of these two measurements. In theory, this cross-correlated spectrum should reduce the effects of the bright foregrounds found in 21 cm observations. Secondly, my collaborator Michael Pagano and I explored the possibility of using independent astrophysical probes of the IGM to complement 21 cm observations. FRBs, should they exist at high DM, directly probe the IGM through their dispersion delay and can in theory reveal the reionization history. The chapters are summarised as follows:

- In Chapter 2, the main observables, namely the brightness temperature of both the 21 cm field and the [CII] field are presented and discussed. In addition, a brief qualitative history of the cosmic dark ages, cosmic dawn, and the epoch of reionization is provided with commentary on how these brightness temperatures are expected to evolve through these epochs.

- In Chapter 3, the experimental status of 21 cm global signal experiments, 21 cm intensity mapping experiments, and [CII] intensity mapping experiments is presented with a specific focus on epoch of reionization related science. In addition, the fiducial surveys used in the simulation of cross-correlations are identified.

- Chapter 4 deals with introducing the mathematics of single dish instruments as well as interferometers. The fiducial surveys are also discussed and their instrument specifications are presented.

- In Chapter 5, map making, power spectra, and window functions are discussed. These are presented as analysis tools to be used in the subsequent chapter.

- Chapter 6 deals with simulating cross-correlations between 21 cm and [CII] line intensity mapping observations. Here, the components of and end-to-end simulation pipeline are presented. Each component of this pipeline was developed from the ground up and is designed simulated both instrumental effects as well as 21 cm and [CII] foregrounds in order to produces cross-spectra with error estimates. The first results of this effort are presented.

- Chapter 7 is the result of published work titled "Constraining the Epoch of Reionization With Highly Dispersed Fast Radio Bursts" [115] written in collaboration with Michael Pagano. In this work, we explore whether the DMs of FRBs are sensitive to certain reionization model parameters and whether the DMs of highly dispersed FRBs can reveal the reionization history, and to what precision. Michael and I collaborated on every aspect of this work, namely performing initial calculations, setting up the simulations, and interpreting the results.

- In Chapter 8, the main conclusions and key results of this thesis are summarized. We also reflect on the role of multiple probes in studying the EoR.

Chapter 2

The Early Universe and Its Observables

2.1 Introduction

In this chapter, the main observable of 21 cm cosmology is introduced, the brightness temperature. It is first derived and we then proceed to describing how the brightness temperature evolves as we move through different epochs. The underlying physical mechanisms responsible for changes in this signal are discussed in detail. One must always keep in mind in discussion of the 21 cm brightness temperature that this story we tell about its evolution is simply qualitative. The precise timing, duration, and details of each event that contributes to the global signal we model are unknown. There does not exist a fiducial model of cosmic dawn and reionization. We only have broad clues about certain large scale changes that must have happened in order for cosmic history to remain consistent. The precise timing and characteristics of the events discussed below must all be determined experimentally and all current predictions are heavily dependent on the model. In addition to this, the morphology of the 21 cm field during reionization is discussed.

Lastly, the physics of the [CII] line are discussed. Once again, we only have a vague qualitative story about the production of ionized carbon and the excitation of the transition. That being said, this qualitative story allows us to derive the spin temperature of [CII] and understand the general morphology of the signal.

2.2 Brightness Temperature And The Cosmic History of HI

The 21 cm transition arises from the hyperfine splitting of the ground state $1s^2S^{1/2}$ of atomic hydrogen into two. This forbidden transition is the result of the interaction between the magnetic moments of the proton and the electron [163]. When a hydrogen atom in the aligned state transitions to its anti-aligned, lower energy state, a 21 cm photon is emitted. If the converse occurs, the atom absorbs a 21 cm photon. The transition rate has been computed to high precision by Gould and includes first-order radiative corrections to the magnetic moment of the electron and the coupling of the 21 cm photon to the magnetic moment of the nucleus. It has been computed to be $A_{10} = 2.8843 \times 10^{-15}$ s^{-1} meaning the transition occurs on average every 11 million years [55]. Once again, knowing that approximately 75% of the universe's chemical abundance is hydrogen, this 21 cm signal is abundant.

This transition is often described using a quantity called the spin temperature, T_s , which is related to the relative occupancy of the two spin states

$$\frac{n_1}{n_0} = \frac{g_1}{g_0} \exp\left(\frac{h\nu_{21}}{kT_s}\right) \tag{2.1}$$

where n_1 is the number density of hydrogen atoms in the excited hyperfine state, n_0 is the number density of hydrogen atoms in the ground hyperfine state, $g_1 = 1$ and $g_0 = 3$ are the statistical weights, h is Planck's constant, k is Boltzmann's constant, and ν_{21} = 1420.406 MHz is the rest frequency of the 21 cm line. Equation 2.1 is nothing more than the ratio of the number hydrogen atoms in the excited to the number of hydrogen atoms in the ground state which can be described by a single variable, the spin temperature.

Now, this transition does not occur in isolation, but rather occurs on the cosmological stage, meaning that rather than measure T_s directly, it is measured with respect to the CMB. Therefore, we proceed to define the brightness temperature which is the temperature deviation from the CMB due to either absorption or emission of the 21 cm line.

$$T_b(\hat{\mathbf{r}}, z) = \left[1 - e^{-\tau_{21}(\hat{\mathbf{r}}, z)}\right] \frac{T_s(\hat{\mathbf{r}}, z) - T_\gamma(z)}{1 + z} \tag{2.2}$$

where τ_{21} is the optical depth across the 21 cm line at redshift z and T_γ is the temperature of CMB photons. As one can see, the first term in the square brackets of this expression corresponds to the relative emission and the second is the relative absorption of the 21 cm line, relative being to the CMB. It is the interplay between these two terms that dictate whether there exists a signal.

Since there exists a one-to-one mapping between redshift and frequency, namely

$$1 + z = \frac{\nu_{\rm emit}}{\nu_{\rm obs}} \tag{2.3}$$

and since we indeed tune our telescope to a particular frequency rather than a redshift, we are motivated to find a frequency dependent formula for T_b. This can be accomplished by, firstly, writing down the equation for the optical depth τ_{21}. This optical depth is the optical depth across the 21 cm line of a patch of the IGM. The optical depth is the following,

$$\tau_{21} = \frac{3\hbar c^3 A_{10}}{16k} \frac{\nu_{\rm obs}}{\nu_{21}^3} \frac{x_{HI} n_H}{dv_{||}/dr_{||} T_s} \tag{2.4}$$

where $\hbar$ is the reduced Planck's constant, $\nu_{\rm obs}$ is the observed frequency, $dv_{||}/dr_{||}$ is the gradient of the proper velocity along the line of sight with respect to the line of sight distance, n_H is the number density of atomic hydrogen whether neutral or not, and x_{HI} is neutral fraction of atomic hydrogen [79]. I would like to make a quick note on the neutral fraction and its relationship to the ionized fraction x_{HII} and the IGM electron density n_e. The neutral fraction is defined as the ratio of the number density of neutral atomic hydrogen to the number density of any form of atomic hydrogen, $x_{HI} = n_{HI}/n_H$. Likewise the ionized fraction is defined as the ratio of the number density of ionized atomic hydrogen to the number density of any form of atomic hydrogen, $x_{HII} = n_{HII}/n_H$. Some take as a proxy for n_{HII}, simply the number density of electrons in the IGM since every ionized hydrogen nucleus has an electron counterpart. It should be noted that while this approximation holds for the high redshift observations we are interested in, helium reionization at $z \sim 2$ does increase the electron number density at late times. We will return to this discussion in Chapter 7.

Now, plugging equations 2.3 and 2.4 into equations 2.5, and Taylor expanding to first order [1] we obtain,

$$T_b(\hat{\mathbf{r}}, \nu_{\text{obs}}) = \frac{3\hbar c^3 A_{10}}{16k} \frac{\nu_{\text{obs}^2}}{\nu_{21}^4} \frac{x_{HI} n_H}{dv_{||}/dr_{||}} \left(1 - \frac{T_s(\hat{\mathbf{r}}, \nu_{\text{obs}})}{T_\gamma(\nu_{\text{obs}})}\right). \tag{2.5}$$

In figure 2.1, the top panel displays a lightcone of 21 cm brightness temperature and the middle panel displays the global sky-averaged 21 cm brightness temperature across $7 \leq z \leq 90$. There are many notable features which are all a result of the underlying physics. In the following few subsections we will take a walk through this cosmic timeline and dive into what physics are at play. We will comment on both the 21 cm fluctuations and the global signal.

2.2.1 The Dark Ages ($20 < \mathbf{z} \leq 1100$)

At recombination, $z = 1100$, baryons and photons decoupled and electrons and baryons combined to create the universe's first atoms. Still, there remains a small fraction of free electrons for photons to scatter off of which leads to the coupling of baryon and photon temperatures. As the universe expands, the scattering rate decreases until at $z \sim 300$, the rate becomes so rare that the photon and baryon temperatures decouple. This decoupling results in the Baryon temperature cooling at its typical rate which is much faster than the cooling rate of photons. Since there exists collisional coupling between the kinetic gas temperature and the spin temperature, the spin temperature also cools leading to a brightness temperature absorption signal which is visible at $30 < z < 80$. This can be seen in figure 2.1 in the top two panels on the high-z right hand side.

This period where there exists an absorption signal is of particular cosmological interest. Most notably, Silk damping erases the small scale information in CMB spectra [138]. These small scales now become directly observable in 21 cm all the way down to the Jeans scale and the T_b fluctuations effectively trace the matter power spectrum up to high wavenumber modes. Additionally, since there do not yet exist luminous objects, first order per-

[1] This Taylor expansion is justified since the optical depth in the exponent has been measured to be $\lesssim 4$ [79].

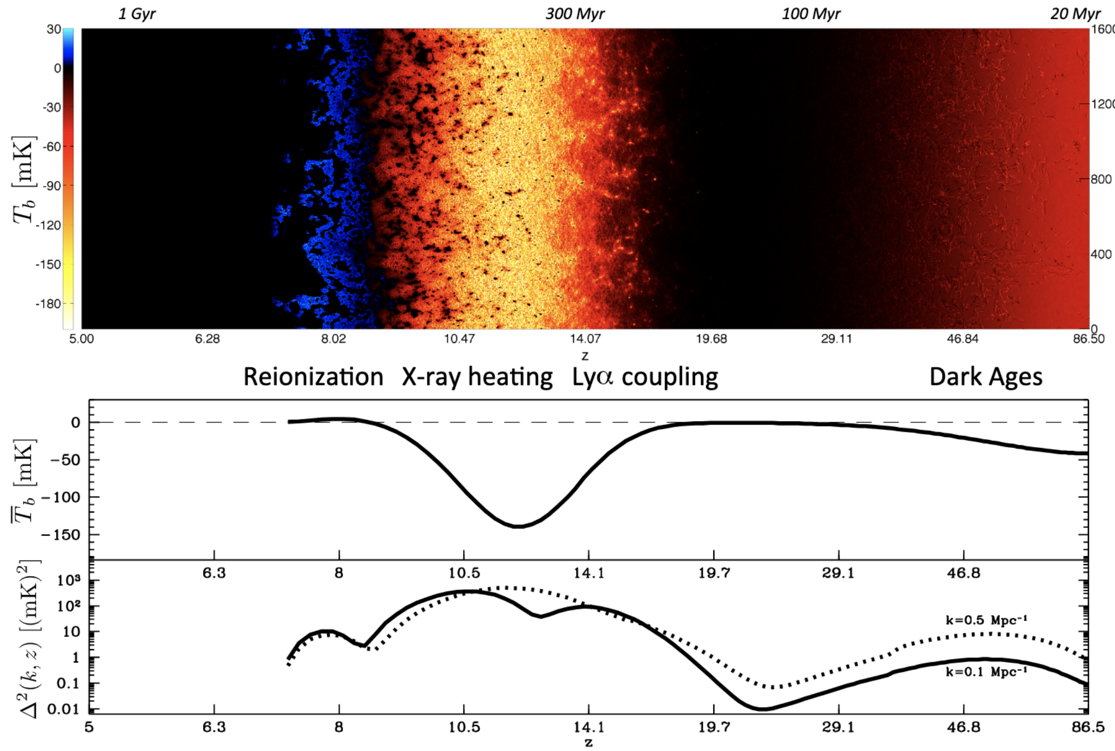

Figure 2.1: Displayed here is a simulated 21 cm signal from $7 < z < 90$. The top panel shows the 2D slice of a 3D lightcone of the 21 cm brightness temperature field. The x axis shows the evolution across different redshifts and the compounding age of the universe is on the top horizontal axis. The middle panel displays the global 21 cm signal as a function of redshift. This was computed by taking the average brightness temperature for each slice of the lightcone at each redshift. The bottom panel shows the dimensionless power spectrum as a function of redshift and the modes $k = 0.5\mathrm{Mpc}^{-1}$ (dotted) and $k = 0.1\mathrm{Mpc}^{-1}$ (solid) are shown. This figure is reproduced from [83].

turbation theory holds and these small scales are easy to model in contrast to the complex non-linear modelling needed for other probes [136, 152]. This clean probe of the matter field would allow us to study non-Gaussianity, to measure the small scale properties of dark matter, to improve constraints on the neutrino mass, to measure the primordial power spectrum, and to detect primordial gravitational wave signatures [88, 96, 107].

Despite this being a period full promise, the 21 cm line at these redshifts gets redshifted into the ultra-low frequency range. The observed frequencies lie between $\sim 4 - 40$

MHz. Not only would this require extremely long baselines to achieve the angular resolution required to observe the relevant features on the sky, but the ionosphere becomes increasingly opaque to frequencies below ~ 30 MHz and can cause distortions at frequencies above but still close to this limit. There has been a sustained effort to conduct interferometric observations at these frequencies [111], although calibration becomes more difficult, and certain phenomena like Faraday rotation become increasingly relevant and complicated to model. While there is still hope of doing low-frequency science on Earth, there are growing initiatives to develop space-based experiments, either in orbit or on the far side of the moon, in order to overcome these limitations [15].

But like all good things, at $z \sim 30$, this absorption period comes to an end. As expansion continues, collisions between hydrogen atoms become rare and the kinetic and spin temperatures decouple. The spin temperature rises and reaches the CMB temperature. Since there is no longer a temperature contrast from the CMB, the 21 cm signal disappears. This can be seen in figure 2.1 as we move along the cosmic timeline toward the left. In the top panel we see a dark band and in middle panel the average brightness temperature flattens to $T_b = 0$.

2.2.2 Cosmic Dawn ($12 \leq \mathbf{z} \leq 20$)

At $z \sim 20$, the first luminous objects form, and the complex small scale astrophysics we avoided during the dark ages now prohibits us from probing the high k modes of those fundamental cosmological fields. Cosmic dawn, however, provides us with the opportunity to learn about this first generation of stars and galaxies. Initially, Lyman alpha (Lyα) photons are produced from the first stars which travel through the IGM and excite neutral hydrogen atoms to the $n = 2$ state. When these atoms decay back down to the ground state, they may find themselves in a different hyperfine state leading to increased 21 cm emission. In addition, due to the large scattering cross section of the Lyα photon, the gas temperature once again couples to the spin temperature. Since the gas temperature has continued to cool, so too will the spin temperature, leading to the start of a deep well in the global signal as can be seen at $z \sim 12$ in the middle panel of figure 2.1.

The IGM continues to be saturated with Lyα flux and as star formation becomes more efficient, even higher energy photons begin to be emitted from these first stars. These photons are now energetic enough to ionize, excite, and heat the neutral hydrogen and helium. This phase of X-ray heating increases the gas temperature and consequently the spin temperature leading to an emission signal rather than one of absorption. Because astrophysical sources causing the heating are clustered, there are significant spatial fluctuations in the 21 cm line. These x-ray sourced fluctuations will persist until the entire IGM is heated. Once again, as mentioned in section 2.1, since there is no concordance model for these epochs, the precise order and timing of these various heating events is unknown. We have a vague qualitative picture of what must have happened and only through observation will we be able to obtain a detailed account.

2.2.3 The Epoch of Reionization ($5 \leq z \leq 12$)

The end of cosmic dawn marks the beginning of reionization. Stars now efficiently produce UV photons which ionize their surrounding medium. This leads to very distinct features in the 21 cm field. A sponge-like structure starts to form where small ionized regions form around galaxies while the rest of the IGM remains neutral and continues to emit 21 cm photons. These bubbles grow as a function of redshift since more and more of the IGM becomes ionized. Finally, the bubbles become so large that they all join together leaving an entirely ionized IGM where little 21 cm signal exists. Figure 2.2 displays 2D slices of the temperature brightness field as a function of redshift simulated on `21CMFAST` [99].

This epoch is truly a mystery and there are many questions that remain. When did reionization begin? When did it end? What was the rate of reionization as a function of redshift? What sources were most responsible; stars, active galactic nuclei, or something more exotic? The answers to all of these questions characterise our reionization history. In figure 2.3, recent constraints on the reionization history are shown, parametrized by the neutral fraction. As can be seen in the figure, the start of reionization is constrained mostly by CMB measurements, while mid to end of reionization limits could be greatly improved. The scarcity of precision measurements during this epoch indicates that there is still much to learn about this time, and that innovative probes will be required.

2.2.4 Low Redshifts ($0 \le z \le 5$)

While it might at first glance seem impossible to make any sort of 21 cm detection after reionization, the universe continues to surprise us. Neutral hydrogen within galaxies is self-shielded from ionizing photons [142, 161]. These dense neutral regions continue to emit the 21 cm signal from galaxies instead of from the IGM. The distribution of this hydrogen can be mapped using line intensity mapping (LIM) techniques much like the ones used to measure the EoR. The goals of such experiments are to measure the matter power spectrum which is a dynamical probe that provides us with information about structure growth. In addition, LIM can allow us to measure the correlation function which reveals the baryon acoustic oscillation (BAO) scale which is the imprint of sound waves that propagated through the primordial plasma. This scale acts as a standard ruler and is therefore of particular astrophysical and cosmological interest. BAO measurements are traditionally done using galaxy surveys which are tedious, time consuming and experimentally challenging because each galaxy must be individually resolved, requiring very small angular resolution to probe out to $z \sim 5$. Hydrogen intensity mapping will allow us to trace the distribution of galaxies without needing to resolve galaxies which is a significant advantage. Experiments that are currently or planning on making these observations include the Canadian Hydrogen Intensity Mapping Experiment (CHIME, [3]), the Hydrogen Intensity and Real-time Analysis eXperiment (HIRAX, [111]), the Canadian Hydrogen Observatory and Radio-transient Detector (CHORD, [155]), Parkes, and the Square Kilometer Array (SKA, [36]), to name a few. For the interested reader, a full list of experiments can be found in [13].

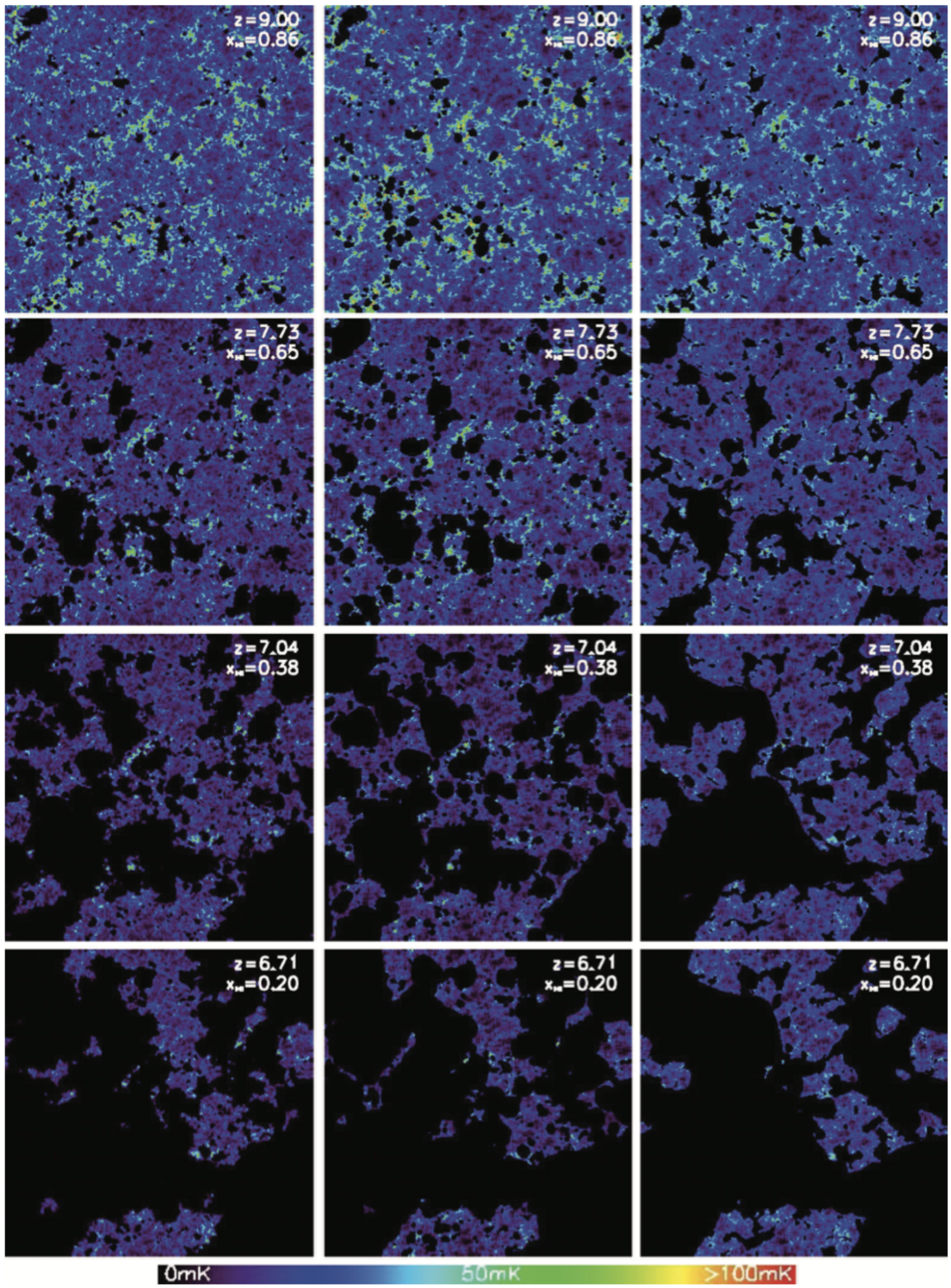

Figure 2.2: Plotted in this figure are the brightness temperature fluctuations, δT_b at redshift slices $z = \{9, 7.73, 7.04, 6.71\}$. From left to right, the slices are generated from the hydrodynamic simulation, DexM, MF07, and 21cmFAST. As reionization marches on, more ionized bubbles form until the black ionized patches dominate the field. This figure is reproduced from Mesinger et al. 2011 [99].

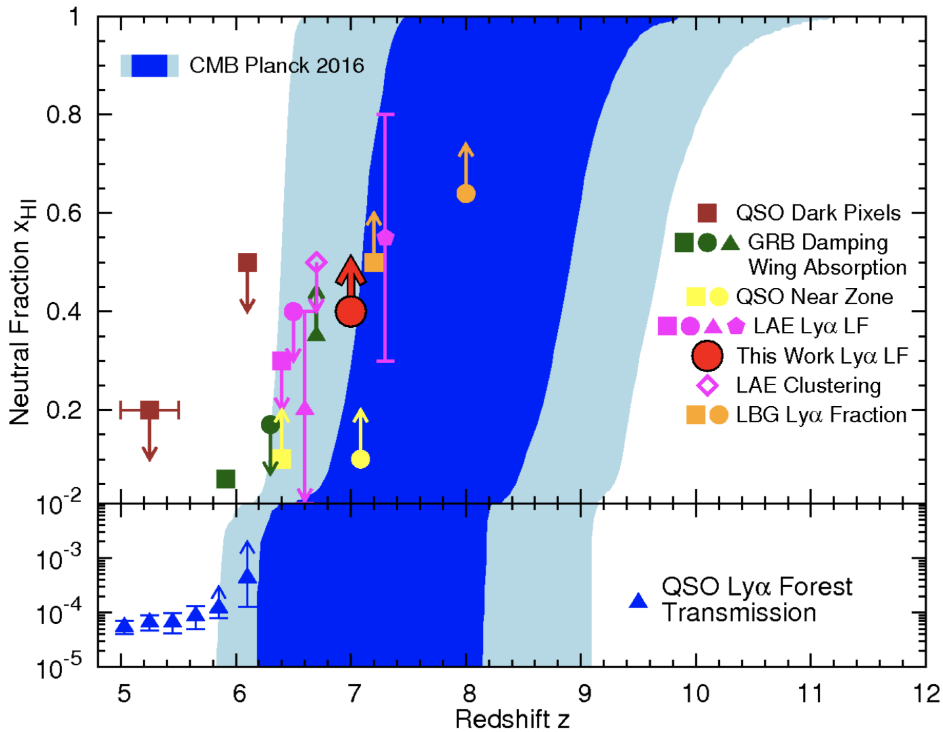

Figure 2.3: Cosmic reionization history constrained by different probes. The reionization history is parametrized by the neutral fraction as a function of redshift. Reproduced from Ota et al. 2017 [114].

2.3 The Morphology Of The 21 cm Field

Throughout the discussion in the previous section, were allusions to how the HI field traced the underlying matter field. As mentioned, before star formation begins, the HI field traces the matter field as there are no ionizing sources. However, throughout the cosmic dark ages and the epoch of reionization the HI field evolves and the precise nature of this evolution is related to the physics of star formation such as Lyman-α emission, X-ray heating, and of course, ionization by UV photons. As such, the HI field could evolve, relative to the matter field, in several different ways depending on the timing and efficiency of the processes mentioned. In particular, we are interested in how the dominant driver of reionization affects the correlation between the HI field and the matter field. Of course this correlation could be (and most probably is) complex and scale and redshift dependent, but at the extremes we can consider positively correlated and negatively correlated reionization.

Firstly, negatively correlated reionization corresponds to the more physically intuitive scenario where UV photons emerging from galaxies, ionize the immediate environment. As reionization continues, the IGM continues to be ionized further and further away from galaxies until the entire IGM is ionized. This is referred to as "inside out" reionization. In this scenario, areas of matter over-density are under-dense in HI at the beginning of reionization and areas of low matter density remain dense in HI until the end stages of reionization. This scenario is typically taken to be the fiducial model of reionization in most simulations.

Conversely, positively correlated reionization occurs when the deep IGM is initially ionized while the regions near galaxies remain neutral. This process is driven by X-ray heating where X-ray photons are emitted from galaxies and scatter through the IGM until they become UV ionizing photons. In this case, low density regions are the first to be ionized leaving high density regions dense in HI at the start of reionization. As reionization presses on, neutral hydrogen closer and closer to galaxies becomes ionized. This scenario is often referred to as "outside in" reionization. It should be noted that the relationship between the brightness temperature field and the matter field is more complex and while ionized regions do correspond a brightness temperature of zero, outside in and inside out reionization affect the brightness and morphology of the brightness temperature field in unique ways. A more fruitful discussion of these details can be found in [116].

In reality, all of these processes are working in tandem and it remains unknown what the dominant mechanisms of reionization are nor precisely how they evolve as a function of redshift. A more quantitative discussion of density correlations can be found in section 7.2.2. It is worth stating, however, that at low redshifts, the HI line is positively correlated with the density field since self-shielded HI in galaxies remains neutral throughout the reionization process.

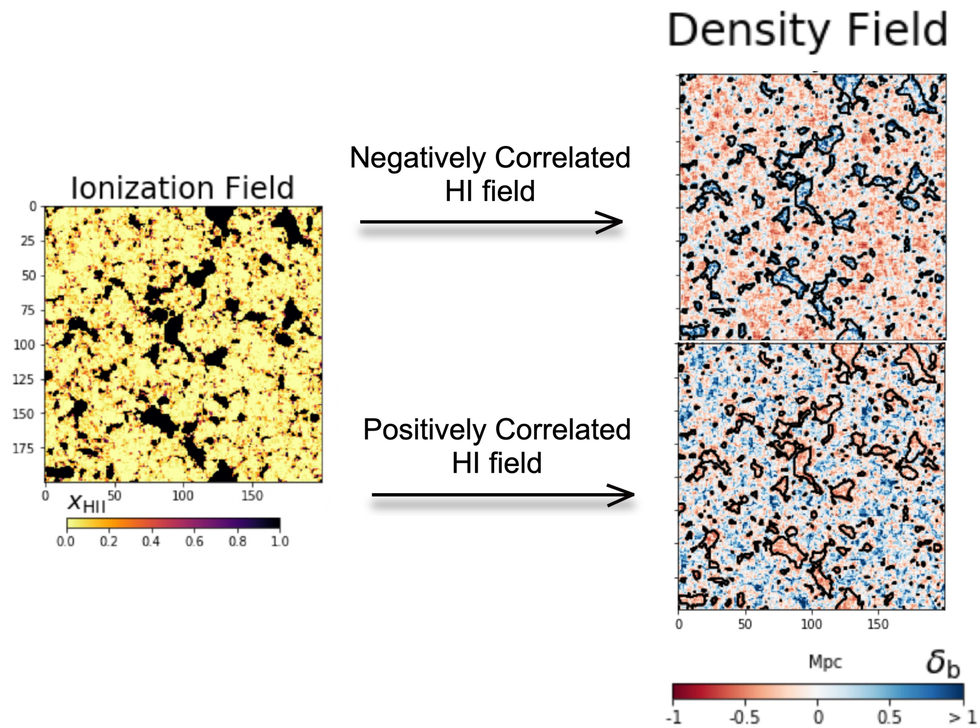

Figure 2.4: Depicted here is the correlation between the ionization field and density field. Following the negatively correlated HI field arrow, it is clear that high density regions in blue, correspond to ionized regions in black. Therefore the neutral fraction is negatively correlated with the density field. Similarly, following the positively correlated HI field arrow, the low density regions in red now correspond to the ionized regions in black. This diagram has been adapted from Pagano & Liu 2020 [116].

2.4 [CII] emission

In addition to the 21 cm line, there exist other lines that can map out large scale structure and that evolve in physically significant ways. For the work done in this thesis, the ionized carbon [CII] line is of notable interested because it is spatially correlated with the 21 cm line. Carbon is first produced in our universe by Population III (Pop III) stars, the first generation stars which are primarily hydrogen burning. Carbon has an ionization energy of 11.26 eV which is below that of hydrogen, meaning that neutral carbon can be more easily ionized. Once ionized, either in the interstellar medium (ISM) or in the IGM,

[CII] can undergo the spin-orbit coupling transition ${}^2P_{3/2} \rightarrow {}^2P_{1/2}$, emitting a photon of wavelength 157.7 μm. This transition can occur by 3 different mechanisms: collisional emission, spontaneous emission, and stimulated emission [5, 145].

Within galaxies, the main mechanism for emission is collision with ionized gas in the ISM. The electron density needed to trigger collisional excitation is less than 100 cm^{-3} while the number needed to trigger an excitation in hydrogen is between 1000 and 10,000 cm^{-3} [95], meaning that electrons more frequently excite CII ions than HI atoms [77, 145]. In the more diffuse IGM, radiative processes are primarily responsible for CII line emission. The excitations here are due to spontaneous emission and stimulated emission from collisions with CMB photons. While emission of the CII line occurs both in the ISM and the IGM, the spin temperature of the line alone is not the observable of interest. Likewise with the 21 cm line, we seek to observe the difference in temperature between the CII spin temperature and the CMB photon temperature. In figure 2.5, the left plot shows the spin temperature of CII and the CMB photon temperature in the IGM as a function of redshift. As is clearly shown, at high redshift there is no observable brightness temperature from CII in the IGM. Conversely, on the right plot, even with the most conservative electron number density and kinetic temperature of the electrons, there is a clear surplus in temperature from the [CII] line. Therefore, the CII brightness temperature traces galaxies, and is therefore anti-correlated with the 21 cm line in the inside out scenario, and is positively correlated with the 21 cm line in the outside in scenario. This correlation can be exploited for foreground removal and will be the focus of chapter 6.

2.4.1 [CII] Spin Temperature

In this section, we will derive the spin temperature plotted in Figure 2.5. Similar to the 21 cm line, we begin by writing down the statistical balance equation,

$$\frac{n_1}{n_0} = \frac{B_{01} I_{\nu_{10}} + n_e C_{01}}{B_{10} I_{\nu_{10}} + A_{10} + n_e C_{10}} = \frac{g_1}{g_0} \exp\left(\frac{h\nu_{10}}{kT_{s,10}}\right) \tag{2.6}$$

where 1 denotes the higher total angular momentum state and 0 denotes the lower total angular momentum state. B_{01} and B_{10} are the stimulated absorption and emission coef-

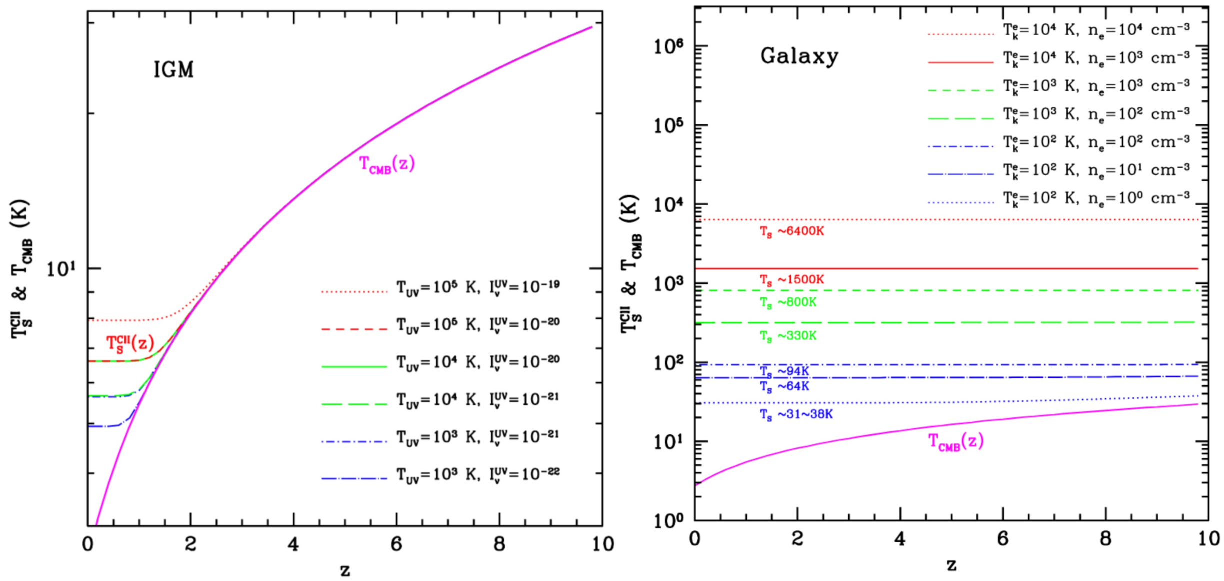

Figure 2.5: (Left) The IGM [CII] spin temperature is plotted along with the CMB photon temperature as a function of redshift. The red, green and blue lines denote different UV colour temperatures and UV background intensities which affect the rate of UV pumping. (Right) The galactic [CII] spin temperature is plotted along with the CMB photon temperature as a function of redshift. Here the red green and blue lines indicate different electron number densities and kinetic temperatures affection the collision rate and therefore the spin temperature. This figure is adapted from Gong et al. 2011 [54].

ficients respectively, $I_{\nu_{10}}$ is the intensity of the CMB at the transition frequency, ν_{10}, A_{10} is the spontaneous emission coefficient, n_e is the electron number density, and C_{01} and C_{10} are the excitation and de-excitation collision rates respectively. The rightmost portion of the equality contains the statistical weights $g_1 = 4$ and $g_0 = 2$, and the spin temperature of the transition T_s.

Now, the collisional rate can be written in the following way [113,144,148],

$$C_{01} = \frac{8.629 \times 10^{-6}}{g_0 \sqrt{T_k}} \gamma_{01} \exp\left(\frac{-h\nu_{10}}{kT_k}\right) \tag{2.7}$$

where now we have introduced T_k, the kinetic temperature of the electrons and γ_{01} the effective collision strength.

Using Einstein's relations, namely $g_0 B_{01} = g_1 B_{10}$ and $A_{10} = (2h\nu^3/c^2)B_{10}$ and the collisional balance equation,

$$\frac{C_{01}}{C_{10}} = \frac{g_1}{g_0}\exp\left(\frac{h\nu_{10}}{kT_{k,10}}\right) \tag{2.8}$$

and plugging them into equation 2.6, we obtain the equation for the spin temperature of the CII transition,

$$\frac{h\nu_{10}}{kT_s} = \log\left\{\frac{A_{10}[1 + I_{\nu_{10}}c^2/2h\nu_{10}^3] + n_e C_{10}}{A_{10}(I_{\nu_{10}}c^2/2h\nu_{10}^3) + n_e C_{10}\exp(-h\nu_{10}/kT_k)}\right\}. \tag{2.9}$$

Some references also include, in addition to spontenatous and stimulated emission and collisional emission, emission from UV pumping. This is a process by which UV photons produced by the first high redshift galaxies can excite CII ions from the energy levels, $2s^2 2p\ ^2P_{1/2}$ to $2s2p^2\ ^2D_{3/2}$ and $2s^2 2p\ ^2P_{3/2}$ to $2s2p^2\ ^2D_{3/2}$ [48, 57, 164]. The excited ion then proceeds to de-excite $^2D_{3/2} \to {}^2P_{3/2} \to {}^2P_{1/2}$ and the [CII] line is emitted. This mechanism, however, is subdominant in both the ISM and the IGM at high redshifts so it is omitted from the derivation of T_s here. For those interested in reading about UV pumping in more detail, please refer to [54].

Taking equation 2.9, we can make a first approximation in the ISM case. We will assume that the main excitation mechanism is through collision with electrons and proceed to writing the spin temperature for the ISM in the following way,

$$\frac{h\nu_{10}}{kT_s} \sim \log\left\{\frac{n_e C_{10}}{n_e C_{10}\exp(-h\nu_{10}/kT_k)}\right\} \tag{2.10}$$

$$\sim \log(1) - \log(\exp(-h\nu_{10}/kT_k)) \tag{2.11}$$

$$\sim h\nu_{10}/kT_k \tag{2.12}$$

$$T_s \sim T_k. \tag{2.13}$$

Therefore we can clearly see that in the ISM the spin temperature is approximately the electron kinetic temperature which is larger than the CMB temperature during reionization. For reference, the CMB temperature at $z = 8$ is $\sim 29K$ and a conservative kinetic temperature is $\sim 1000K$.

If we now make an approximation for the IGM and take only spontaneous and stimulated emission to be significant we can write,

$$\frac{h\nu_{10}}{kT_s} \sim \log\left\{\frac{A_{10}[1 + I_{\nu_{10}}c^2/2h\nu_{10}^3]}{A_{10}(I_{\nu_{10}}c^2/2h\nu_{10}^3)}\right\} \tag{2.14}$$

$$\sim \frac{1 + c^2/2h\nu_{10}^3(2h\nu_{10}^3/c^2\frac{1}{exp(h\nu_{10}/kT_{CMB})+1})}{c^2/2h\nu_{10}^3(2h\nu_{10}^3/c^2\frac{1}{exp(h\nu_{10}/kT_{CMB})+1}} \tag{2.15}$$

$$\sim \frac{1 + 1/(exp(h\nu_{10}/kT_{CMB}) + 1)}{1/(exp(h\nu_{10}/kT_{CMB}) + 1)} \tag{2.16}$$

$$\sim \log(exp(h\nu_{10}/kT_{CMB})) + \log\left(\frac{1}{exp(h\nu_{10}/kT_{CMB})}\right) - \log\left(\frac{1}{exp(h\nu_{10}/kT_{CMB})}\right) \tag{2.17}$$

$$\sim h\nu_{10}/kT_{CMB} \tag{2.18}$$

$$T_s \sim T_{CMB} \tag{2.19}$$

In the IGM, the spin temperature is approximately the CMB photon temperature and there is no observable [CII] line emission. Once again, these details are summarized in Figure 2.5.

In this chapter we derived the brightness temperature of both the 21 cm line and the [CII] line. In addition, we presented a brief history of the cosmic evolution of the 21 cm brightness temperature. During the epoch of reionization, the morphology of the 21 cm field, whether inside out or outside in, will dictate how these two probes are correlated. This correlation can be exploited in order to extract signals from these otherwise heavily contaminated probes. This technique is subject of chapter 6. In the next chapter, the current experimental status of 21 cm and [CII] experiments will be presented.

Chapter 3

The Experimental Status of 21 cm and [CII] LIM

3.1 Introduction

In this chapter we will go over the current and upcoming experimental status of 21 cm cosmology and [CII] line intensity mapping (LIM) experiments. The 21 cm experiments are divided into two categories: global signal experiments and intensity mapping experiments. Since the work done in this thesis is focused on detecting the spatial fluctuations of the 21 cm brightness temperature signal, we will only take a brief look at global signal experiments. In addition, all the experiments discussed in this chapter are ones with cosmic dawn and EoR windows. Low redshift hydrogen mapping experiments have been successfully underway, but unfortunately are beyond the scope of this thesis. That being said, the simulation pipeline presented in Chapter 6 can be used to model experiments at any redshift. For a full list of hydrogen intensity mapping experiments, the reader is directed to Sections 4 and 15 of Liu & Shaw 2020 [83]. For readers who are interested in medium to low redshift [CII] intensity mapping, they are directed to Section 3.3 of Kovetz et al. 2017 [71].

3.2 21 cm Global Signal Experiments

The first category of experiments is global signal experiments. This category aims at detecting the all-sky averaged brightness temperature as a function of redshift. This averaging is done over all angular directions on the sky of each redshift bin. As mentioned previously in section 2.2.2, there is expected to be a significant cosmic dawn signal, a large cavity, in the $T_b(z)$ plot. The depth, width, and placement of the absorption feature along the redshift axis probes how and when energy was injected into the IGM. As mentioned in the previous chapter, when the first stars ignited, X-ray heating and Lyα coupling inject energy into the IGM.

To date, only one experiment has claimed a cosmic dawn detection. The Experiment to Detect the Global Epoch of reionization Signature (EDGES, [9]) purports a detection of the absorption trough characteristic of cosmic dawn. This detection is of considerable scientific interest because it veers drastically from the expected signal. The trough, centered at 78 MHz, is both deeper and narrower than modelling has suggested it should be. The location along the frequency axis, and the narrowness of the trough suggests that star formation would have had to have happened far more rapidly than previously expected [103]. It has been suggested that the unexpected depth of the tough, that is the large temperature contrast between T_b and T_γ, is due to one of two physical scenarios: (1) There exists an undetected population of radio sources that increase the background temperature relative to the spin temperature [40, 41, 45, 46, 62, 137]; (2) There exists exotic physics that is allowing the spin temperature to cool faster than the adiabatic cooling rate of a gas [4, 19, 20, 24, 29, 44, 59, 64, 72, 73, 76, 104, 106, 108, 109, 133, 135, 141]. Of course, this trough could be a result of both effects acting simultaneously.

While the thought of new astrophysical objects and exotic physics is exciting to many, some do not share this view. Many in the field have criticised the experiment and believe that this is a false detection due to the improper treatment of systematics or fallacies in the EDGES analysis methods [10, 11, 58, 62, 139]. The challenges lie in the fact that there is no way to calibrate such an instrument on the sky and we thus rely on lab measurements to characterize the instrument. In addition, spectrally smooth foreground models are assumed in order to remove foreground contributions. Luckily, additional global signal experiments are either underway or are in the planning stages. These experiments aim to confirm or disprove the EDGES signal. These experiments include Shaped Antenna measurement of the background Radio Spectrum (SARAS , [140]), Probing Radio Intensity at high-z from Marion experiment (PRIzM, [122]), Large-aperture Experiment to Detect the Dark Ages (LEDA, [129]), Radio Experiment for the Analysis of Cosmic Hydrogen (REACH, [32]), Sonda Cosmológica de las Islas para la Detección de Hidrógeno Neutro (SCI-HI , [156]), Broadband Instrument for Global HydrOgen ReioNisation Signal (BIGHORNS, [143]), and Dark Ages Radio Explorer (DARE, [16]). The coming decade will see much progress in this field.

3.3 21 cm LIM and Tomography

The second category of 21 cm experiments are LIM or tomography experiments which aim at mapping out spatial fluctuations of the 21 cm brightness temperature over the course of reionization. 21 cm imaging is, however, still a distant goal and most current generation experiments aim to measure the 21 cm power spectrum. Like global signal experiments, this remains a challenge due to bright foreground contaminants that are 4–5 orders of magnitude brighter than the 21 cm brightness temperature. These foregrounds include galactic synchrotron emission, Bremsstrahlung emission, radio point sources, and radio frequency interference (RFI). Challenges aside, intensity mapping experiments allow us to acquire information that is simply not accessible in global signal experiments. For example, the ionization field is imprinted in the spatial fluctuations of the brightness temperature, meaning intensity mapping can allow us to infer the average ionized bubble size which is indicative of the dominant sources of reionization [97].

Currently, no experiments have claimed a detection but many have now released upper limits on the 21 cm power spectrum. The Murchison Widefield Array (MWA, [8]), the Giant Metrewave Radio Telescope (GMRT, [66]), the Donald C. Backer Precision Array for Probing the Epoch of Reionization (PAPER, [118]), the LOw Frequency Array (LOFAR, [154]), and most recently the Hydrogen Epoch of Reionization Array (HERA, [34]), have all placed upper limits on the 21 cm power spectrum. The Square Kilometre Array (SKA, [36]), is an upcoming experiment that is expected to tackle many science cases with improved observations including EoR and post-EoR related cosmology. Experiments like MWA and HERA have also planned instrument upgrades which, along with SKA, may allow them to make high-significance detections and more precisely diagnose systemics. For the remainder of this thesis, HERA will be used as the fiducial 21 cm survey in Chapter 6 and a more detailed discussion of this experiment will ensue in the following chapters.

3.4 [CII] LIM

While the above-mentioned experiments aim at detecting the 21 cm auto-spectrum, some in the field have become increasingly skeptical about the reliability of such a detection and many advocate for detection confirmation through cross-correlations. The [CII] line can be cross-correlated with the 21 cm line. Similar to 21 cm LIM, [CII] LIM experiments aim to map out the spatially fluctuating [CII] brightness temperature. These observations are done at the millimeter and sub-millimeter wavelengths and therefore do not face the same degree of diffuse foreground contaminants as radio interferometric observations. Still, [CII] observations suffer from line interlopers, low redshift transitions that redshift to the same observed frequencies as the high redshift [CII] transition. Therefore, [CII] experiments also benefit from cross-correlations. There are currently no active high redshift [CII] intensity mapping experiments and consequently, no claimed detections. To date, three high redshift [CII] LIM experiments are in development. The CarbON CII line in post-rEionisation and ReionisaTiOn epoch (CONCERTO, [25]), the Cerro Chajnantor Atacama Telescope-prime (CCAT-prime, [2]), and the Tomographic Ionized carbon intensity Mapping Experiment (TIME, [30]) all aim to detect the ionized carbon line during the epoch of reionization. For the remainder of this thesis, CCAT-prime will be used as the fiducial [CII] survey in Chapter 6 since it has the largest redshift overlap with HERA. This is depicted in figure 3.1 below.

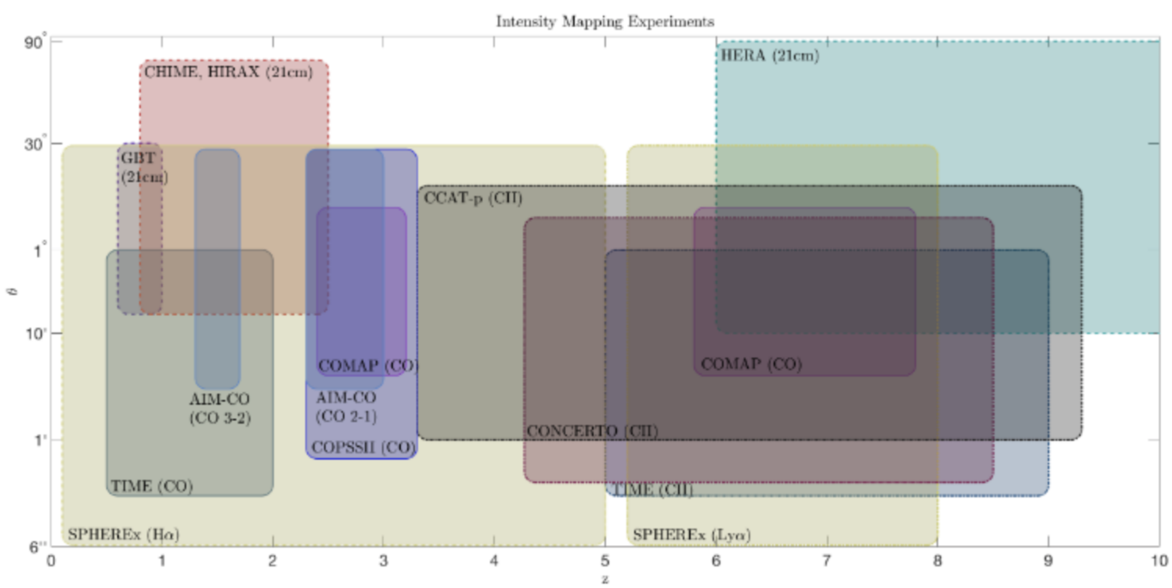

Figure 3.1: This figure displays a subset of current and upcoming intensity mapping experiments. The horizontal axis indicates the redshift and the vertical axis indicates the best resolution in arcminutes and total sky coverage in degrees. Notice how CONCERTO, CCAT-prime and TIME, all have considerable z overlap with HERA. This figure is reproduced from Kovetz et al. 2017 [70].

Chapter 4

Radio and Sub-Millimeter Astronomy

4.1 Single Dish Telescopes

The first category of instrument we will cover is the single dish telescope. In many cases, this instrument consists of a single antenna mounted on a reflecting dish which focuses the incoming radiation to the antenna feed. The resolution of single dish antennas are characterized by the primary beam and in the ideal observational scenario, the beam is accurately modelled. However, as a rule of thumb, the resolution of a single dish telescope is roughly equivalent to the full width half maximum (FWHM) of the primary beam of the dish, assuming the dish has a Gaussian beam. Therefore, for a dish of diameter D observing at wavelength λ, the diffraction limited angular resolution is,

$$\theta \sim 1.22 \frac{\lambda}{D} \tag{4.1}$$

which is the minimum spatial resolution of the telescope. Therefore, at a given fixed observing wavelength, larger dishes have better spatial resolution than smaller dishes.

In addition to resolution, an antenna is also characterised by its point source sensitivity, which is the minimum signal the telescope can detect above a certain signal-to-noise threshold in a particular direction, or rather, at a particular point on the sky. It is defined as the ratio between the source temperature and the rms noise,

$$SNR_{source} = \frac{T_{source}}{\sigma_T}. \tag{4.2}$$

The source temperature can be written in the following way,

$$T_{source} = \frac{A_e S_{\nu,source}}{2k} \tag{4.3}$$

where the effective collecting area, A_e, is defined as the output spectral power of the antenna, in response the total flux from an unpolarized point source with flux density $S_{\nu,source}$. Therefore, A_e, is the power seen by the instrument. ν is the observed frequency and k is the Boltzmann constant. The rms noise can be written in terms of the system temperature T_{sys}, using the radiometer equation,

$$\sigma_T = \frac{T_{sys}}{\sqrt{\delta\nu t_{obs}}} \tag{4.4}$$

T_{sys} consists of all flux contributions from both the sky and the instrument, that is not the signal of interest. One way to think of T_{sys} is that it is the temperature a resistor would have to have to produce the same amount of Johnson-Nyquist noise as the total noise contribution. $\delta\nu$ is the channel width and t_{obs} is the total observing time. As one can see, there are 3 ways to increase the SNR for a source of fixed temperature T_{source}. The system temperature can be reduced, the channel width can be widened, or the observing time can be increased.

Interestingly, the average effective collecting area of a dish is not dependent on the size of the telescope whatsoever. It depends only on the observed wavelength,

$$\langle A_e \rangle = \frac{\lambda^2}{4\pi}. \tag{4.5}$$

Some readers may be thinking that this means that small dishes are equivalent to large dishes and are perhaps confused why we even bother to build large radio dishes. Many telescopes aim to resolve particular sources on the sky and therefore it is favourable for these instruments to be large enough to have the required sensitivity and resolution since these parameters *do* scale with dish size. The Five-hundred-meter Aperture Spherical radio Telescope (FAST), the Green Bank Telescope (GBT), and the previously operational Arecibo Observatory, are large single dish telescopes and are prime examples of how larger telescopes allow us to achieve certain science goals. Still, it is a rather remarkable fact that a television satellite dish has the same average effective area as FAST.

That being said, global 21 cm experiments are single antenna experiments that measure an all sky signal. These experiments are not interested in resolving spatial fluctuations, nor are they interested in increasing their sensitivity in any particular direction on the sky. These experiments are, therefore, rather modest in size, allowing these instruments to be constructed at a low cost and operated virtually anywhere. Ultimately, the science goal will dictate the instrument design.

CCAT-prime, one of our fiducial surveys, is one such single dish telescope located in the Atacama desert at 5612 m altitude. This site makes for optimal observing conditions for sub-millimeter astronomy. CCAT-prime can observe the [CII] line at redshifts 5-9 and has an 16 square-degree field of view. In table 4.1 the instrument specifications are summarised and these are the parameters that will be used for simulating [CII] observations in Chapter 6.

Table 4.1: Parameters for [CII] survey CCATp. These parameters are based on [12], [23]. It should be noted that the parameters with the superscript ($*$) are frequency dependent quantities and the values in the table were computed at 237 GHz.

Paramters	CCAT-prime
System temperature, $\sigma_{\rm pix}$ (MJy/sr$(\rm s)^{1/2}$)	0.86*
Beam FWHM, $\theta_{\rm FWHM}$ (arcmin)	0.75*
Dish Diameter (m)	6
Frequency Range, $\nu_{\rm obs}$ (GHz)	210-300
Channel Width, $\delta\nu$ (GHz)	2.5
Number of Detectors, $N_{\rm det}$	20
EoR Survey Area, $\Omega_{\rm surv}$ (deg^2)	4

4.2 Radio Interferometry

Now that we have come to understand the basics of single dish instruments, one can see that we run into an instrumentation nightmare if one were to try to perform high redshift 21 cm cosmology using a single dish. If, for example, a single dish instrument measuring the 21 cm line at $z \sim 8.5$ were to achieve the same 0.75 arcminute resolution as CCAT-prime, that dish would have to be 8 km in diameter! This is completely infeasible from an instrumental design point of view. Luckily for us, radio interferometry allows us to observe at longer wavelengths while still maintaining high resolution and sensitivity.

Radio interferometry is a technique where instead of using a single large dish to observe the sky, an array of multiple smaller dishes work in unity to act as a single instrument. To gain some intuition, consider the following two dish array.

The baseline vector $\vec{b}$, characterizes the separation and orientation of the dishes relative to one another. The signal vector $\vec{s}$ is the direction of the incoming radiation. As one can see in Figure 4.1, when the signal reached dish 2, it is still a distance $c\tau_g$ away from dish 1. Therefore, the geometric delay τ_g is the extra time it takes for the signal to reach dish 1 after having already reached dish 2. It is referred to as the geometric delay because this delay in arrival time is due only to the geometric orientation of the dishes relative to the sky and has nothing to do with the systematics of the instrument itself. The voltages measured by dishes 1 and 2 are therefore,

$$V_1 = V\cos(\omega \cdot (t - \tau_g)) \quad V_2 = V\cos(\omega \cdot t) \tag{4.6}$$

The voltages V_1 and V_2 are then fed to a correlator which computes the time averaged correlation between the voltages. This is referred to as the response, $R = \langle V_1 V_2 \rangle = V^2/2\cos(\omega \cdot \tau_g)$, where the angle brackets denote a time average.

However, instruments too are imperfect and one can consider a situation where the cable connecting dish 2 to the multiplier (X), is slightly longer than the one connecting dish 1. Therefore the measured voltage V_2 is also delayed by an instrument delay τ_i

$$V_2 = V\cos(\omega \cdot (t - \tau_i)) \tag{4.7}$$

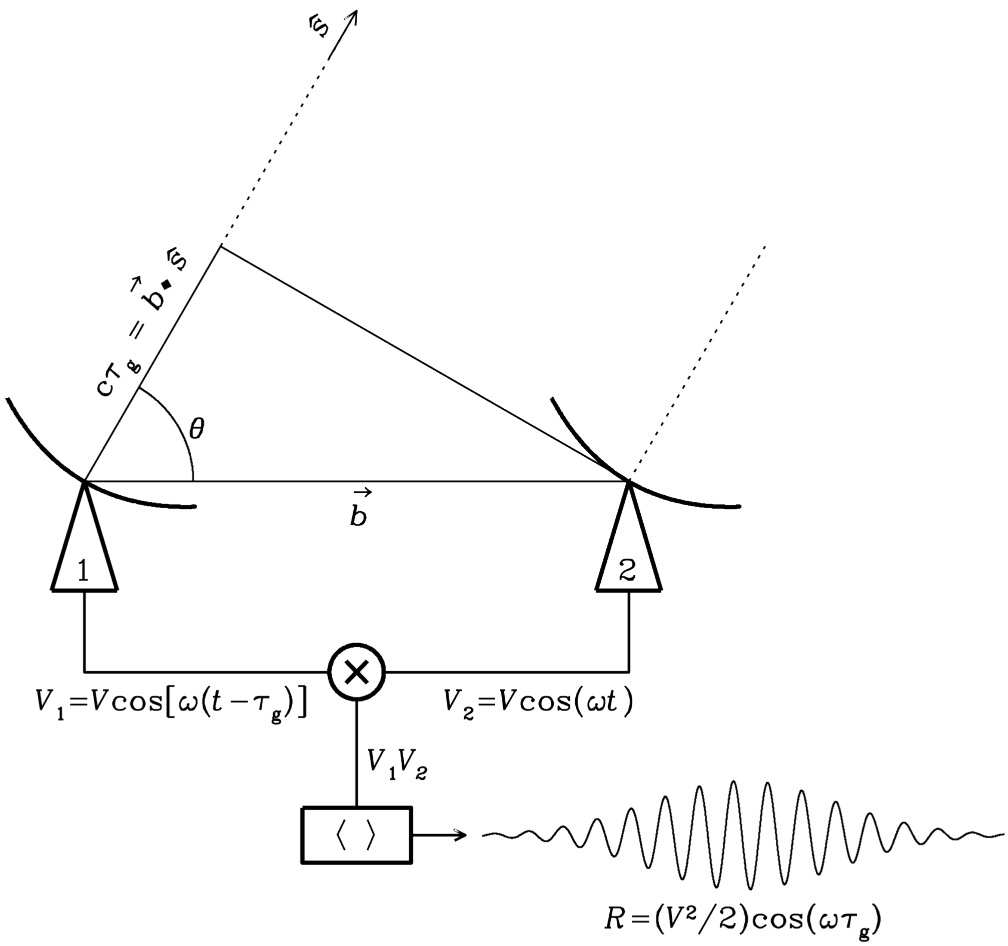

Figure 4.1: Two element array where the (X) denotes the amplifier and multiplier and the $[\langle\rangle]$ symbol denotes the correlator. This figure is reproduced from [26].

and therefore one can define the total time delay of the dishes relative to one another $\tau = \tau_g - \tau_i$. It is convention for τ_i to be positive for the dish that does not experience the geometric delay.

Now, we have made two assumptions which need to be addressed. Firstly, the correlator defined above is a cosine correlator and since cosine is an even function it is only sensitive to the even contribution of the source brightness. However, we are equally justified in constructing a sine correlator where where the cosine is replaced by a sine function in our response equation, $R = \langle V_1 V_2 \rangle = V^2/2\sin(\omega \cdot \tau_g)$. A sine correlator is sensitive to only the odd contribution of the source brightness, and therefore one can consider a complex correlator which takes into account the cosine and sine correlators as real and imaginary components respectively.

$$V = R_{\text{cosine}} + iR_{\text{sine}} \tag{4.8}$$

$$e^{i\theta} = \cos(\theta) + i\sin(\theta) \tag{4.9}$$

The second assumption made was that the source being observed is not extended over some region on the sky. However, intensity mapping precisely deals with extended features and therefore must integrate over the patch of the sky with intensity $I(\nu, \vec{s})$,

$$V(\nu, \vec{b}) = \int A(\nu, \vec{s}) I(\nu, \vec{s}) e^{-2\pi i \left(\frac{\vec{b}\cdot\vec{s}}{\lambda}\right)} d\Omega \tag{4.10}$$

and this quantity, $V(\nu, \vec{b})$, which is a function of the baseline vector and the observed frequency is called the visibility and it is what is measured by an interferometer. The quantity $A(\nu, \vec{s})$ is the primary beam. A few things to note is that visibilities are complex, and that they are nothing more than the sky intensity $I(\nu, \vec{b})$ composed with the Fourier kernel. Therefore what we measure with interferometers is essentially the Fourier transform of the sky intensity with respect to its spatial components. Each baseline measures a single Fourier mode on the sky,

$$k = \frac{2\pi|\vec{b}|}{\lambda D_{\text{comov}}} \tag{4.11}$$

where D_{comov} is the comoving distance to the source being observed. In Section 5.2 on map-making, we will see how we process the visibilities in order to recover a map of sky intensity. The baseline's sensitivity to a single Fourier mode, is the interferomtry analog to the spatial resolution of single dish telescopes. One thing to note is that interferometers are only sensitive to fluctuations about the mean intensity and cannot measure the mean itself. This is because the k = 0 mode corresponds to a dish separation of 0. In many cases, the autocorrelation information is stored, but is too noisy to be salvaged. The noise voltages from two different elements are almost completely uncorrelated, leaving behind a signal after the correlation step. Auto-correlating noise voltages, on the other hand, doesn't get you far.

To now relate the interferometer back to the single dish case, we can look at their difference in point source sensitivity. Recall that for a single dish telescope, the point source sensitivity is given by eq. 4.2 which can be written as,

$$\sigma_{dish} = \frac{2kT_{sys}}{A_e\sqrt{\delta\nu t_{obs}}} \tag{4.12}$$

and the point source sensitivity for a two-dish interferometer is,

$$\sigma_{array} = \frac{2^{1/2}kT_{sys}}{A_e\sqrt{\delta\nu t_{obs}}} \tag{4.13}$$

meaning that the interferometric array is more sensitive than each individual dish in the array but less sensitive than a single dish with the same effective collecting area as the two dishes in the array combined. The reason for this is that the autocorrelation information is lost in an interferometric array. The fact that we cannot measure the k = 0 mode also means that the array is less sensitive than a single dish with the same effective area. For an array of N dishes, the point source sensitivity is given by,

$$\sigma_{array} = \frac{2^{1/2}kT_{sys}}{A_e\sqrt{N(N-1)\delta\nu t_{obs}}}. \tag{4.14}$$

HERA, our fiducial 21 cm survey, is a 350 dish drift-scan array located in the Karoo desert of South Africa. Drift-scan telescopes do not have the dishes point to particular points on the sky, but rather the dishes stay fixed and the sky drifts over the instrument as the Earth rotates. HERA, with its large number of 14 m diameter dishes, is one of the most sensitive EoR experiments for the scales of interest. As we saw in Section 4.1, this means that if the rms noise is roughly the same across experiments, HERA currently has the highest SNR making it sensitive to spatial fluctuations in the signal. In table 4.2, the instrument specifications are listed and these will be the parameters used to simulate HERA in Chapter 6.

Table 4.2: Parameters for 21 cm surveys. (*) indicates quantities computed at 150 MHz. These parameters are based on [35] and [126].

Paramters	HERA
System temperature, $T_{\rm sys}$ (K)	$100 + 120(\nu/150\text{MHz})^{-2.55}$
Beam FWHM at 150 MHz, $\theta_{\rm FWHM}$ (degree)	8.7
Element Diameter (m)	14
Shortest Baseline (m)	14.6
Longest Baseline (core) (m)	292
Longest Baseline (outrigger) (m)	876
EoR Frequency Range, $\nu_{\rm obs}$ (MHz)	100-200
Channel Width, $\delta\nu$ (kHz)	97.8
Survey Area, $\Omega_{\rm surv}$ (deg^2)	1440

Chapter 5

Analysis Tools

5.1 Introduction

In this chapter, we will cover the analysis tools that are often used in observational cosmology and that will be used in the analysis side of the cross-correlation pipeline. Of paramount importance is the power spectrum which allows us to decompose a cosmological field into its Fourier modes and study the correlations of that field. In addition, we will look at map-making methods used to compress and visualize data. We will see that mapping estimators also play a role in observed power spectrum estimation through the computation of window functions.

5.2 Map Making

In the previous chapter we reviewed how interferometers measure the Fourier transform of intensity fluctuations. In this section we will establish the mathematical formalism used to process this data and reproduce maps of these fluctuations. It is of course possible and sometimes preferable to simply conduct one's analysis with the raw visibilities rather than to pursue map-making, especially in cases of power spectrum estimation which is a statistic that is computed in Fourier space. In a cosmological context, map making is often used as a data compression step rather than for visualization as is the case in radio astronomy. Still, mapping is used as a visualization tool mostly to help diagnose systematics instead of observing cosmological fields. It is usually computationally infeasible to constrain cosmological parameters with time-ordered data. Mapping allows one to reduce the size of the data set, making parameter constraints possible. In the case of parameter estimation, the optimal mapping method is one that will minimize the error bars on the parameter estimates. In fact, there exist lossless map estimators that do not increase the error bars on parameter estimates any more than what they would have been if they had been estimated using time ordered data. This is the estimator that will be discussed in this section and that is used in the simulation pipeline.

Firstly, let's consider a vector $\vec{x}_{\text{true}}$ encoding the true sky intensity (i.e before being observed by the instrument). Although the true sky brightness is a continuous function of position, typically maps are pixelized and therefore we will use the notation $\boldsymbol{x} = [x_1, x_2, ..., x_m]$ to denote the vector containing the pixelized "true" sky information. The measured quantity will be denoted by $\boldsymbol{y} = [y_1, y_2, ..., y_n]$ and related to $\boldsymbol{x}$ by,

$$\boldsymbol{y} = \mathbf{A}\boldsymbol{x} + \boldsymbol{n} \tag{5.1}$$

where $\mathbf{A}$ is a known matrix that quantifies the effect of the instrument and $\boldsymbol{n}$ is a random noise vector. If, for example, we consider observations by an interferometer, we can write down the discrete version of 4.10 with noise added as,

$$\begin{bmatrix} V_1 \\ \vdots \\ V_n \end{bmatrix} = \begin{bmatrix} A(\boldsymbol{r}_1)\exp(-2\pi i \boldsymbol{b}_1 \boldsymbol{r}_1/\lambda) & A(\boldsymbol{r}_2)\exp(-2\pi i \boldsymbol{b}_1 \boldsymbol{r}_2/\lambda) & \cdots \\ \vdots & \ddots & \\ A(\boldsymbol{r}_1)\exp(-2\pi i \boldsymbol{b}_n \boldsymbol{r}_1/\lambda) & & A(\boldsymbol{r}_m)\exp(-2\pi i \boldsymbol{b}_n \boldsymbol{r}_m/\lambda) \end{bmatrix} \begin{bmatrix} I_1 \\ \vdots \\ I_m \end{bmatrix} + \begin{bmatrix} n_1 \\ \vdots \\ n_m \end{bmatrix} \tag{5.2}$$

and we can see that it takes precisely the same form as eq. 5.1.

We assume that the noise vector $\boldsymbol{n}$ is such that it is described by a covariance matrix $\mathbf{N}$, where

$$\mathbf{N} = \langle [\boldsymbol{n} - \langle \boldsymbol{n} \rangle][\boldsymbol{n}^t - \langle \boldsymbol{n}^t \rangle] \rangle \tag{5.3}$$

as well as the true sky covariance matrix,

$$\mathbf{S} = \langle [\boldsymbol{x} - \langle \boldsymbol{x} \rangle][\boldsymbol{x}^t - \langle \boldsymbol{x}^t \rangle] \rangle \tag{5.4}$$

and without any loss of generality we can move forward with the assumption that both the signal and the noise have mean zero, $\langle \boldsymbol{n} \rangle = \langle \boldsymbol{x} \rangle = 0$. In addition, we will assume that the sky signal and the noise are uncorrelated, that is $\langle \boldsymbol{x}\boldsymbol{n}^t \rangle = 0$.

The goal now is to define a linear transformation, $\mathbf{M}$, that transforms $\boldsymbol{y}$ into an estimate, $\tilde{\boldsymbol{x}}$, of the true sky, $\boldsymbol{x}$

$$\tilde{\boldsymbol{x}} = \mathbf{M}\boldsymbol{y}. \tag{5.5}$$

It is therefore natural to define the error as how different the estimate is from the true sky,

$$\boldsymbol{\varepsilon} = \tilde{\boldsymbol{x}} - \boldsymbol{x} = (\mathbf{MA} - \mathbf{I})\boldsymbol{x} - \mathbf{M}\boldsymbol{n} \tag{5.6}$$

and try to find an estimator that minimizes $\boldsymbol{\varepsilon}$. The estimator that accomplishes this is the one used by the Cosmic Background Explorer (COBE) team [63] and $\mathbf{M}$ takes the form of,

$$\mathbf{M} = [\mathbf{A}^\dagger \mathbf{N}^{-1} \mathbf{A}]^{-1} \mathbf{A}^\dagger \mathbf{N}^{-1}. \tag{5.7}$$

This estimator has the following 3 desirable properties [149] ,

1. χ^2 is minimized
2. The ensemble averaged error is minimized
3. It provides the maximum-likelihood estimate of $\boldsymbol{x}$ assuming that $\boldsymbol{n}$ is uncorrelated Gaussian noise.

Therefore, in a noiseless approximation, the estimated map is related to the true sky by the matrix,

$$\tilde{\boldsymbol{x}} = [\mathbf{A}^\dagger \mathbf{N}^{-1} \mathbf{A}]^{-1} \mathbf{A}^\dagger \mathbf{N}^{-1} \mathbf{A}\boldsymbol{x} = \mathbf{S}\boldsymbol{x} \tag{5.8}$$

We will see this estimator in action in the following chapter.

5.3 Power Spectrum Estimation

5.3.1 Power Spectra

At its core power spectra quantify correlations. There exist many cosmological fields that, to our great pleasure, are correlated due to the underlying physics that governs the behaviour of these fields. For instance, the matter field exhibits correlations driven by gravity which is why we tend to find galaxies clustered together rather than randomly scattered throughout the universe. As such, cosmology concerns itself with quantifying the statistics of its fields using correlation functions and consequently, power spectra.

While the goal of this section is understanding the power spectrum we will first motivate it with the correlation function. A correlation function indicates whether a particular field you are measuring at, say, one location is spatially correlated to the field at another location. Making the assumptions that cosmological fields are statistically translationally invariant, and that the Universe is statistically isotropic, we can write the correlation function as follows,

$$\xi(r) = \xi(|\mathbf{r_1} - \mathbf{r_2}|) = \langle T(\mathbf{r_1})T(\mathbf{r_2})\rangle \tag{5.9}$$

where here $T(\boldsymbol{r_1})$ and $T(\boldsymbol{r_2})$ represent the brightness temperature of a transition line. From here onward, we will use this notation to indicated intensities of pixels on the sky instead of the $I(\boldsymbol{r})$ used in previous sections. To provide a bit of intuition, if $\xi(r) = 1$ then the brightness temperatures $T(\mathbf{r_1})$ and $T(\mathbf{r_2})$ are likely to both be brighter (of both be dimmer) than average brightness temperature of the field, and if $\xi(r) = -1$ then if $T(\mathbf{r_1})$ is brighter than the mean, $T(\mathbf{r_2})$ will likely be darker than the mean. If $\xi(r) = 0$ then, on average, the brightness temperature at $\mathbf{r_1}$ tells us nothing about the brightness temperature at $\mathbf{r_2}$, they are uncorrelated.

The correlation function defined above lives in position or configuration space. We can equally well study the power spectrum which is defined as the Fourier transform of the correlation function and we will see that simply performing a Fourier transform can be advantageous. The power spectrum, $P(\boldsymbol{k})$, is defined as,

$$P(\mathbf{k}) = \int_{-\infty}^{\infty} d^3 r e^{-i\boldsymbol{k}\cdot\boldsymbol{r}} \xi(\boldsymbol{r}). \tag{5.10}$$

The power spectrum can be computed from the ensemble average of the Fourier transform of the brightness temperature, $\hat{T}$,

$$\begin{aligned}
\langle \hat{T}(\boldsymbol{k_1}) \hat{T}(\boldsymbol{k_2})^* \rangle &= \int d^3 r_1 d^3 r_2 e^{-i\boldsymbol{k_1}\cdot\boldsymbol{r_1}} e^{i\boldsymbol{k_2}\cdot\boldsymbol{r_2}} \langle T(\boldsymbol{r_1}) T(\boldsymbol{r_2}) \rangle \\
&= \int d^3 r_1 d^3 r_2 e^{-i\boldsymbol{k_1}\cdot\boldsymbol{r_1}} e^{i\boldsymbol{k_2}\cdot\boldsymbol{r_2}} \int \frac{d^3 k}{(2\pi)^3} e^{-i\boldsymbol{k}\cdot(\boldsymbol{r_1}-\boldsymbol{r_2})} P(\boldsymbol{k}) \\
&= (2\pi)^3 \int d^3 k P(\boldsymbol{k}) \delta^3(\boldsymbol{k_1} - \boldsymbol{k}) \delta^3(\boldsymbol{k_2} - \boldsymbol{k})
\end{aligned}$$

which we can now integrate.

$$\langle \hat{T}(\boldsymbol{k}) \hat{T}(\boldsymbol{k'})^* \rangle = (2\pi)^3 P(\boldsymbol{k}) \delta^3(\boldsymbol{k} - \boldsymbol{k'}) \tag{5.11}$$

Now, of course the equation above is not quite useful yet, because we cannot divide both sides by a delta function in the hopes of isolating $P(\boldsymbol{k})$. In order to make this equation computationally tractable, one can redo this computation taking into account the fact that we can only survey a finite volume. In this case the brightness temperature we actually measure is,

$$T_{\text{obs}}(\boldsymbol{r}) = \phi(\boldsymbol{r}) T(\boldsymbol{r})$$

where

$$\phi(\boldsymbol{r}) = \begin{cases} 1 & \text{if } \boldsymbol{r} \text{ is inside the survey volume} \\ 0 & \text{otherwise} \end{cases}$$

If one were to redo the computation above with T_{obs}, one will find the estimate for eq. 5.11 to be,

$$P(\boldsymbol{k}) \approx \frac{\langle \hat{T}_{\text{obs}}(\boldsymbol{k}) \hat{T}_{\text{obs}}(\boldsymbol{k'})^* \rangle}{V}. \tag{5.12}$$

.

5.3.2 Window Functions

In section 5.2, we defined a linear estimator that took us from true sky brightnesses to the sky we would see if it were mapped by some instrument. In addition, that original field of interest, $\boldsymbol{x}$ has associated with it a power spectrum $P(\boldsymbol{k})$, and likewise the estimate of the field $\tilde{\boldsymbol{x}}$ has associated with it a power spectrum which we will call $\tilde{P}(\boldsymbol{k})$. So now we can ask ourselves, is there a linear estimator that can take the true power spectrum of $\boldsymbol{x}$ and tell us what the estimated spectrum is given that we know how $\boldsymbol{x}$ is related to $\tilde{\boldsymbol{x}}$? The answer to this question is yes, and it is the goal of this section to compute these transfer functions known as window functions.

For completeness and clarity, we will begin by working in the continuum limit and then move back to the pixelized version of the power spectrum estimator at the very end. Firstly, let us consider a vector $x(\vec{r}\prime)$ which contains all the true brightnesses at every point on the sky being observed. Again, "true" denotes that this is the sky unobserved by the telescope. Once the observation is made, the instrument transforms the sky such that the image is not a perfect depiction of the true sky but it has been in some way mangled by the instrument. This observed sky is denoted by $\tilde{x}_(\vec{r})$. Explicitly,

$$\tilde{x}(\vec{r}) = \int S(\vec{r}, \vec{r}\,')x(\vec{r}\,')d^3\vec{r}\,' \tag{5.13}$$

where $S(\vec{r}, \vec{r}\,')$ is the linear estimator that characterizes both the particular instrument doing the observing and the mapping method of choice.

Since the power spectrum is computed using the Fourier transform of the field, a first step would be to find the function that transforms the Fourier transform of the true sky,

$\hat{x}(\vec{r})$, to the Fourier transform of the observed sky, $\hat{\tilde{x}}(\vec{r})$

$$
\begin{aligned}
\tilde{x}(\vec{r}) &= \int S(\vec{r},\vec{r}\,')x(\vec{r}\,')d^3\vec{r}\,' \longrightarrow \text{FT of both sides} \\
\hat{\tilde{x}}(k) &= \int d^3\vec{r}e^{-i\vec{k}\cdot\vec{r}} \int d^3\vec{r}\,'S(\vec{r},\vec{r}\,')x(\vec{r}\,') \\
\hat{\tilde{x}}(k) &= \int d^3\vec{r}e^{-i\vec{k}\cdot\vec{r}} \int d^3\vec{r}\,'S(\vec{r},\vec{r}\,') \int \frac{1}{(2\pi)^3} d^3\vec{k}\,'e^{i\vec{k}\,'\cdot\vec{r}\,'}\hat{x}(\vec{k}\,') \longrightarrow \text{Fourier inversion of } x(r) \\
\hat{\tilde{x}}(k) &= \int \frac{1}{(2\pi)^3} d^3\vec{k}\,'\hat{x}(\vec{k}\,') \int\int d^3\vec{r}d^3\vec{r}\,'e^{i\vec{k}\,'\cdot\vec{r}\,'}e^{-i\vec{k}\cdot\vec{r}}S(r,\vec{r}\,') \\
\hat{\tilde{x}}(k) &= \int \frac{1}{(2\pi)^3} d^3\vec{k}\,'\hat{x}(\vec{k}\,') \int\int d^3\vec{r}d^3\vec{r}\,'e^{-i(-\vec{k}\,')\cdot\vec{r}\,'}e^{-i\vec{k}\cdot\vec{r}}S(r,\vec{r}\,') \\
\hat{\tilde{x}}(k) &= \int \frac{1}{(2\pi)^3} d^3\vec{k}\,'\hat{x}(\vec{k}\,')\widehat{\widehat{S}}(\vec{k},-\vec{k}\,')
\end{aligned}
$$

So now we know that $\hat{x}(\vec{k}')$ gets transformed to $\hat{\tilde{x}}(\vec{k})$ by the function $\widehat{\widehat{S}}(\vec{k},-\vec{k}\,')$. The double-hat here denotes that Fourier transforms were taken with respect to both $\vec{k}$ and $\vec{k}'$.

This transformation can be visualised in the following commutative diagram. Going

$$
\begin{tikzcd}
\tilde{x} \arrow[d, mapsto, "\mathcal{F}"] & x \arrow[l, mapsto, "\mathbf{S}"] \arrow[d, mapsto, "\mathcal{F}"] \\
\hat{\tilde{x}} & \hat{x} \arrow[l, mapsto, "\widehat{\widehat{\mathbf{S}}}"]
\end{tikzcd}
$$

counter clockwise from $\hat{x}$, to $\hat{\tilde{x}}$, it is now clear that,

$$
\widehat{\widehat{\mathbf{S}}} = \mathcal{F} \circ \mathbf{S} \circ \mathcal{F}^{-1}. \tag{5.14}
$$

With this function we can then compute the observed power spectrum from the "true" one.

$$\langle|\hat{\tilde{x}}(\vec{k})|^2\rangle = \frac{1}{(2\pi)^3(2\pi)^3}\int\int d^3\vec{k_1}d^3\vec{k_2}\widehat{\hat{S}}(\vec{k},\vec{k_1})\widehat{\widehat{S^*}}(\vec{k},\vec{k_2})\langle\hat{x}(\vec{k_1})\hat{x}(\vec{k_2})^*\rangle$$
$$\langle|\hat{\tilde{x}}(\vec{k})|^2\rangle = \frac{1}{(2\pi)^3(2\pi)^3}\int\int d^3\vec{k_1}d^3\vec{k_2}\widehat{\hat{S}}(\vec{k},\vec{k_1})\widehat{\widehat{S^*}}(\vec{k},\vec{k_2})(2\pi)^3\delta^D(\vec{k_1}-\vec{k_2})P(\vec{k_1})$$
$$\langle|\hat{\tilde{x}}(\vec{k})|^2\rangle = \frac{1}{(2\pi)^3}\int d^3\vec{k_1}|\widehat{\hat{S}}(\vec{k},\vec{k_1})|^2P(\vec{k_1})$$

Now, the observed power spectrum is defined in the following way,

$$\tilde{P}(\vec{k}) = \frac{\langle|\hat{\tilde{x}}(\vec{k})|^2\rangle}{V} = \frac{1}{V(2\pi)^3}\int d^3\vec{k_1}|\widehat{\hat{S}}(\vec{k},\vec{k_1})|^2P(\vec{k_1}) \tag{5.15}$$

Now we can define the window function, denoted by $W(\vec{k},\vec{k_1})$,

$$W(\vec{k},\vec{k_1}) = \frac{1}{V(2\pi)^3}|\widehat{\hat{S}}(\vec{k},\vec{k_1})|^2 \tag{5.16}$$

Similar to eq. 5.5, this is the set of transfer functions that tells us what the observed spectrum of a field will be given a mapping estimator S. Moving now to the discrete pixelized case, we can write

$$\tilde{\mathbf{P}} = \mathbf{WP} \tag{5.17}$$

Chapter 6

Cross-Correlation Simulation and Analysis Pipeline

6.1 Introduction

In this chapter, we will explore the potential of using cross-correlations between 21 cm and [CII] LIM observations to probe the epoch of reionization. As has been previously mentioned, 21 cm observations suffer from bright foreground contaminants that are 4–5 orders of magnitude brighter than the signal. In theory, these spectrally smooth foregrounds should be able to be easily subtracted from the quickly varying signal. However, the chromatic window functions of interferometers introduce aberrations to an otherwise smooth foreground spectrum making these foregrounds appear more like the cosmological signal. While foreground removal techniques are still being explored, it remains a key challenge and there is increasing desire to measure cross-spectra for validation. Cross-correlations do not suffer from the same foreground biases as auto-correlations due to the fact that the two probes being correlated are observed at difference frequencies and therefore their foregrounds do not emanate from the same sources at the same redshifts. As such, the foregrounds of our two probes are uncorrelated leaving behind the distinctly correlated signal. In this chapter, we test this hypothesis using an end-to-end simulation and analysis pipeline and present our first results. A schematic depiction of this pipeline can be found in Figure 6.1. Starting at the top of the figure, the pipeline takes in as input two correlated cosmological fields. Their respective foreground contaminants are added on according to the particular frequency being observed. What follows is the observation by the instrument and in the case of this thesis, HERA and CCAT-prime are used as fiducial surveys. For interferometric observations, we proceed to map-making and once both maps are obtained, their cross-spectrum is computed. There is also a theory module which computes the joint window function of the two experiments. This window function will be used to compute a window function estimated power spectrum to be compared to the output of the simulation and analysis pipeline.

Each module of this pipeline was built from the ground up with the exception of the modelling of 21 cm synchrotron radiation which was done using the `pyGSM` package developed by [33, 167]. While the surveys used here are HERA and CCAT-prime, this is a general framework that can be used to model any single dish or interferometric instrument; all parameters can be altered to the design specifications of the instrument one is interested in modelling. The source code for this pipeline can be found here[1] and in the next two sections, we will go over how the instruments and foregrounds are modelled. What will follow is a full run-through of the pipeline using a toy cosmological model with the first results. It should be noted that the current version of this pipeline analyses 2D slices at a given frequency. This limitation will be addressed and this work is to be extended to take in 3-dimensional data cubes and make use of spectral information in addition to the spatial information present in the 2D slices.

6.2 21 cm Foreground Contaminants

Despite the promise of 21 cm cosmology, using the 21 cm line to map out the large scale structure in the universe is subject to serious challenges, namely, bright foreground contaminants. These foregrounds are varied in both spectral and spatial extent and are 4–5 orders of magnitude brighter than the 21 cm signal. This is in contrast to CMB observations, where the CMB signal is dominant to its foregrounds. The main contaminants to

[1] https://github.com/hannahfro/X-CorrPipeline

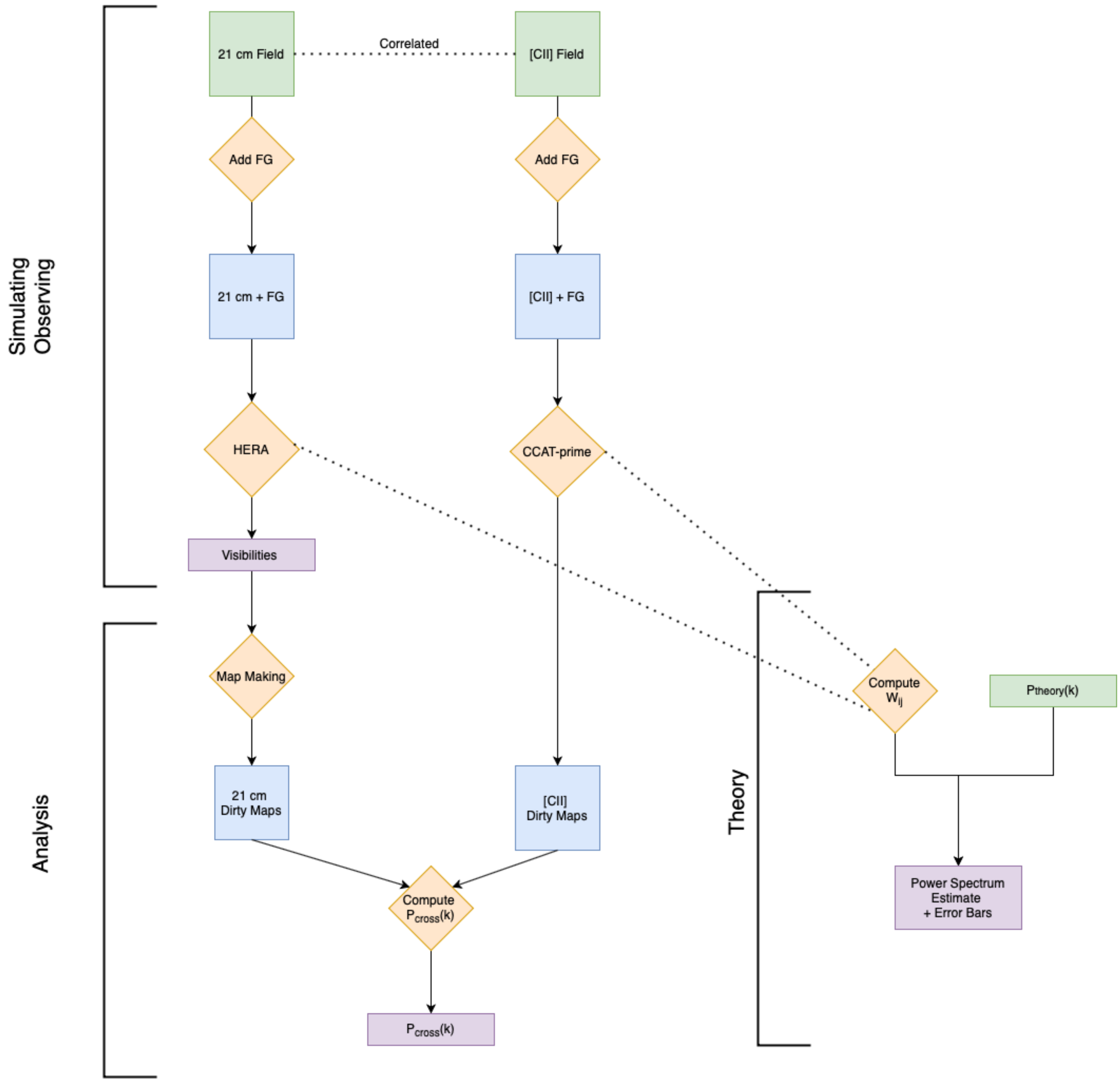

Figure 6.1: This flowchart depicts the computations performed in the simulation and analysis pipeline. Starting from the top, correlated fields are used as inputs. Next, foregrounds and instrumental noise are generated. In the case of observations by an interferometer, a map-making step follows. Finally, the dirty maps are used to compute cross-spectra. In addition, there is a theory branch which uses the matrices quantifying instrumental effects to construct window functions and estimate power spectra from the theoretical ones used to construct the input cosmological fields.

the 21 cm line are, galactic synchrotron emission, Bremsstrahlung radiation, and bright extragalactic point sources. In this section, we will lay out how each of the contaminants is modeled in the simulation pipeline.

6.2.1 Galactic Synchrotron Emission

Galactic synchrotron radiation is the brightest diffuse foreground contaminant. As the name suggests, it is emanating from our Milky Way galaxy and is the result of charged particles moving through magnetic fields. In this work, galactic synchrotron radiation is simulated using the `pyGSM` package developed by de Oliveira-Costa et al. and Zheng et al. [33, 167]. Since there do not exist all-sky maps of our galaxy at all frequencies from observation, this package allows one to interpolate the currently available data to create all-sky maps in the frequency range 10 MHz – 5 THz. This simulation takes into account flux as a function of position which allows one to obtain a realistic foreground map in which foregrounds are brighter in the centre of the galactic plane and dimmer toward the outskirts. There are two generations of this code; the pioneering version released in 2008 is referred to as `gsm2008` and the most recent update from 2016 is referred to as `gsm2016`. For the work done in this thesis, the 2016 version was used and therefore the discussion of the interpolation method will be mostly dedicated to this version only.

This package uses an iterative principal component analysis (PCA) algorithm and uses 29 sky maps between 10 MHz and 5 THz [167] to reconstruct the sky in this frequency range. PCA is a process by which some data matrix, $\mathbf{D}$ is diagonalized and its non-zero eigenvalues are then used to reconstruct the data matrix. The general idea is that for some data matrix $\mathbf{D}$ with dimension $n_{\text{pix}} \times n_f$, there exist certain matrices $\mathbf{M}$ and $\mathbf{S}$ with dimension $n_{\text{pix}} \times n_c$ and $n_c \times n_f$ respectively such that,

$$\mathbf{D} \approx \mathbf{MS}. \tag{6.1}$$

The matrix D is reconstructed if $\mathbf{M}$ and $\mathbf{S}$ minimize the cost function,

$$|\mathbf{D} - \mathbf{MS}|^2. \tag{6.2}$$

For this iterative algorithm, $\mathbf{M}$ and $\mathbf{S}$ are obtained for each iteration in the following way. First, these matrices are computed for the base case. While the entire data matrix $\mathbf{D}$ contains 29 sky maps, some maps are omitted for this step and only the maps that share 5% sky coverage are used. This pared down data matrix will be denoted by D^* and $\mathbf{D}^{*,T}\mathbf{D}$ diagonalized as follows,

$$\mathbf{D}^{*,T}\mathbf{D} = \mathbf{C^T \Lambda C} \tag{6.3}$$

where $\mathbf{C}$ is an $n_f \times n_f$ orthogonal matrix of eigenvectors of $\mathbf{D}^{*,T}\mathbf{D}$ along it rows, and $\mathbf{\Lambda}$ is an $n_f \times n_f$ matrix with the eigenvalues of $\mathbf{D}^{*,T}\mathbf{D}$ along its diagonal. The non-zero eigenvalues and their corresponding eigenvectors are identified and are denoted as the principle components. Then, if the non-principal components are removed,

$$\mathbf{D}^{*,T}\mathbf{D} = \mathbf{\tilde{C}^T \tilde{\Lambda} \tilde{C}} \tag{6.4}$$

where now, $\mathbf{\tilde{C}}$ has dimension $n_c \times n_f$ and $\mathbf{\tilde{\Lambda}}$ has dimensions $n_c \times n_c$ and n_c denotes the number of principal components.

It should now be plain to see that $\mathbf{\tilde{C}}$ has the same dimensions as $\mathbf{S}$ and so $\mathbf{\tilde{C}}$ is what will be used to find $\mathbf{M}$ that satisfies eq 6.2, meaning

$$\mathbf{D} \approx \mathbf{M\tilde{C}}. \tag{6.5}$$

This resulting matrix $\mathbf{M}$ will be denoted $\mathbf{M^{(0)}}$ and $\mathbf{\tilde{C}}$ will be denoted $\mathbf{S^{(0)}}$ since they are the result of the base case of the iteration. The subsequent $\mathbf{M^{(i)}}$ and $\mathbf{S^{(i)}}$ are computed using the following equations,

$$\mathbf{S^{(i)}} = (1-\eta)\mathbf{S^{(i-1)}} + \eta(\mathbf{M^{(i-1)T}M^{(i-1)}})^{-1}\mathbf{M^{(i-1)T}D} \tag{6.6}$$

$$\mathbf{M^{(i)}} = (1-\eta)\mathbf{M^{(i-1)}} + \eta(\mathbf{S^{(i)}S^{(i)T}})^{-1}\mathbf{S^{(i)}D}^T \tag{6.7}$$

where $0 < \eta \leq 1$ is a step size. The iteration proceeds until the cost function, eq 6.2, decreases by less that 0.01%. Performing this iteration between the components and the maps allows one to find the best fit to all of the data available. The previous version required one to restrict which maps could be used based on which maps had overlapping pixel fluxes. This iterative approach allows one to make use of more maps and more pixels per map, resulting in both more accurate maps, and maps simulated in a larger frequency range.

For those looking for a simpler but statistically accurate model, the foreground spectrum can be fit by a power law as prescribed in Liu & Tegmark [85]. In this model, each pixel is assigned a flux density according to the power law spectrum,

$$x(\nu) = A_{\mathrm{sync}} \left(\frac{\nu}{\nu_*} \right)^{-\alpha_{\mathrm{sync}}} \tag{6.8}$$

where $A_{\mathrm{sync}} = 335.4$ K and $\nu_* = 150$ MHz [160]. Flux differences from pixel to pixel are achieved by varying the spectral index, α_{sync}. For each pixel, the spectral index is drawn from a Gaussian distribution with mean $\overline{\alpha}_{\mathrm{sync}} = 2.8$ and standard deviation $\Delta\alpha_{\mathrm{sync}} = 0.1$ [160]. While the average flux of this map is roughly the same as that of the pyGSM map at the same frequency, position correlations in flux are lost. Therefore, for the remainder of this work, we proceed with using only the pyGMS model.

6.2.2 Bremsstrahlung Emission

The next contaminant to be modelled is Bremsstrahlung emission from ionizing sources which constitutes a bright diffuse radio foreground. The Bremsstrahlung emission is modeled in precisely the same way as the Liu & Tegmark model for galactic synchrotron radiation. Again, each pixel has a power law spectrum of the form,

$$x(\nu) = A_{\mathrm{ff}} \left(\frac{\nu}{\nu_*} \right)^{-\alpha_{\mathrm{ff}}} \tag{6.9}$$

except here, $A_{\mathrm{ff}} = 33.5$ K and $\nu_* = 150$ MHz [160]. Again, for each pixel a spectral index is draw from a Gaussian distribution, where in this case, the mean is $\overline{\alpha}_{\mathrm{ff}} = 2.15$ and standard deviation $\Delta\alpha_{\mathrm{ff}} = 0.01$ [160].

6.2.3 Extragalactic Point Sources

Finally, we must consider extragalactic point sources, of which two main populations arise: bright radio point sources and unresolved sources. It should be noted that a third sub-category is bright extended sources, that is, bright and nearby extragalactic sources that have a spatial extent greater than a single pixel. For 21 cm observations, an example of such a source is Fornax A. This sub-category of bright sources is not included in this model of foregrounds but a treatment of extended sources can be found in [81].

The first class of extragalactic sources are those which are unresolved by the instrument. Here these sources are taken to have a flux of 100 mJy or less. This is due to the fact that most peeling techniques that are used to remove bright point sources can only remove sources whose flux is greater than $\sim$ 10-100 mJy. Of course, the exact flux cutoff depends on the resolution and sensitivity of the instrument since, for example, an instrument with lower resolution will smear more sources into the unresolved background. As in [85], the more conservative bound of 100 mJy is used here. First, each pixel is populated with 100 sources, with S_* values drawn from the following source count distribution,

$$\frac{dn}{dS_*} = B\left(\frac{S_*}{880\text{mJy}}\right)^{-\gamma} \tag{6.10}$$

where B = 4.0 mJy^{-1}sr^{-1} and $\gamma = 1.75$ [37]. It should be noted that this source count distribution is scaled by the pixel size. Again, the choice of 100 sources is simply an assumption, but for a more realistic treatment, one can draw the number of sources per pixel using the Schechter luminosity function in much the same way as is done in section 6.3.

Now that each source in the pixel has it's own S_* value, the flux of each source is then drawn from the power law distribution,

$$x(\nu) = 1.4 \times 10^{-6}\left(\frac{\nu}{\nu_*}\right)^{-2}\left(\frac{\Omega_{\text{pix}}}{1sr}\right)^{-1} S_*\left(\frac{\nu}{\nu_*}\right)^{-\alpha}\text{mJy} \tag{6.11}$$

where the spectral index α is drawn from a gaussian with mean $\overline{\alpha} = 0.5$ and standard deviation $\Delta\alpha = 0.5$, in agreement with CMB observations [150]. This alpha is drawn for each source in the pixel, and once all the source fluxes have been computed, they are averaged over to obtain the total pixel flux. This process is then repeated for each pixel in the map.

Lastly, we consider bright radio point sources: bright radio foreground galaxies. These are not simulated by a model, but rather are taken from the Galactic and Extragalactic All-sky MWA (GLEAM) survey which observed 24,402 square degrees on the sky over declinations south of 30 degrees and Galactic latitudes 10 degrees of the Galactic plane. The catalog consists of observations of 307,455 radio sources across frequencies 72-231 MHz and with resolution of $\sim$ 2 arcminutes [60]. In order to account for bright sources in the side lobes of the primary beam, bright point sources are not added to the input map directly, but instead their visibilities are computed and added to the simulated observation in phase-space. Each source is characterized by its brightness and its position on the sky, therefore its visibility is defined as

$$V_{lm} = A_m T_m e^{2\pi i (b_l \cdot r_m)/\lambda} d\theta d\phi \tag{6.12}$$

where T_m is the brightness of the m$^{\text{th}}$ source measured by GLEAM, r_m is the position of the m$^{\text{th}}$ source, and A_m is the attenuation factor of the primary beam at the position of the source, and b_l is the baseline coordinates at a particular time.

Now, as mentioned in the previous section, unresolved extragalactic point sources are simulated below 100 mJy, and as such, bright extragalactic point sources are only simulated above 100 mJy. In order to ensure that this is the case and that we are not doubling up on dim sources, the following condition is imposed:

$$A_m T_m > 100 \text{ mJy}. \tag{6.13}$$

Since HERA is a drift scan telescope and bright sources move in and out if its primary beam, this condition is checked at every observing time. These are the three sources of foreground contaminants that are modeled in this simulation pipeline. As mentioned, the diffuse foregrounds are added in position space to the cosmological field, and the bright point sources are incorporated at the level of visibilities. In the subsequent section, we review the simulation of [CII] foregrounds.

6.3 [CII] Foreground Contaminants

Unlike 21 cm observations, which suffer from several sources of diffuse foregrounds, the main contaminants of [CII] are low redshift line interlopers. Carbon monoxide (CO) at low redshifts undergoes spontaneous rotational transitions, emitting a photon which redshifts into the same frequency band as the photon emitted from [CII] at high redshift. In particular, CO (6-5), CO (5-4), CO (4-3), CO (3-2), CO (2-1), are line interlopes for [CII] observations during the EoR, where the pairs of numbers denote the quantum numbers, J, indicating the change in the total angular momentum state of the molecule. It may be of concern to some that the [CII] line interlopers and 21 cm point source foregrounds may in fact be emanating from the same galaxies at $0 \lesssim z \lesssim 3$. While this is certainly not impossible, it is not likely. There does exist a handful of hydrogen and deuterium fine structure lines whose rest frequencies are such that if they came from the same $0 \lesssim z \lesssim 3$ galaxies as the line interlopers, they would redshift into 21 cm observed frequency range [43,74]. That being said, the transition rate of these lines is unknown and the transitions have only been observed under strict laboratory conditions. Still, one may consider a broadband emission which could produce this correlation though such a scenario is omitted here. For the simulations done in this chapter, we generate independent realizations of both point source foreground contaminants.

In this section we will describe the method used to simulate these foregrounds. This method is based on the prescription of Cheng, Chang, & Bock [18]. The main difference with the method employed here, is that we approach the modelling from an observational point of view which has the added benefit of decreasing the computational cost. Instead of building a large and dense lightcone, we instead populated the spectral channels of the instrument with the lines that will have redshifted into that channel. As previously mentioned, the code currently computes one spectral channel at a time but can be parallelized to produce a host of foreground maps since each frequency map is generated independently. The following will be a discussion of how the foregrounds in one frequency channel are computed. For a multi-channel case, this computation is repeated for every channel in the observing band.

This foreground model relies on only 3 pieces of information as input: the lower and upper bound frequencies of the channel in GHz, the pixel size in steradians, and the number of pixels in the output map. Built into this model is CO luminosity function data namely, the rest frequencies and the Schechter luminosity function parameters for lines CO (6-5), CO (5-4), CO (4-3), CO (3-2), CO (2-1), CO (1-0). These parameters were obtained from the CO luminosity function models of Popping et al. [128]. The Schechter parameters are the following: α, $\log((\phi_*)$ [Mpc^{-3} dex^{-1}], $\log(L_*)$ [Jy km/s Mpc^2]. The first computation done here is to convert the unit of $\log L_*$ to [W m^{-2} Mpc^2] which amounts to converting [Jy km/s] to [W m^{-2}]. The conversion factor is,

$$1 \text{ Jy km/s} = \frac{10^{-26}\text{W m}^{-2}\text{ Hz}^{-1}}{3\times 10^5\text{km/s}}\nu_{\text{obs}}\text{Hz}. \tag{6.14}$$

Since it is $\log L_*$ and not L_* itself that is in the data array, the unit conversion is carried out using the logs of L_* and the conversion factor,

$$\log L_*[\text{W m}^{-2}\text{ Mpc}^2] = \log L_*[\text{Jy km/s Mpc}^2] + \log\frac{10^{-26}\text{W m}^{-2}\text{ Hz}^{-1}}{3\times 10^5\text{km/s}}\nu_{\text{obs}}\text{Hz}. \tag{6.15}$$

The luminosity bins are also defined and are in fact L/L$_*$ bins ensuring that every line will always be populated by sources the same order of magnitude dimmer and brighter than their respective L$_*$. The L/L$_*$ bin width in log space is also computed.

In what follows, we determine which lines redshift into the observed frequency channel. Using the rest frame frequency of each line and eq. 2.3, the frequency-redshift relation , we check the condition that for a line to be redshifted into the observed frequency channel, it must be the case that $z_{\text{emit}} \geq 0$. If the $z_{\text{emit}} \geq 0$ condition is met, we then proceed to interpolate the Schechter parameter data for that line in order to find all of the parameters at z_{emit}. The Schechter parameters of the lines observable in that channel are then stored.

Now we proceed to using the Schechter luminosity function to populate the luminosity bins of each line with sources. Starting with the Schechter function derived in [134], the number density of galaxies of luminosity L+dL is given by,

$$\Phi(L_{\rm CO})dL_{\rm CO} = \phi_* \left(\frac{L_{\rm CO}}{L_*}\right)^{\alpha} e^{-(L_{\rm CO}/L_*)} d(L_{\rm CO}/L_*). \tag{6.16}$$

But since the L/L_* bins were defined in log space, we can rewrite $d(L_{CO}/L_*)$ in the following way,

$$d(L_{\rm CO}/L_*) = ln(10)\left(\frac{L_{\rm CO}}{L_*}\right) d\log(L_{\rm CO}/L_*) \tag{6.17}$$

and substituting this into 6.16, we obtain,

$$\Phi(L_{\rm CO})dL_{\rm CO} = \ln(10)\phi_* \left(\frac{L_{\rm CO}}{L_*}\right)^{\alpha+1} e^{-(L_{\rm CO}/L_*)} d\log(L_{\rm CO}/L_*). \tag{6.18}$$

So now we have obtained the quantity of interest because $\Phi(L_{\rm CO})dL$ is the number of galaxies with luminosity $L+dL$ per unit volume. Since we are dealing with arrays and not continuous variables, we will now denote dL's by $\Delta L_{\rm CO}$'s instead, where $\Phi(L_{\rm CO})\Delta L_{\rm CO}$ is the number of galaxies per unit volume in the luminosity interval $\Delta L_{\rm CO}$ centred on $L_{\rm CO}$. Now we must adjust for the size of the voxel (or pixel), since we desire the number of galaxies contained in a voxel of a certain volume in the luminosity bin of width $\Delta L_{\rm CO}$ centred on $L_{\rm CO}$, which we will denote by $n(L_{\rm CO})\Delta L_{\rm CO}$. So we simply multiply by the volume of the voxel (or area of the pixel) to get $n(L_{\rm CO})\Delta L_{\rm CO}$

$$n(L_{\rm CO})\Delta L_{\rm CO} = \Phi(L_{\rm CO})\Delta L_{\rm CO} V_{\rm vox} = \ln(10)\phi_* \left(\frac{L_{\rm CO}}{L_*}\right)^{\alpha+1} e^{-(L_{\rm CO}/L_*)} \Delta\log(L_{\rm CO}/L_*) V_{\rm vox}. \tag{6.19}$$

This $V_{\rm vox}$ is computed using the differential comoving volume element $\mathrm{dV_{comov}}$ in [Mpc^3 sr^{-1}] and $\Omega_{\rm pix}$, the pixel size in steradians. Therefore,

$$V_{\rm vox} = dV_{\rm comov}\Omega_{\rm pix}. \tag{6.20}$$

Now, $n(L_{\rm CO})\Delta L_{\ rmCO}$ is the average number of sources in each luminosity bin. What we proceed to do is loop through each luminosity bin for each line, draw the number of sources in that luminosity bin from a Poisson distribution, and multiply that number of sources by the luminosity of that bin. Since the bins were defined as $\log(L_{\rm CO}/L_*)$, the final luminosity is computed in the following way,

$$L = 10^{\log(L_{\rm CO}/L_*)+\log(L_{*,\rm line})}. \tag{6.21}$$

Recall that this L is in units of [W m^{-2} Mpc^2], and in order to simulate these foregrounds in a way that will be useful and familiar to observers we proceed with the last step which is simply a unit conversion. This intensity is defined as the following,

$$I[\text{Jy sr}^{-1}] = L[\text{W m}^{-2}\text{ Mpc}^2]\frac{10^{26}}{4\pi D_\ell(z_{\rm emit})[\text{Mpc}^2]\delta\nu_{\rm obs}[\text{Hz}]\Omega_{\rm pix}[\text{sr}]}. \tag{6.22}$$

In Figure 6.2 the luminosity of each line is plotted as a function of redshift and observed frequency. A magenta horizontal line is placed at the observing frequency of the run presented in this thesis. The [CII] line observed at $\nu = 200$ suffers from five bright line interlopers.

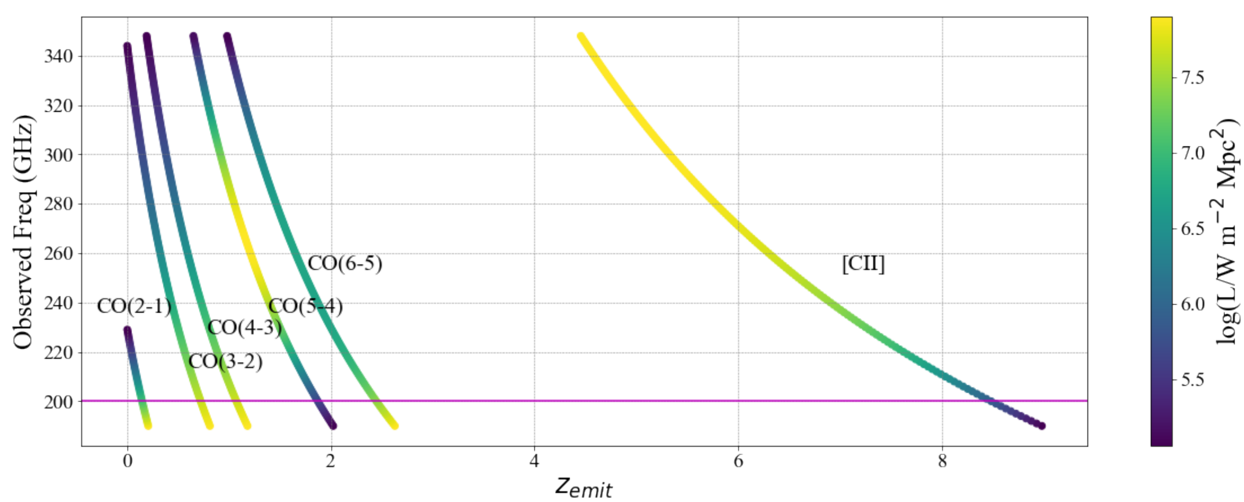

Figure 6.2: Plotted are the luminosities of CO line transitions and the [CII] transition as a function the emitted redshift and the frequency at which the line is observed. The horizontal magenta line at $\nu \sim 200$ GHz shows the lines observed at that frequency and these are the lines that are modeled for the mock observations presented in the following sections.

6.4 Simulating Instruments

6.4.1 Simulating HERA

Following the addition of foregrounds, we proceed to simulating instrumental effects. First we begin by discussing the simulation of interferometric instruments. The main goal of this module is to build $\mathbf{A}$ and $\mathbf{N}$ to produce a map estimate which we defined earlier as the following,

$$\tilde{\boldsymbol{x}} = [\mathbf{A}^{\dagger}\mathbf{N}^{-1}\mathbf{A}]^{-1}\mathbf{A}^{\dagger}\mathbf{N}^{-1}\mathbf{A}\boldsymbol{x} + [\mathbf{A}^{\dagger}\mathbf{N}^{-1}\mathbf{A}]^{-1}\mathbf{A}^{\dagger}\mathbf{N}^{-1}\boldsymbol{n}. \tag{6.23}$$

The $\mathbf{A}$ matrix is an $n_{\mathrm{Nbl}\times\mathrm{Nt}} \times n_{\mathrm{npix}}$ array of Fourier kernels,

$$A_{lm} = A_e(\boldsymbol{r}_m)\exp(-2\pi i \boldsymbol{b}_l \boldsymbol{r}_m/\lambda) \tag{6.24}$$

where Nbl refers to the number of unique baselines in the array and Nt refers to the number of times the sky was observed throughout its rotation. The noise matrix, $\mathbf{N}$ is taken to be a diagonal matrix with diagonal entries,

$$N_{ij} = \frac{T_{sys}}{\sqrt{2t_{obs}\delta\nu}}\delta_{ij} \tag{6.25}$$

where T_{sys} is the frequency dependent system temperature as defined in table 4.2, t_{obs} is the integration time, and $\delta\nu$ is the channel width, δ_{ij} is the Kronecker delta. In order to ensure that the matrix $[\mathbf{A}^{\dagger}\mathbf{N}^{-1}\mathbf{A}]$ is indeed invertible, we pick out only the diagonal elements, that is, $[\mathbf{A}^{\dagger}\mathbf{N}^{-1}\mathbf{A}]$ is in fact $\mathrm{diag}[\mathbf{A}^{\dagger}\mathbf{N}^{-1}\mathbf{A}]$.

In figure 6.3 below, we display estimated maps from different arrays of dishes in order to build some intuition for these types of observations. The input "true" sky used here is one with a single point source in the centre of the field. In the top panel, we simulate observations from a single east-west baseline and as expected we recover a vertical fringe pattern. In the middle panel, we add another dish to the array and one can see that the fringe patterns produced by each baseline interfere as expected, and the estimated sky is one with a repeating circular pattern. In the bottom panel, we simulate the observation from a more complex, 494 array of randomly placed dishes and the interference of all the baseline fringes reveals the point source in the centre. While in this first version of the simulation beam effects, time variability, and non-redundancy are omitted these effects are important to model and understand. In the upgraded version, we will use `hera_sim`, a publicly available simulation, to model instrumental systematics such as thermal noise, RFI, bandpass gains, cross-talk, and cable reflections.

6.4.2 Simulating CCAT-prime

The next instrument we simulate here is CCAT-prime which is a single dish telescope. This instrument is modelled by convolving the sky with a 2D Gaussian beam. The Gaussian beam is centered on the field and has a standard deviation equal to the diffraction limited angular resolution, that is $\sigma = \lambda_{obs}/D$ where D is the diameter of the dish. Here we make use of the convolution theorem,

$$\mathcal{F}\{f * h\} = \mathcal{F}\{f\} \cdot \mathcal{F}\{h\} \tag{6.26}$$

and perform this convolution in phase space in order to decrease the number of computations performed. Therefore the Fourier transform of the noiseless sky estimate is related to the Fourier transform of the true sky by a matrix we will call $\widehat{G}$,

$$\hat{\tilde{x}}_{[\mathrm{CII}]} = \widehat{G} \cdot \tilde{x}_{[\mathrm{CII}]} \tag{6.27}$$

which is the Fourier transform of the Gaussian beam. Therefore, both the beam and the sky are Fourier transformed, multiplied together, and the result is inverse Fourier transformed. Following this convolution, the noise contribution is computed. We compute the standard deviation of the rms noise. The reported system temperature for a beam FWHM $\theta = 0.75$ arcmin is $\sigma_{\mathrm{pix}} = 0.86$ MJy $\sqrt{s}$/sr. The pixel size corresponding a single beam is

$$\Omega_{\mathrm{pix}} = \frac{\pi\theta^2}{4\log(2)}. \tag{6.28}$$

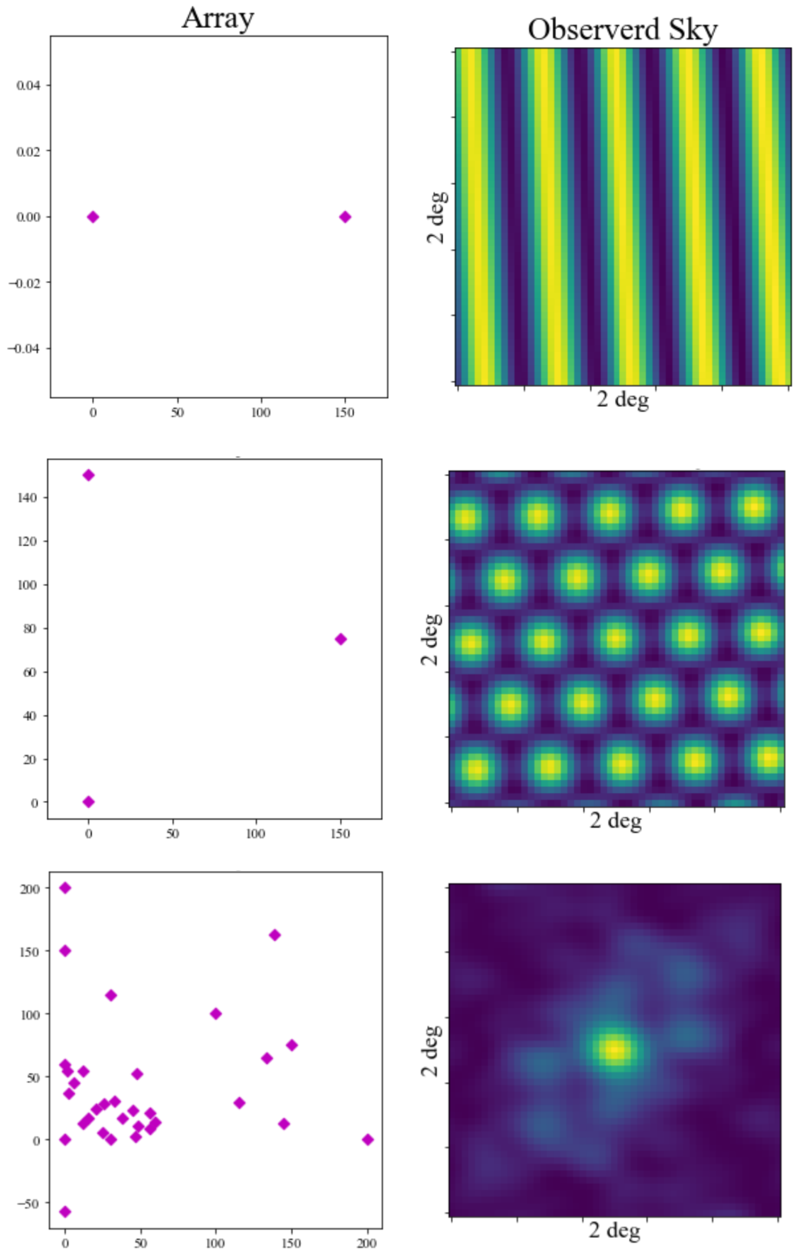

Figure 6.3: Displayed here are 3 different arrays with their observed skies. The "true" sky is simply a single point source in the center of the field. These observations are performed over a 2 deg $\times$ 2 deg patch on the sky at ν = 300 MHz. The top row shows a single baseline array and it produces a single fringe pattern. In the middle row, a 3 baseline array is shown and the observed sky is a lattice of circles which is the result of interference between the fringe patterns from the 3 baselines. In the bottom row, a 494 random array is shown and it recovers the point source in the centre.

The system temperature is then scaled according to the size of the simulated pixel, $\Omega_{\text{pix,sim}}$, relative to the CCAT-prime reported pixel size, Ω_{pix},

$$\sigma_{\text{sim}} = \frac{\sigma_{\text{pix}}}{\sqrt{\Omega_{\text{pix,sim}}/\Omega_{\text{pix}}}} \tag{6.29}$$

and the rms noise obtained by scaling σ_{sim} according to the time spent observing each pixel relative to the total integration time of the whole survey area,

$$t_{\text{pix}} = t_{\text{pix}} \frac{\Omega_{\text{pix}}}{\Omega_{\text{surv}}} \tag{6.30}$$

$$\sigma_{\text{rms}} = \frac{\sigma_{\text{sim}}}{\sqrt{t_{\text{pix}}}}. \tag{6.31}$$

Lastly, a box is populated with with random noise drawn from a Gaussian distribution with $\mu = 0$ and $\sigma = \sigma_{\text{rms}}$. This noise is then added to the convolved sky map.

6.5 First Spectra

6.5.1 Theory Spectra and Field Generation

In this section, we build a toy cosmological model in order to demonstrate the use of the tools available in this pipeline as well as to showcase the first results. The first step in this process is producing 50×50 pixel, toy cosmological fields for both the 21 cm and the [CII] line. This observation occurs at one frequency slice and will take place at $z \sim 8.5$ over ~ 4 deg^2 on the sky. This sky coverage was chosen to emulate the ~ 4 deg^2 overlap between the HERA and CCAT-prime surveys fields. At $z \sim 8.5$, this angular scale corresponds to a ~ 325 by 325 Mpc box. The theoretical spectrum of the fields is defined to be a narrow Gaussian spectrum with μ = 0.08 and σ = 0.005. The choice to have the spectrum peak at $k = 0.08$, which corresponds to a comoving scale of ~ 78 Mpc, was to ensure that enough features were realised inside of the box. This means that each realization is a relatively faithful sample of the spectrum and would be less subject to sampling errors due to cosmic variance.

We begin by generating our cosmological fields by sampling from the power spectrum and inverse Fourier transforming to obtain a box in configuration space. The output field is taken to be the 21 cm field and its brightness is scaled to have a dynamic range of a few tens of mK. This field is then inverted since the [CII] and 21 cm fields are anti-correlated during the EoR. The [CII] field brightness is then scaled to have a dynamic range of a few hundred Jy/sr. The re-scaling of the brightnesses of these fields ensures that when the foregrounds are added, their cosmological field brightnesses relative to their foregrounds are preserved. In Figure 6.4, the cosmological fields are displayed on the left panels.

In order to evaluate the theoretical statistics of this field, the auto-spectra and the cross-spectrum of these fields are computed. In Ch. 5, we derived the auto-spectrum. The cross-spectrum of two fields is computed in an analogous way but instead, we use one copy of each field,

$$P_{cross}(k) = \frac{\langle \tilde{T}_1(k)\tilde{T}_2^*(k)\rangle}{V} \tag{6.32}$$

where in our case, $\tilde{T}_1(k)$ is $\tilde{T}_{21}(k)$, $\tilde{T}_2(k)$ is $\tilde{T}_{[CII]}(k)$, and V is the volume of the overlap region of the two surveys. The auto-spectra and cross-spectrum of these fields is displayed in the right panel of Figure 6.4. As expected, the cross-spectrum is negative, indicating a negative spatial correlation between the fields. This trough is the feature we wish to recover once the cross-correlation is performed with the contaminated maps.

We expect to recover the correlated signal since we expect the spatially fluctuating foregrounds for 21 cm and [CII] to be uncorrelated as well as the instrument noises to be uncorrleated. In addition we expect the 21 cm signal to be uncorrelated with [CII] foregrounds and instrumental noise. Explicitly,

$$\langle \tilde{T}_1(k)\tilde{T}_2^*(k)\rangle = \langle (\tilde{T}_{s1}(k) + \tilde{T}_{fg1}(k) + \tilde{T}_{n1}(k))(\tilde{T}_{s2}^*(k) + \tilde{T}_{fg2}^*(k) + \tilde{T}_{n2}^*(k))\rangle \tag{6.33}$$

$$= \langle \tilde{T}_{s1}(k)\tilde{T}_{s2}^*(k)\rangle + \langle \tilde{T}_{s1}(k)\tilde{T}_{fg2}^*(k)\rangle + ... + \langle \tilde{T}_{n1}(k)\tilde{T}_{n2}^*(k)\rangle \tag{6.34}$$

$$= \langle \tilde{T}_{s1}(k)\tilde{T}_{s2}^*(k)\rangle \tag{6.35}$$

if only the signals are correlated. In an idealized case, the power spectrum estimate is expected to have no foreground and noise bias.

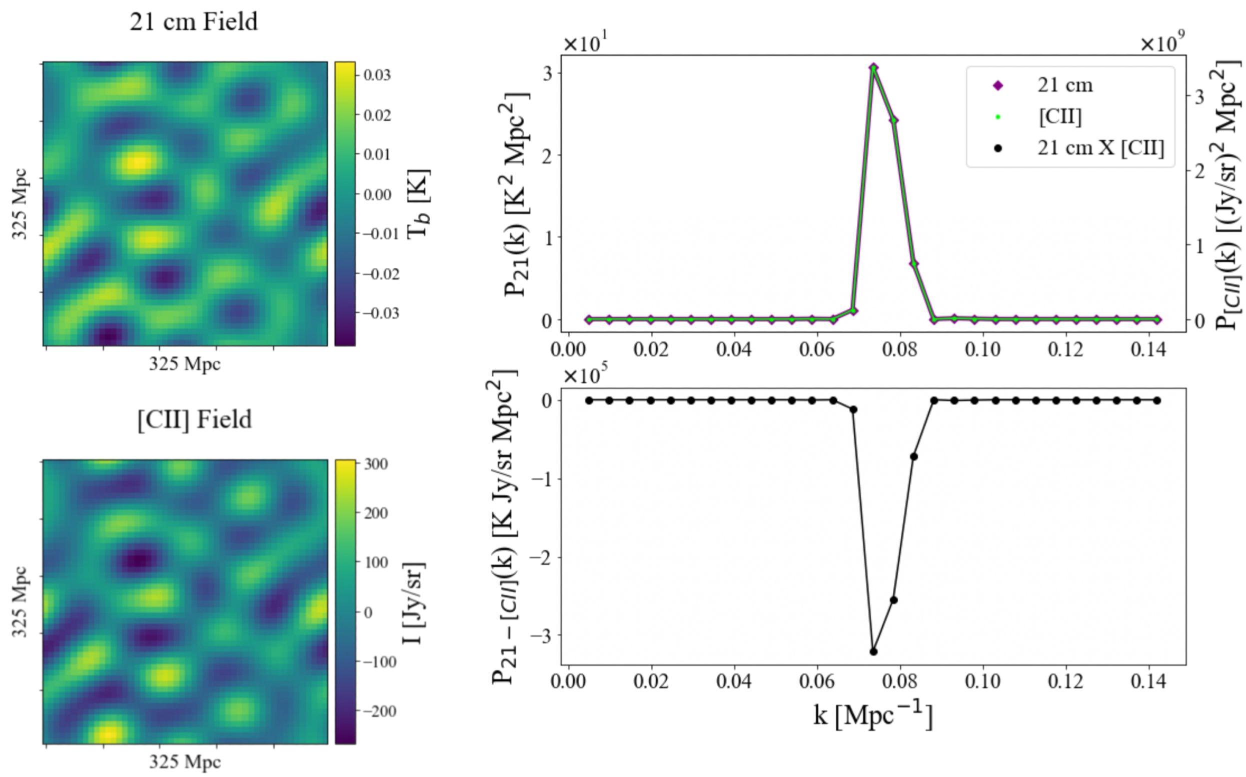

Figure 6.4: The "true" cosmological fields and statistics are shown. The top left panel displays the 21 cm brightness temperature field and the bottom left panel displays the [CII] intensity field. One may notice that the bright spots in the top field correspond to dark spots in the bottom one. On the top right panel, the auto-spectra for these fields are plotted. The 21 cm spectrum is plotted in purple and the [CII] spectrum is plotted in green. As expected, they follow the same spectral shape, though their amplitudes and units vary. The bottom right hand side panel displays the 21cm – [CII] cross-spectrum. As expected these anti-correlated fields give rise to a negative peak. All of the spectra for this field realization peak at $k = 0.75$.

After the theoretical fields are produced, we move to the theory branch of the pipeline. In this step, the window functions for all the observations are computed as well as the estimated spectra. This window function package also has the capability of estimating error bars due to spectral leakage, though this function is not used for the work done in this thesis. It is these spectra with which we compare the foreground and noise contaminated spectra in the following section. The window functions are computed as outlined in Chapter 5. For HERA, the window matrix is,

$$\mathbf{S} = \mathrm{diag}([\mathbf{A}^{\dagger}\mathbf{N}^{-\mathbf{1}}\mathbf{A}]^{-\mathbf{1}})\mathbf{A}^{\dagger}\mathbf{N}^{-\mathbf{1}}\mathbf{A} \tag{6.36}$$

$$\mathbf{W}_{\mathrm{HERA}} = \widehat{\widehat{\mathbf{S}}}\widehat{\widehat{\mathbf{S}}}^{*}. \tag{6.37}$$

For CCAT-prime, we use the Fourier transform of the Gaussian beam, $\widehat{\mathbf{G}}$, unfurled along the diagonal of an $n_{\mathrm{pix}} \times n_{\mathrm{pix}}$ matrix. We will continue to use the notation $\widehat{\mathbf{G}}$ to denote this unfolded, diagonal version. This construction ensures when the Fourier transform of the pixel brightnesses of the [CII] field are unfurled into a 1D array, the estimated Fourier transform of the sky is once again recovered,

$$\begin{bmatrix} \hat{\hat{x}}_1 \\ \vdots \\ \hat{\hat{x}}_n \end{bmatrix} = \begin{bmatrix} \widehat{G}_1 & 0 & \dots \\ \vdots & \ddots & \\ 0 & & \widehat{G}_n \end{bmatrix} \begin{bmatrix} \hat{x}_1 \\ \vdots \\ \hat{x}_n \end{bmatrix}. \tag{6.38}$$

The window matrix for CCAT-prime is therefore,

$$\mathbf{W}_{\mathrm{CCAT-p}} = \widehat{\mathbf{G}}\widehat{\mathbf{G}}^{*}. \tag{6.39}$$

Lastly, the cross-spectrum is estimated using a joint window function which is analogous to the way the cross-spectrum is computed. Since the cross-spectrum is computed using one copy of the brightness temperature of 21 cm as seen by HERA, and one copy of [CII] intensity as seen by CCAT-prime, the estimated spectrum is the following

$$\tilde{\mathbf{P}} = \frac{\langle \widehat{\widehat{\mathbf{S}}}\hat{x}_{21}\widehat{\mathbf{G}}^{*}\hat{x}^{*}_{\mathrm{[CII]}} \rangle}{V} = \widehat{\widehat{\mathbf{S}}}\widehat{\mathbf{G}}^{*}\frac{\langle \hat{x}_{21}\hat{x}^{*}_{\mathrm{[CII]}} \rangle}{V} \tag{6.40}$$

and the joint window function matrix is

$$\mathbf{W}_{\mathrm{cross}} = \widehat{\widehat{\mathbf{S}}}\widehat{\mathbf{G}}^{*}. \tag{6.41}$$

6.5.2 Results

In this section we present the results of the cross-spectrum analysis pipeline. To recapitulate, the theory spectra in Figure 6.4 are piped through the the foreground step and the relevant foregrounds for each probe are added. At $z \sim 8.5$, the 21 cm observation is made at 150 MHz and the [CII] observation is made at ~ 200 GHz. The 21 cm foreground contaminated field is then observed by the 350 dish HERA array, the map estimator is applied to the visibilities, and instrumental noise is added. The noise is drawn from a Gaussian with $\mu = 0$ and $\sigma = 8$ Jy in accordance with recent HERA data. Similarly, the foreground contaminated [CII] map is piped through its instrument simulation module and instrument noise is added. Once both maps are produced, their auto-spectra and cross-spectra are computed.

In Figure 6.5 we present these results. The columns, from left to right, contain 21 cm auto-spectra, [CII] auto-spectra, and 21 cm – [CII] cross-spectra. The rows labelled 'A','B','C', and 'D' denote different scenarios. Row 'A' contains the window estimated spectra and these are the spectra with only instrumental effects without any noise or foreground contaminants. These are the spectra that the subsequent ones should be compared to. The 21 cm estimated spectrum does spread power to different k modes, in particular to the low k modes. The instrument also inflates the amplitude of the spectrum compared to the raw theory spectrum. The same is true of the [CII] window function estimated spectrum, though the spectral leakage occurs only in the modes very close to the peak. The cross window function estimated spectrum is sharply peaked at $k = 0.075$ and it is this peak that we wish to recover in the subsequent contaminated scenarios.

The second row labelled 'B' contains the spectra in the case where only instrument noise is added without any foregrounds. The 21 cm auto-spectrum has now lost its peak and the spectrum is completely dominated by instrument noise, in particular at the low k modes. The [CII] spectrum is less biased by its instrumental noise, though there is a slight shift in power to the highly peaked mode. In both cases, the amplitude of the spectra are biased by instrument noise as expected, since the pixel brightnesses estimated are inflated. In the rightmost plot in row 'B', the cross-spectrum reveals the peak that was lost in the 21 cm power spectrum. The correlated modes create a deep negative peak as expected. Compared to the window function estimate of the cross spectrum, the peak is broadened and its amplitude is increased in the negative direction due to noise bias.

In row 'C', both foreground contaminants and instrument noise are modelled and the sky is observed over one night. In this scenario, the 21 cm power spectrum has a large peak due to galactic synchrotron radiation. This peak dominates over all the others. The [CII] auto-spectrum still contains an observable signal, again biased by systematics. Additionally, there are foreground biased modes at both low and high k. Since the [CII] foreground modelling does not take into account spatial clustering, the spatial characteristics of these foregrounds are akin to those of white noise, thus leading to a flat spectrum. In the rightmost plot of row 'C' the cross-spectrum is computed. Most notably, the negative peak is once again recovered, though its amplitude is again biased by systematics. Still, the cross-spectrum remains a robust statistic for the location of the correlated modes. Once again, there remain foreground correlations due to the fact that the Bremsstrahlung emission, unresolved point source background, and CO line interloper intensity fields have no spatial characteristics that have been modelled. The spatial distribution of pixels, for all of these maps is random and the spectra are therefore relatively flat. The last row 'D' depicts the same scenario as row 'C' except we consider a larger N limit where 100 different cosmological realizations are observed for one night each, and their spectra averaged together. Since these are 100 independent observations, a new instrument noise realization is generated for each cosmological realization as well. The same foreground realization is added to each of the observations. Therefore, the error bars have noise, and cosmic variance contributions. The 21 cm spectrum is effectively the same as row 'C' though its amplitude is increased. The [CII] spectrum is increasingly biased by systematics, though the amplitude is decreased to be of the same order of magnitude as the window function estimated spectrum albeit with significant error bars. The last cross-spectrum is once again able to recover the negative peak at a lower amplitude relative to the foreground biased modes which do not increase in amplitude from row 'C'. One thing to note is that the foreground modes have smaller error bars than the cosmological signal mode. Since the same foreground realization was used in all 100 simulations, the foreground modes (i.e. the ones not at k = 0.75) have error bars only characterized by instrument noise. The signal trough's error bar has an instrument noise contribution as well as a cosmic variance contribution since each of the 100 simulations used a different cosmological field.

As a null test, the spectra of row 'C' were computed without a cosmological field present. The results are presented in Figure 6.6. The plot on the left is of the 21 cm foreground and noise observation. One can see that in addition to the low-k peak due to galactic synchrotron radiation, the foreground and noise spectrum also has power at higher k modes. In the middle plot, it is now plain to see that the [CII] foreground and noise realization have a relatively flat spectrum peaking at almost every wave-number. As a result, one can notice in the right plot of the cross-observation spectrum there is a slight positive correlation at the $k = 0.075$ mode, the mode that contains the signal in the cosmological field. This therefore indicates that the negative peak recovered at $k = 0.075$ in Figure 6.5 is in fact the result of the anti-correlation between the [CII] and 21 cm fields.

6.5.3 Next Steps

The results of this preliminary analysis are promising and serve as a proof of concept that cross-correlations in LIM may be a useful tool in extracting power spectrum information from otherwise heavily contaminate data sets. Still, there are many ways in which this pipeline an be improved upon. To begin, the input cosmological fields can be ameliorated with more realistic modeling. A challenge here is that since field correlations must be preserved, the brightness temperature fields of all probes considered must be simulated from a common density field. Such efforts are currently underway though are still in development phase. LIM-Fast is one such line intensity map simulator and now has the ability to simulate ~ 100 different lines using semi-empirical models [146]. This may be a tool that can be employed here. In addition, while the work here was done at a single frequency slice, we are currently working to extend this pipeline to process 3D data cubes, making use of line-of-sight spectral information. In addition, it is clear from this work that more realistic foreground models are needed, particularly ones that contain

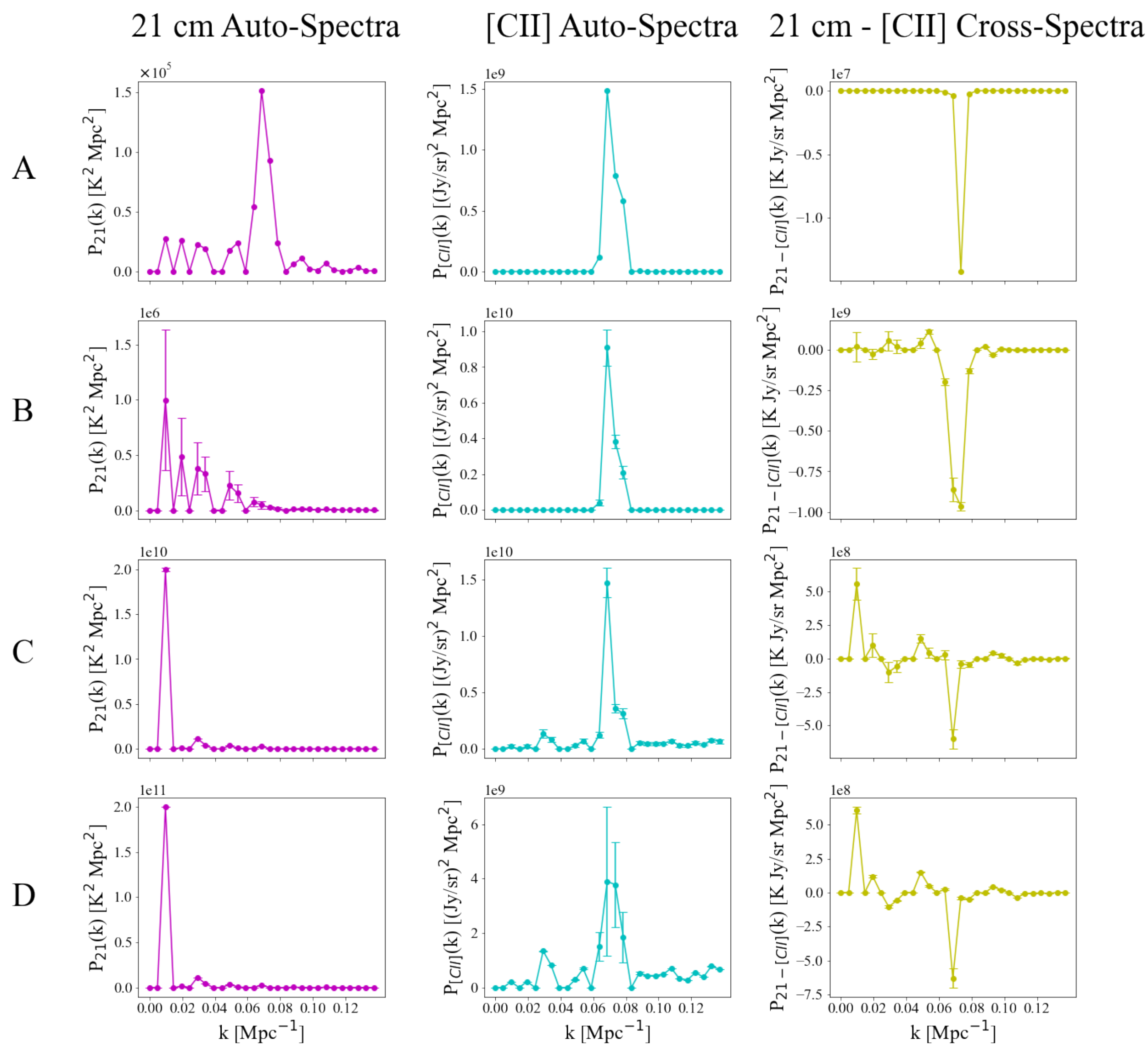

Figure 6.5: Displayed in each column, from left to right, are the 21 cm auto-spectra in magenta, the [CII] auto-spectra in cyan, and the 21 cm – [CII] cross-spectra in yellow. Row 'A' contains the window function estimated theory spectra. Row 'B' contain spectra from observations of the cosmological field with the addition of instrument noise observed over 1 night. Row 'C' contain spectra from observations of the cosmological field with the addition of instrument noise as well as foregrounds observed over 1 night. Row 'D' contain spectra from 100 realisations of the cosmological field with noise and foregrounds each observed for 1 night and averaged together.

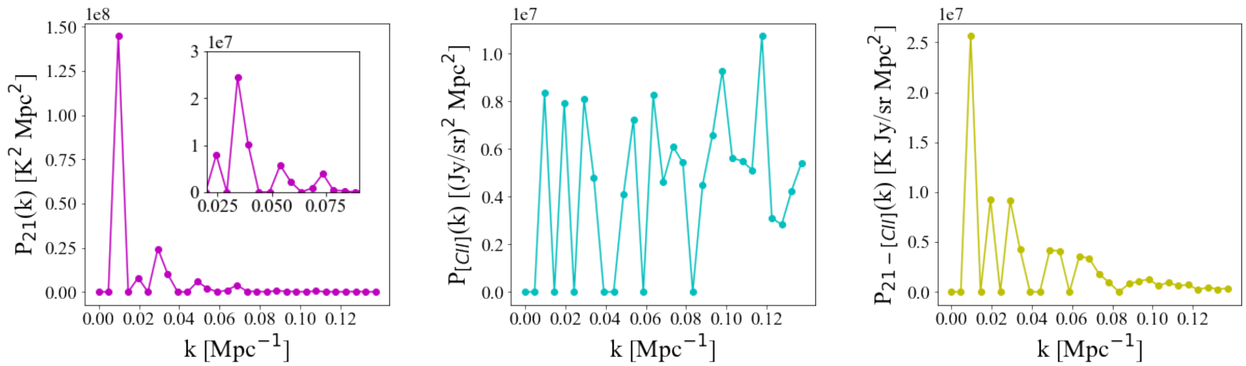

Figure 6.6: Plotted here are the result of a simple null test where the observation of row 'C' of Figure 6.5 is repeated without the inclusion of the cosmological field. In the left plot, the 21 cm foreground and noise spectrum is plotted. There is a zoomed in section to indicate that power at high k is present. In the middle plot, the [CII] foreground and noise spectrum is plotted. The right plot shows the cross-spectrum of both the observations' systematics.

clustering information for [CII] line interlopers. There were also certain contaminants that were omitted such as radio frequency interference (RFI) and extended sources which can be included in updated versions of this pipeline. And of course, a long term goal for this research program is to extend this framework to involve other probes, such as CMB observations and near-infrared observations, which can also be cross-correlated with the 21 cm line.

Chapter 7

FRB Cosmology

7.1 Introduction

The Epoch of Reionization (EoR) is a transitional period in our Universe's history when the neutral hydrogen (HI) making up the intergalactic medium (IGM) was ionized by the first generation of stars and galaxies. The Cosmic Microwave Background (CMB) has given us a peek into the early universe and measurements of quasars at $z < 7$ teach us about early galaxy evolution. Cosmic dawn and the EoR remain the missing piece of our understanding at $z_{\rm CMB} > z > 7$. Understanding this period not only provides insight into the very early universe, but also teaches us about the first generation of stars and galaxies. The timing, mechanisms, and morphology of the EoR are poorly constrained despite its importance to our understanding of the Universe. A number of observational probes have began placing limits on the EoR through the 21cm line [8, 9, 34, 66, 118]. The advantage of using this line as a direct probe IGM during the EoR is that neutral hydrogen is abundant in the early Universe and that, by measuring the redshifting of this photon, we can trace primordial hydrogen along the line of sight. For a comprehensive review of 21cm cosmology, the reader is encouraged to read [105], [52], [130], [87] and [84].

21cm cosmology, however, does not come without its challenges. Making a detection of the 21 cm line during the EoR is exceptionally difficult since the frequency of the line is redshifted into the 50-300 MHz range [84]. Systematics, radio frequency interference (RFI), galactic synchrotron emission, and radio bright sources have made the 21 cm signal difficult to measure, and thus limit our ability to constrain the astrophysics during this epoch [86]. As a result, many look to other probes of the EoR.

Fast Radio Bursts (FRBs) are a class of bright, millisecond duration, radio transients that have been detected at frequencies ranging from 110 MHz to 1.5 GHz with dispersion measures (DMs) lying between 110 and 2600 pc cm^{-3} [121,125]. Thanks to current and upcoming broad-band wide-field-of-view instruments, such as the Canadian hydrogen Intensity Mapping Experiment (CHIME; [3]), Five-hundred metre Aperture Spherical Telescope (FAST; [110]), and Australian Square Kilometer Array Pathfinder (ASKAP; [65]), we have seen a large increase in the number of FRBs detected. It is estimated that when SKA is online, its event detection rate may be as high as $\sim$1000 FRBs sky^{-1} day^{-1} [47].

Since their discovery by [89], the number of FRBs detected has increased tremendously. CHIME alone has detected over 1000 bursts since 2018. While one source has now been localized within the Milky Way ([21]), the vast majority of FRBs remain extragalactic sources and can thus probe out to cosmological distances [38,67]. Many questions remain about the astrophysical origin of these bursts as well as their intrinsic distribution out to high DM [75,90,124].

While the progenitor of FRBs remains unknown, the DMs of these bursts are, on the contrary, well understood and could thus prove yet another direct probe of the IGM during the EoR. The DM of an FRB is defined as the integrated column density of free electrons along the line of sight from source to observer. As the FRB travels through the IGM, it experiences a frequency dependent time delay, $\Delta t \propto \nu^{-2}$DM. DM is given by

$$\mathrm{DM}(\mathbf{x}, z) = \int \frac{n_e(\mathbf{x}, z)}{1+z} dl, \tag{7.1}$$

where dl is the line element along the light of sight, $n_e(\mathbf{x}, z)$ is the free electron density at comoving position $\mathbf{x}$ and redshift z. Measuring the DM of an FRB at redshift z can therefore probe the integrated number density of free electrons along the line of sight in the IGM. To evaluate 7.1 for each reionization scenario, we express the line element dl in terms of the Hubble parameter

$$dl = cdt = \frac{-cdz}{H(z)(1+z)} \tag{7.2}$$

where $H(z)$ is given in terms of the ΛCDM parameters through

$$H(z) = H_0\sqrt{\Omega_m(1+z)^3 + \Omega_\Lambda} \equiv H_0 E(z). \tag{7.3}$$

The free electron number density in the IGM can be written as a function of the ionization and density field,

$$n_e = \frac{\mathrm{f_H f_{IGM}}\Omega_m \rho_0(z)}{m_{\mathrm{H}}}(1+z)^3(1+\delta(\mathbf{x},z))x_{\mathrm{HII}}(\mathbf{x},z), \tag{7.4}$$

where $\mathrm{f_H}$ is the fraction of baryonic matter that is hydrogen, $\mathrm{f_{IGM}}$ is the fraction of hydrogen that is found in the IGM, $\mathrm{m_H}$ is the mass of hydrogen and ρ_0 is the mean density of the IGM at redshift z. The dispersion measure of FRBs detected after the EoR can be approximated to be $x_{\mathrm{HII}}(\mathbf{x}) = 1$, i.e. the IGM is entirely ionized. Note that helium reionization does increase the number density of free electrons at low redshift ($z \sim 2$), however this is independent of the reionization model. Therefore, we do not take this into account in our models for Equation 7.1. For interested readers, there is a growing body of literature on constraining helium reionization using the DMs of FRBs [7, 17, 80, 168]. Unlike at low redshift, the ionization field x_{HII} during the Epoch of Reionization is patchy, composed of regions of ionized bubbles and neutral regions, whose placements and evolution depend highly on the astrophysics governing reionization. In this case, the number density of electrons n_e will dependent on the state of the ionization field. High redshift FRBs detected during the Epoch of Reionization will therefore be sensitive to the astrophysics that have imprinted itself onto x_{HII}.

Furthermore, referring to Equation 7.4, the number density of free electrons is dependent on the product of the density and ionization field $x_{\mathrm{HII}}\delta$. The method in which the ionization field x_{HII} maps to the underlying density field δ is known as the density-ionization correlation, which affects the morphology of the EoR. The cross term in Equation 7.4 contains information of the density-ionisation correlation, which affects the observed DM of an FRB. Most EoR models predict morphologies where the ionized regions are not random with respect to the underlying density field. Instead, there are two extreme ways in which the ionization field couples to the density field. The density field can be positively correlated to the ionization field. In this scenario, overdense regions correspond to high ionization fraction. In this model, ionizing sources ionize their immediate surroundings before ionizing the lower density regions of the IGM. We say that reionization happens 'inside-out'. The second extreme model is the scenario where the underlying density field δ is negatively correlated with the ionization field x_{HII}. In this scenario, the ionizing sources first ionize the low density regions before ionizing the high density regions. We say that reionization happens 'outside-in'. In this model, the high density regions in δ correspond to regions of low ionization fraction in x_{HII}. This model usually requires the recombination of hydrogen atoms in high density regions to dominate the effects of UV ionization [22, 102, 162]. Outside-in morphologies can also be achieved by having reionization driven by x-ray photons, which can more easily "leak" into the underdense regions of the IGM [98, 101]. It is also possible for reionization to unfold as a combination of both inside-out and outside-in, in which case, the correlations between δ and x_{HII} are statistical combination of the inside-out and outside-in models [51, 93].

The way in which the mean DM depends on the broad timeline of the reionization history has been previously studied [6, 56, 91, 166]. Most recently, [56] show that one year's worth of observing with SKA phase 2 can reveal our cosmic reionization history, and [6] show that both DM and the differential FRB source count distribution prove useful probes of reionization even with limited redshift information. In this paper we build on the techniques outlined by these authors by performing a study of how the morphology, astrophysics and evolution of the EoR affect the mean DM of high redshift FRBs. We use a set of astrophysical and morphological parameters to bracket the physical range of EoR scenarios and study how DM–z probability distributions and the mean DM of FRBs at each redshift depend on these parameters. We then forecast the types of constraints that we can place on the EoR using measurements of the DMs of high redshift FRBs. Since FRBs at high redshift have yet to be observed, we create a mock sample of highly

Table 7.1: Summary of Reionization Parameters and FRB Observables

Symbol	Parameter Name	Description/Definition
$z_{\rm EoR}$	Reionization Redshift	The redshift indicating the onset of reionization
β	Morphological Parameter	Determines the correlation between δ and $x_{\rm HII}$
$M_{\rm turn}$	The Turnover Mass	Halo mass scale in which star formation is efficient
ζ	Ionizing Efficiency	Number of ionizing photons released per stellar baryon
$R_{\rm mfp}$	Radius of The Mean Free Path	Maximize size of the ionized regions
$\mathrm{DM}(\mathbf{x}, \mathrm{z})$	Dispersion Measure	DM of an individual FRB at redshift z along a single line of sight
$\overline{\mathrm{DM}}(z)$	Mean Dispersion Measure	Mean DM of a collection of FRBs observed at redshift z

dispersed FRBs under a fiducial reionization model and forecast the type of constraints one can place on the astrophysics and morphology of the EoR given such a measurement. We perform this forecast with 10^2, 10^4, and 10^5 high DM samples.

This chapter is structured as follows. In Section 7.2 we describe the astrophysical and morphological parameters used in our simulation to bracket the physical range of EoR scenarios. In Section 7.3 we discuss how the mean DM and the DM probability distributions of high redshift FRBs depend on these parameters. In Section 7.4, we describe our fiducial reionization model, the mock FRB measurements made for this reionization scenario. We forecast the constraints that can be placed on the EoR parameters using such a measurement and in Section 7.5 we present the results. We summarize our conclusions in the concluding chapter. Throughout this work we set the ΛCDM parameters to $\sigma_8 = 0.81$, $\Omega_m = 0.31$, $\Omega_b = 0.048$, $h = 0.68$ [123].

7.2 Simulation

To generate density and ionization boxes representative of different EoR models we use `21cmFAST` package [99]. Density fields are obtained through the Zeldovich approximation while ionization and halo boxes implement the excursion set formalism of [53]. For further details about how `21cmFAST` generates reionization models see [99]. Throughout this paper we use high resolution boxes of 800^3 voxels corresponding to a comoving side length of $300\,\mathrm{Mpc}$ and coarser boxes of 200^3 voxels corresponding to the same comoving side length.

7.2.1 EoR Parameters

We use `21cmFAST` to generate different EoR scenarios by varying a number of adjustable parameters which encapsulate variations in the detailed astrophysics of reionization. We bracket the physical range of EoR scenarios by adjusting the parameters $M_{\rm turn}$, $R_{\rm mfp}$, and ζ. Physically, the turnover mass, $M_{\rm turn}$, determines the mass of a halo in which star formation is efficient. Values of $M_{\rm turn} \simeq 5 \times 10^8 M_\odot$ correspond to a virial temperature of $T_{vir} \simeq 10^4$. Values below $M_{\rm turn}$ have exponential suppression in star formation. Roughly, this sets the mass scale for the ionizing sources. The unitless astrophysical parameter ζ, determines the ionizing efficiency of the sources. This parameter is an amalgamation of other parameters which describe the small scale astrophysics of the UV sources. A large value of ζ will imply more ionizing photons per stellar baryon, while a smaller ionizing efficiency will entail less ionizing photons are emitted for each ionizing source. The cutoff-radius $R_{\rm mfp}$ sets the maximum size of the ionized bubbles [142]. Variation of these parameters effect the timing and duration of reionization, and have been studied in previous works [42,69,82,117,127]. For this work, we use these parameters to generate a wide variety of EoR models that bracket physical scenarios. The `21cmFast` simulation operates under an inside-out reionization formalism in which the density field δ is correlated with the ionization field $x_{\rm HII}$ and therefore do not capture the different δ $x_{\rm HII}$ correlations indicative of different EoR morphologies. Therefore in order to study the effects of morphology, we input it by hand using a parameter, β. In the next Section we introduce a parametrization that extends the physical scenarios bracketed by the astrophysical parameters to EoR morphologies of arbitrary ionization-density correlations.

7.2.2 Morphological Parametrization of the EoR

To simulate EoR scenarios where the density field and ionization field are correlated by some arbitrary amount, we use the β parametrization introduced in [116]. This parameter continuously tracks the correlation between $x_{\rm HII}\delta$. We briefly describe this parametrization here. The β parameter has bounds $-1 \leq \beta \leq 1$ and controls the amount of correlation between $x_{\rm HII}$ and δ. The sign of β indicates the overall sign of the correlation between $x_{\rm HII}$ and δ. Positive values of β, indicate a positive correlation between density and ionization fields, and so overdense regions in δ couple to regions of high ionization fraction in $x_{\rm HII}$. This sign of correlation is indicative of inside-out reionization scenarios, where the overdense regions of the IGM are first to be ionized. Conversely, negative signs of β indicate an overall negative correlation between ionization field and density field so that overdense regions in δ correspond to regions of low ionized fraction of hydrogen. This is indicative of outside-in reionization, where overdense regions of the IGM are last to be ionized. The magnitude, $|\beta|$, indicates how strong that correlation sign is between ionization and density fields. A value of $\beta = 0$ indicates a random placement of the ionized regions, in which case there is no correlation between ionization and density fields. As we increase β from 0 to 1, the relative likelihood of finding overdense regions of δ corresponding to ionized regions in $x_{\rm HII}$ increases, until finally at β of 1, all overdense regions in δ always correspond to regions of ionized hydrogen. Similarly, as we decrease β from 0 to -1, the relative likelihood of finding overdense regions of δ corresponding to ionized regions in $x_{\rm HII}$ increases until at $\beta = -1$, all overdense regions in δ correspond to regions of low $x_{\rm HII}$. The intermediate, non-extreme values of β, i.e. $-1 < \beta < 1$ indicate reionization scenarios that contain the statistics of both inside-out and outside-in. Figure 7.1 demonstrates the affect of inside-out, or outside-in reionization, on the free electron number density n_e in the IGM. For a more detailed discussion on this parametrization, the reader is encouraged to read [116]. Table 7.2 summarizes the terminology used to describe the type of correlation as well as the model to which it pertains. The β parameter encodes only the correlation statistics between density and ionization fields and is treated as independent from the other EoR parameters in our models. This makes β phenomenological

Table 7.2: Lexicon for physical models and their respective correlations

β	Correlations between x_{HII} δ	Physical Model
1	Correlated	Inside-out
$1 < \beta < 0$	Increasingly correlated	Mostly inside-out
0	uncorrelated	Random
$0 > \beta > -1$	Increasingly anti-correlated	Mostly outside-in
-1	Anti-correlated	Outside-in

compared to the other parameters. Although β is a not a physically derived quantity, it correctly predicts the statistics for different density-ionization correlations. In the following Section we shall see that our models only use the statistics of DMs, and so our results do not depend on the physical nature of β.

7.2.3 Dispersion Measure

The observed dispersion in Equation 7.1 is sensitive to all sources of free electrons encountered by the radio burst as the electromagnetic wave travels from source to observer. This includes the free electrons found within the host galaxy as the FRB leaves the source, as well as the free electrons encountered in the Milky Way (MW) as the FRB arrives to the observer. The FRB also has exposure to the free electrons found in the circumgalactic medium (CGM) and IGM. We split Equation 7.1 into its respective components

$$\mathrm{DM_{obs}}(\mathbf{x}, z) = \mathrm{DM_{host}} + \mathrm{DM_{MW}} + \mathrm{DM_{CGM}}(\mathbf{x}, z) + \mathrm{DM_{IGM}}(\mathbf{x}, z). \tag{7.5}$$

The dispersion $\mathrm{DM_{IGM}}(\mathbf{x}, z)$ is due to the free electrons found in the IGM between the FRB source and the observer. This is the DM attributed to cosmic reionization and is the DM of interest in order study the evolution of x_{HII}. The DM attributed to the host galaxy, MW and CGM are subject to uncertainties surrounding the gas dynamics within these regimes, and as a result make them difficult to model. We treat them as contaminants in our measurement of the contributions of $\mathrm{DM_{IGM}}$ to $\mathrm{DM_{obs}}$. The DM contribution due to the interstellar medium (ISM) of intervening galaxies have also been shown to be negli-

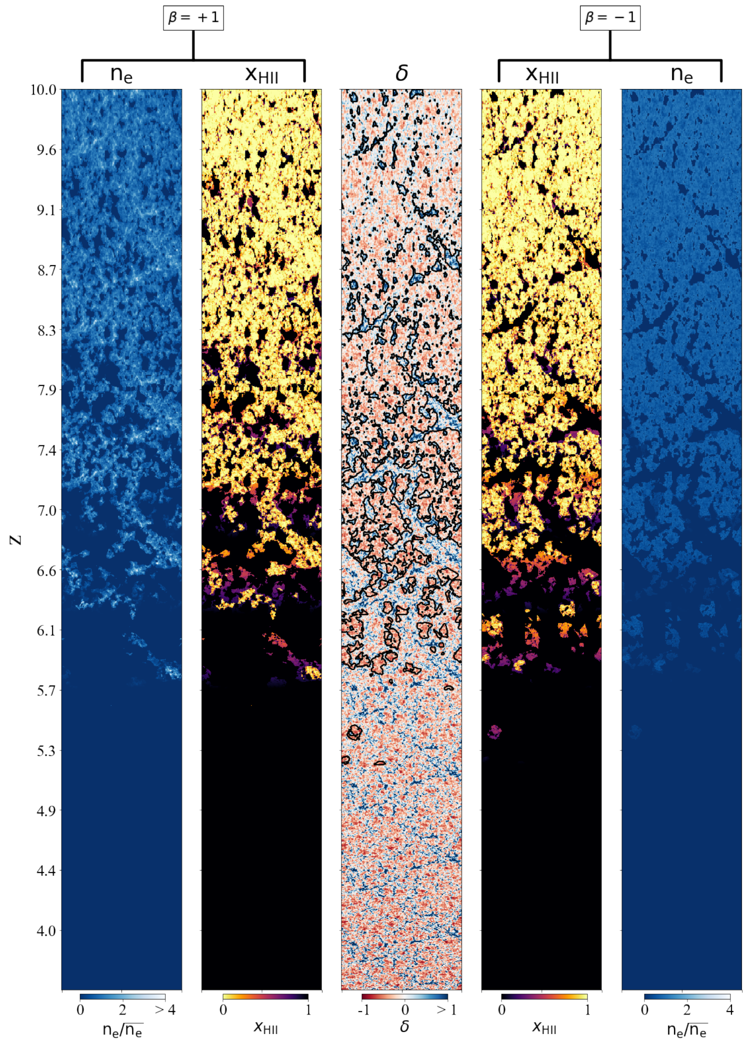

Figure 7.1: From the center of the figure outward: Lightcones of the density field δ, ionization fraction $x_{\rm HII}$ and free electron field n_e for the case of inside-out reionization (left three boxes) and outside-in reionization (right three boxes). Inside-out reionization (left) leads to a higher free electron number density n_e in the ionized bubbles since the density field (center) couples to the ionized regions in $x_{\rm HII}$ compared to outside-in models (right) where the underdense regions in δ couple to the ionized regions in $x_{\rm HII}$.

gible [131]. The inhomogeneity of $x_{\rm HII}$, δ and the gas dynamics as a function of position $\mathbf{x}$ make it unreasonable to draw conclusions on the state of the IGM through a single line of sight. We instead compute the mean value of $\mathrm{DM_{obs}}$ due to all sightlines. This removes single line of sight fluctuations in δ and $x_{\rm HII}$ as well as averages over the contributions due to the CGM. With the assumption that the different contributions to the $DM_{\rm obs}$ are uncorrelated with each other we obtain,

$$\overline{\mathrm{DM}}_{\rm obs} = \overline{\mathrm{DM}}_{\rm host} + \overline{\mathrm{DM}}_{\rm MW} + \overline{\mathrm{DM}}_{\rm CGM} + \overline{\mathrm{DM}}_{\rm IGM}. \tag{7.6}$$

Studies such as [68] model the DM contribution of the Milky Way. Other studies have found that the photon incurs an average DM of $\overline{\mathrm{DM}}_{\rm MW} \sim 200\mathrm{pc\ cm^{-2}}$ when leaving the MW and host galaxy [153, 158]. We treat the average contribution of the MW and host galaxy to $\overline{\mathrm{DM}}_{\rm obs}$ as an offset $\sim 200\mathrm{pc\ cm^{-2}}$.

$$\overline{\mathrm{DM}}_{\rm obs} - (\overline{\mathrm{DM}}_{\rm host} + \overline{\mathrm{DM}}_{\rm MW}) = \overline{\mathrm{DM}}_{\rm CGM} + \overline{\mathrm{DM}}_{\rm IGM}. \tag{7.7}$$

We assume high redshift FRBs have $\overline{\mathrm{DM}}_{\rm obs}$ dominated by the IGM, we neglect the contribution due to the CGM for this work although there may be some evidence that the CGM contribution is ~ 200 pc cm^{-3} [28]. The remaining fluctuations in DM are attributed to cosmic reionization. Henceforth we refer to $\mathrm{DM_{IGM}}$ as $\mathrm{DM_{obs}}$. This model isn't meant to be overly realistic, we intend to capture first order effects due to $\mathrm{DM_{IGM}}$. In order for precise measurements to be made of the impact that the EoR has $\overline{\mathrm{DM}}_{\rm obs}$, a method to subtract out the effects due to the CGM needs to be studied. We leave such a study to future work. The mean DM of a high redshift FRB observed at redshift z due to free electrons in the IGM is then evaluated using Equation 7.1 as

$$\overline{\mathrm{DM}}_{\rm obs}(z) = -\int c dz \frac{\mathrm{f_H f_{IGM}}\Omega_m \rho_0 (1+z)}{m_{\rm H} H_0 E(z)} \left(\overline{x}_{\rm HII}(z) + \overline{\delta x}_{\rm HII}(z)\right). \tag{7.8}$$

The $\overline{\mathrm{DM}}_{\rm obs}$ of high redshift FRBs will be proportional to the mean ionization fraction $\overline{x}_{\rm HII}$ of the IGM as well as to the mean product $\overline{x_{\rm HII}\delta}$. This cross term captures the density-ionization correlation of the EoR which describes how the underlying density field δ couples to the ionization field x_{HII}. The β parameter quantifies the different possibilities of this correlation. The astrophysics of the EoR affect both of these terms. Since the astrophysics sets the size and morphological features of the ionization field x_{HII}, they too have consequences for $\overline{\mathrm{DM}}$. In addition, the astrophysics of the EoR determine the onset and duration of the EoR, i.e. they determine the mean ionization fraction $\overline{x}_{\mathrm{HII}}$ at each redshift z. Previous studies have looked at how broad modeling the mean ionization fraction $\overline{x_{\mathrm{HII}}\delta}$ to redshift affects the observed DM of high redshift FRBs, i.e. the $\overline{x_{\mathrm{HII}}\delta}$ term in Equation 7.8 [166]. Here we build on that by including both terms and studying how the detailed astrophysics as well as density-ionization correlation affect both terms. For readers who are less familiar with the parameters that have been discussed, they are summarized in Table 7.1 for easy reference. In the following Sections, we study how the astrophysical parameters, and the β parameter, which parameterizes the density ionization correlation, affect $\overline{\mathrm{DM}}_{\mathrm{obs}}$.

In the following section, we evaluate Equation 7.8 by simulating 10^5 sightlines, computing the individual DM of each sightline, and by averaging the DMs. This is done for each reionization model.

7.3 Models

Equation 7.8, states that $\overline{\mathrm{DM}}_{\mathrm{IGM}}$ of an FRB depends on the cumulative of both the mean ionization fraction, $\overline{x}_{\mathrm{HII}}$, and the density-ionization correlation, $\overline{x_{\mathrm{HII}}\delta}$, along the line of sight. If z_{EoR} is the redshift in which the IGM becomes increasingly neutral, then $\overline{x}_{\mathrm{HII}} = 1$ for all $z < z_{\mathrm{EoR}}$ and so the relationship between $\overline{\mathrm{DM}}_{\mathrm{IGM}}$ and z is linear up until the onset of reionization [27]. The linear relationship breaks down at z_{EoR} since $\overline{x}_{\mathrm{HII}}$ decreases rapidly due to the increasingly neutral IGM. As a result, the EoR produces a flattening of $\overline{\mathrm{DM}}$ for high redshift FRBs. The shape and positioning of this flattening is highly dependent on the onset, duration and morphology of reionization. In this Section we use the astrophysical and correlation parameters to study how EoR models affect the DM of FRBs observed in the EoR. We consider the distribution of DM at each z of the individual DM sightlines as a function of the astrophysics and morphology of the EoR. In Section 7.5, we forecast

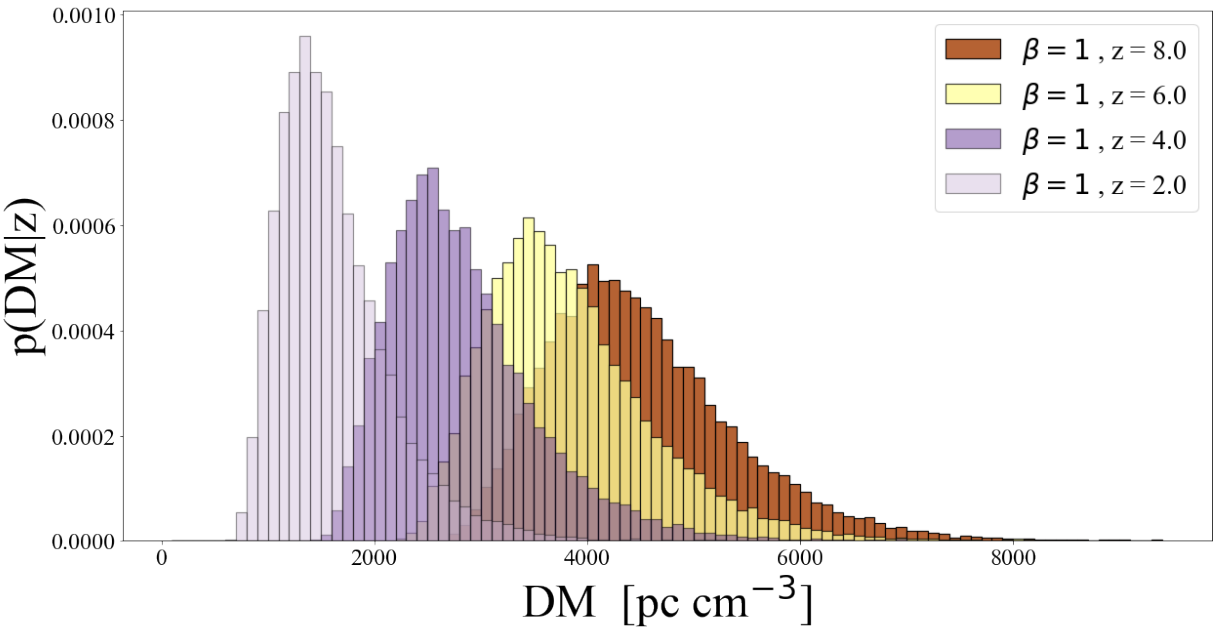

Figure 7.2: Redshift evolution of the DM probability distributions for our fiducial reionization scenario $\beta = 1$, $\zeta = 25$, $M_{\rm turn} = 5 \times 10^8 \mathrm{M}_\odot$ and $R_{\rm mfp} = 30\mathrm{Mpc}$. At higher redshift the relative probability of high DM sightlines increases.

that the constraints that can be placed on these parameters through measurement of high redshift FRBs.

7.3.1 DM Distributions

We consider the distribution of the individual DM sightlines as a function of the astrophysics and morphology of the EoR. FRBs observed at low z are more likely to have low DM sightlines due to less chance of interactions with free electrons in the IGM. From Figure 7.2 we see that the resulting DM probability distribution is highly non-Gaussian and skewed to low DM. Note that the contaminants $\overline{\mathrm{DM}}_{\mathrm{CGM}}$ and $\overline{\mathrm{DM}}_{\mathrm{ISM}}$ can produce high DM fluctuations, even at low redshift. Removal of these contaminated sightlines are required in order to make precise deductions about the state of the IGM using FRB DM statistics. This might be especially difficult to do for high redshift FRBs since FRBs observed at high redshift are more likely to interact with free electrons from the IGM and so large DM sightlines become more likely (see Figure 7.2). At higher redshifts, the distribution functions tend to become better approximated as Gaussian. Previous studies such as [165], use the variance, $\sigma^2 = \langle(\mathrm{DM} - \overline{\mathrm{DM}})^2\rangle$, of the DM distributions to estimate the maximum size of the ionized regions at each z. Since the maximum size of the ionized regions depends on the astrophysical parameters, our approach is complimentary. The astrophysics driving the EoR will determine the evolution of the $\mathrm{DM(z)}$ probability distributions. For example, scenarios with larger ζ or smaller $M_{\rm turn}$ tend to have DM distributions skewed to higher DM since reionization begins early, which increases the relative likelihood of finding high DM sightlines by increasing the likelihood of interaction with free electrons. Meanwhile, scenarios where the EoR unfolds as inside-out, tend to have high density regions in δ couple to regions of high fraction of ionized hydrogen, i.e. the product $\overline{x_{\rm HII}\delta} \sim n_e$ is larger than the corresponding outside-in scenario where the high density regions couple to low fraction of ionized hydrogen. In this scenario, the free electron regions tend to be denser in inside-out models than the corresponding outside-in models. As a result, scenarios where reionization unfolds with $\beta > 0$ increases the likelihood of high DM sightlines. This is reflected in the DM(z) distributions in Figure 7.3 where there is a larger portion of distribution in the high DM portion of the distribution compared to outside-in maps where the distribution is skewed to lower DMs.

These parameters influence the shape of the DM distribution as well as their evolution in redshift. Since $\overline{\mathrm{DM}}$ is derived from these DM distributions, then the underlying astrophysics and morphology of the EoR can be detected directly from $\overline{\mathrm{DM}}$. In the following Sections, we build our intuition on how the astrophysics and morphology of the EoR affect $\overline{\mathrm{DM}}$.

7.3.2 Astrophysical Signature on $\overline{\mathrm{DM}}$

Local fluctuations in n_e make it difficult to deduce the astrophysics from individual sightlines. Instead we average over all sightlines to remove these fluctuations. In doing so, we can predict the signature of the astrophysical parameters on $\overline{\mathrm{DM}}$ in Equation 7.8. Since the presence of neutral hydrogen in the IGM causes a flattening of the $\overline{\mathrm{DM}}$ curve at the onset of neutral hydrogen, then the astrophysical parameters, which determine the timing of

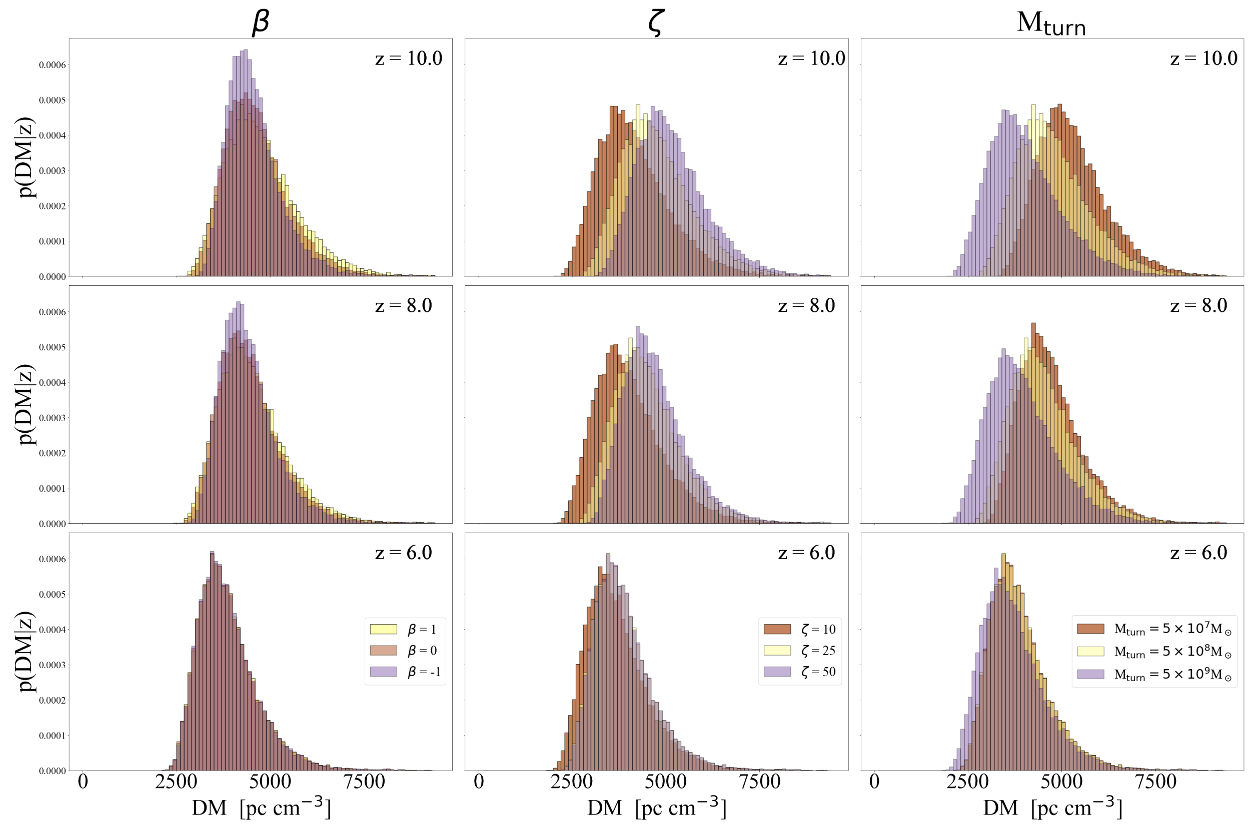

Figure 7.3: Evolution of the individual sightline DM probability distributions for a variety of reionization scenarios encapsulated by the density-ionization parameter β, ionizing efficiency ζ and mass scale of the ionizing sources $M_{\rm turn}$. Notice how the different reionization scenarios begin to distinguish themselves at higher redshifts. In each panel, the gold distribution corresponds to the fiducial reionization scenario of $\beta = 1$, $\zeta = 25$, $M_{\rm turn} = 5 \times 10^8 \mathrm{M}_\odot$ and $R_{\rm mfp} = 30\mathrm{Mpc}$.

this flattening, can be deduced from $\overline{\rm DM}$. For example, the ionizing efficiency ζ increases the output of UV photons from the ionizing sources, which for larger values of ζ, results in shifting the onset of reionization to higher redshifts. In this scenario, the IGM is ionized earlier and the flattening of the $\overline{\rm DM}$ curve occurs at larger z. Conversely, decreasing the ionizing efficiency of the sources shifts the flattening of the $\overline{\rm DM}$ curve to lower redshifts. Therefore, if we study the dependence of $\overline{\rm DM}$ on ζ at fixed z (within the EoR), increasing the ionizing efficiency will increase the mean DM of the FRBs at that redshift. We find a similar dependence for $\overline{\rm DM}$ on $M_{\rm turn}$. This is the mass scale for a source to begin efficiently producing UV photons which similarly alters the onset of reionization. Lower

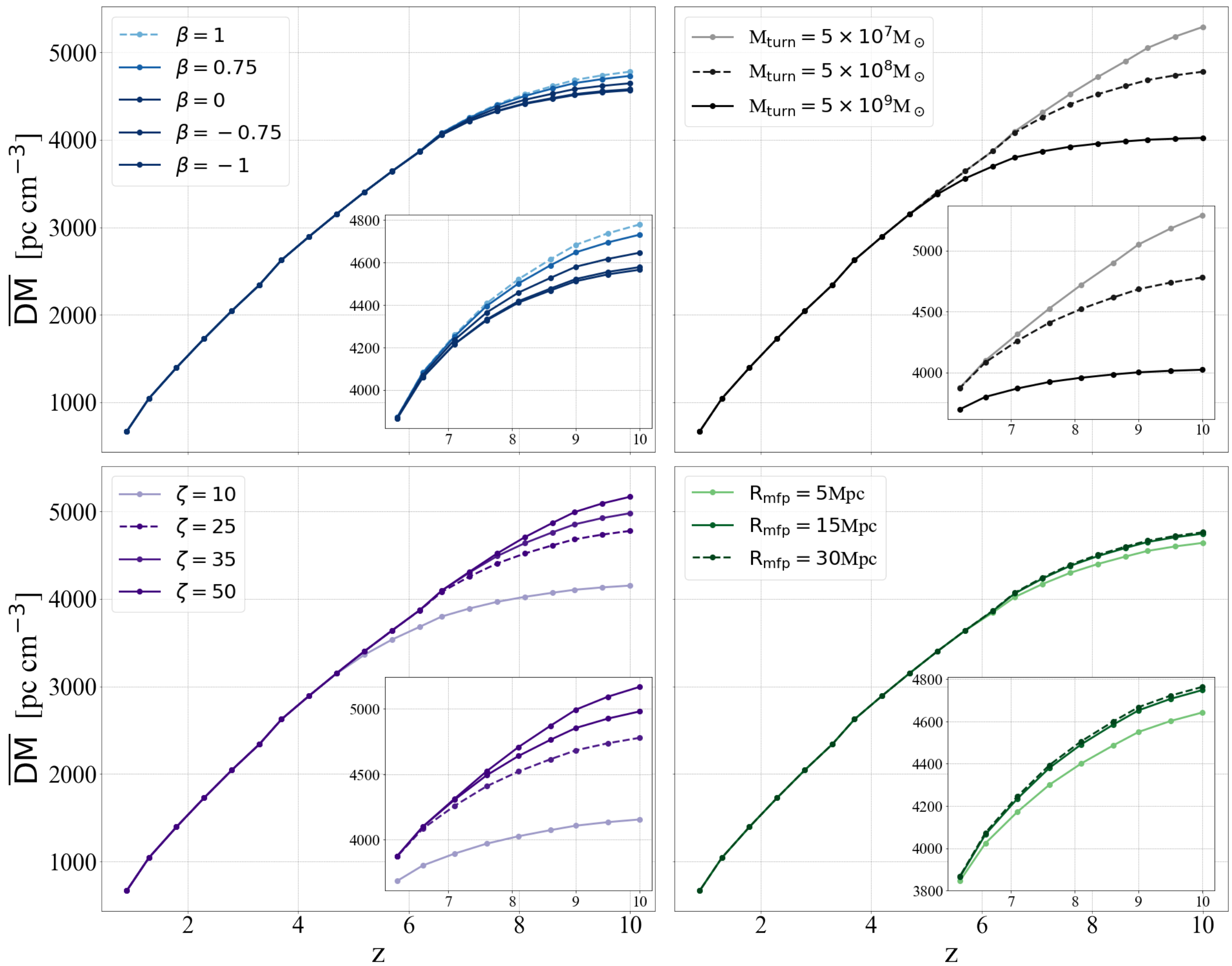

Figure 7.4: $\overline{\mathrm{DM}}$ for a variety of density-ionization correlations β (upper left), mass scale of the ionizing sources M_{turn} (upper right), ionizing efficiency ζ (lower left), and mean free path R_{mfp} of the ionizing photons. Notice how high ionizing efficiency of the sources and smaller masses of the ionizing sources lead to an early onset reionization, and so an increase in $\overline{\mathrm{DM}}$ at that redshift. Inside-out reionization models $\beta > 0$, lead to an increase in $\overline{\mathrm{DM}}$, since the free electron number density in ionized regions is greater than the corresponding ionized region in outside-in models $\beta < 0$. In each panel the dotted curve corresponds to same reionization scenario $\beta = 1$, $\zeta = 25$, $M_{\mathrm{turn}} = 5 \times 10^8 \mathrm{M}_\odot$ and $R_{\mathrm{mfp}} = 30\mathrm{Mpc}$. We use this fiducial reionization scenario in our forecasts in Section 7.4.

values of $M_{\rm turn}$ allow the EoR to start early, which shifts the flattening of $\overline{\rm DM}$ to higher redshifts, while larger values of $M_{\odot}$, delays reionization, pushing the flattening of $\overline{\rm DM}$ to lower redshifts. We find that $\overline{\rm DM}$ is less sensitive to $R_{\rm mfp}$ as compared to the other EoR parameters. Once $R_{\rm mfp}$ is increased beyond the size that is physically possible at given z, $\overline{\rm DM}$ loses all sensitivity to the parameter.

In general, these astrophysical parameters determine the mean ionization fraction $\overline{x}_{\rm HII}$ at each redshift z, which $\overline{\rm DM}$ depends on. One could approach the study of $\overline{\rm DM}$ on $\overline{x}_{\rm HII}$ by adopting a model for the evolution of $\overline{x}_{\rm HII}$ on z without invoking the dependence of astrophysical parameters. However, these parameters can also have a secondary affect on $\overline{\rm DM}$ through the cross term in Equation 7.8. For example, if the Universe reionizes with turnover masses $M_{\rm turn} \simeq 10^{10}{\rm M}_{\odot}$, then the size of the ionized regions are larger compared to a scenario with smaller turnover which increases the cross term in Equation 7.8. Physically this means that there are more free electrons for the FRBs to interact with. Increasing the maximum size of the ionized regions $R_{\rm mfp}$ will maximize the interaction between FRBs and free electrons for given EoR model with fixed ζ and $M_{\odot}$. This maximises $\overline{\rm DM}$.

The sensitivity of $\overline{\rm DM}$ to ζ, $M_{\rm turn}$ and $R_{\rm mfp}$ increases as we observe FRBs at higher redshifts. This is due to the FRBs having interacted with the ionization history of the universe for longer and so Equation 7.8 carries more information about the EoR. Conversely, $\overline{\rm DM}$ loses all sensitivity to the astrophysics of the EoR as the entire Universe is reionized, referring to Figures 7.4, all models converge at $z = 6$ which in our models correspond to an entirely ionized IGM.

7.3.3 Morphological Signature on $\overline{\rm DM}$

From Equation 7.8, the mean DM of high redshift FRBs is sensitive to the density-ionization product $\delta x_{\rm HII}$. The method in which $x_{\rm HII}$ couples to the underlying density field δ, will have consequences for the $\overline{\rm DM}$. Inside-out scenarios, i.e. scenarios where $\beta > 0$ (positive correlation between δ and $x_{\rm HII}$), high density regions couple to high ionized fractions in $x_{\rm HII}$. This results in the ionized regions being denser in free electrons, leading to an increase in $\overline{\rm DM}$ compared to other morphologies. For example, the outside-in scenario, where δ and $x_{\rm HII}$ are negatively correlated ($\beta < 0$), the underdense regions in δ correspond to high fractions of ionized hydrogen. As a result, the free electron density within the ionized regions are comparatively smaller. Referring to Figure 7.4, we see that inside-out morphologies lead to an increase in the mean DM of high redshift FRBs as compared to outside-in models. Intermediate values of β can be interpreted as follows; as β is increased from the uncorrelated scenario, $\beta = 0$, (where the ionized regions are random with respect to δ) to $\beta = 1$, the high density regions in δ becoming increasingly likely to couple to ionized regions in $x_{\rm HII}$. The mean n_e within bubbles monotonically increases until $\beta = 1$ where all high density regions correspond to ionized bubbles and $\overline{\rm DM}$ is maximized with respect to β. Conversely, as we decrease β from $\beta = 0$ to $\beta = -1$, the high density regions increasingly couple to regions of low ionized fraction in $x_{\rm HII}$ which monotonically decreases the mean n_e of the ionized regions. As a result, the product $n_e \sim \delta x_{\rm HII}$ is decreased, which leads to a decrease in the mean DM of these models. As a result, inside-out scenarios receive a boost in average DM due to the increase of $\overline{n}_e$ compared to outside-in driven models. The morphological signature on $\overline{\rm DM}$ is different than the astrophysical parameters since the morphology directly influences the mean density of free electrons, n_e within the ionized bubbles without changing the timing of reionization. The contrast in $\overline{\rm DM}$ between the extreme morphologies is greatest for FRBs observed at highest redshift. The longer the exposure of the FRB to the ionization history, the more sensitive $\overline{\rm DM}$ will be to the morphology. Conversely, as we observe FRBs at lower redshifts, there hasn't been enough exposure to the EoR morphology to distinguish between different β models. Therefore $\overline{\rm DM}$ loses all sensitivity to β as $\overline{x}_{\rm HII} \to 1$. In Section 7.5, we determine the number of FRBs required to make a measurement of $\overline{\rm DM}$ precise enough to place constraints on β as well as the astrophysical parameters.

In the following Section, we generate mock data by sampling the fiducial DM distributions at each redshift given our choice of fiducial EoR and morphological parameters. In Section 7.4.3, we forecast the type of constraints that can be placed on β as well as the remaining EoR parameters through measurement of $\overline{\rm DM}$.

7.4 Forecasts

In this Section we use the formalism of Section 7.3 to forecast the constraints that can be placed on the EoR through measurement of high redshift FRB DMs. Since high redshift FRBs have not yet been detected, we simulate a mock observation of high DM FRBs under a fiducial reionization scenario. It should be noted that it is assumed that all generated FRBs are observed with accompanied redshift localization where we take the uncertainty on the redshift, $\sigma_z = 0$. This may seem an ambitious assumption, but [159] notes that with a mid- to large-size optical survey, it should be feasible to obtain about 10 redshifts for host galaxies per night. Still, we concede that this redshift assumption is rather unrealistic. Acquiring redshift information entails localizing the burst to a host galaxy. Currently, there are a few localization techniques. Firstly, repeating FRBs can be localized by other high resolution interferometers such as the Very Large Array (VLA) by doing a follow up search. Conversely, it is very difficult to localize a non-repeater because one would need an instrument with a very large field of view as well as a high resolution. ASKAP is currently able to do such localization and has localized all of the localized non-repeaters to date. Once CHIME outriggers are placed, increasing CHIME's spatial resolution, CHIME too will be able to perform such localization. That being said, some of the instrument software may inhibit our ability to do this localization, even with outriggers, with high redshift bursts. Another localization technique is to look for high energy counterparts. The Neil Gehrels Swift Observatory, for example, has the ability to aid in localisation if there is a high energy counterpart to the burst. This, however, represents a small subset of FRBs and so far all bursts with counterparts have been in the Milky Way. Certainly, all of these methods may not be optimal for searching for high redshift FRBs. The work in this chapter simply explores what can be done in the most ideal scenario where both DM and redshift information is available. In upcoming work, we intend to explore whether constraints may be placed on reionization history when one only has access to DM. In this Section, we outline our model for generating this mock observation as well as discuss our fiducial reionization scenario. In Section 7.5, we present the results of these forecasts.

7.4.1 Intrinsic FRB Statistics

Since FRBs observed after the EoR do not contain any information about the ionization history of the Universe, only high redshift FRBs observed during the EoR contribute to our forecasts. FRBs at these redshifts have not yet been observed and may be rare. To get a more realistic sense of how many intrinsic FRBs that can potentially be observed given a capable high DM experiment, we use an existing theoretical model of source count distributions of FRBs at each DM. From this theoretically motivated count of FRBs within $z > z_{\rm EoR}$, we can populate our mock catalogue. We first define an intrinsic source count distribution of FRBs. It will be from this distribution that we populate the redshift bins of our fiducial sample for our forecasts. For this, we choose a source count distribution that traces the star formation rate (SFR) [27]. While other source count distributions have been proposed, [112] shows that the the density of FRBs ($\rho_{\rm FRB}$) closely resembles cosmic star formation history. We follow this prescription and use the following simple top-heavy distribution for the number of FRBs per DM,

$$\frac{dn}{d\mathrm{DM}} = \frac{\rho_{\rm FRB}(z)}{(1+z)} \frac{dV}{dz} \frac{dz}{d\mathrm{DM}} \tag{7.9}$$

where, $\frac{dV}{dz}$ is the comoving volume element.

Tracing the cosmic star formation history, we take the density to be proportional to the SFR density [92, 94],

$$\rho_{\rm FRB}(z) \propto \rho_{\rm SFR}(z) = 0.015 \frac{(1+z)^{2.7}}{1 + ((1+z)/2.9)^{5.6}} \text{ M}_\odot \text{ yr}^{-1} \text{ Mpc}^{-3} \tag{7.10}$$

What relies on the model in this source count distribution is the $\frac{dz}{d\mathrm{DM}}$ factor. As mentioned in Sections 7.3.2 and 7.3.3, the DM–z relation is sensitive to reionization parameters. Currently, the widely used DM–z relation is linear

$$\mathrm{DM(z)} = \mathrm{C} \times \mathrm{z} \text{ pc cm}^3 \tag{7.11}$$

where C is often taken to be 1000 [112] or 1200 [61]. These linear relations approximate the redshift to an accuracy of about 2% for $z < 2$ [121]. As shown in Figure 7.4, the model of reionization affects the shape of the DM–z relation, especially at high redshift. In order to place constraints on reionization, high redshift samples are paramount. Therefore, in order to compute the source count distribution for the fiducial model, we calculate $\frac{dz}{d\mathrm{DM}}$ by taking numerical derivatives of the corresponding fiducial DM–z curve. Measurements of the EoR parameters have not yet been made, so in order to produce a mock sample of observed high redshift FRBs, we must assume a fiducial reionization scenario. Our fiducial EoR model is produced by fixing the astrophysical and morphological parameter β from Section 7.3. We choose EoR parameters $\zeta_0 = 25$, $\mathrm{M}_{\mathrm{turn},0} = 5 \times 10^8 \mathrm{M}_{\odot}$, and $\mathrm{R}_{\mathrm{mfp},0} =$ 30Mpc as well as $\beta = 1$. The astrophysical parameters are consistent with previous studies such as [100], while the morphological parameter, $\beta = 1$, corresponds to an inside-out reionization scenario.

The fiducial DM–z curve is the light blue dashed line ($\beta = 1$) shown in the top left panel of Figure 7.4. Now that the CDF is defined, we can build our mock data set.

7.4.2 Mock Catalogue of FRBs

We build our sample of FRBs using inverse transform sampling whereby a given number of random samples is drawn from a probability distribution given its CDF. This populates each redshift bin, of bin width δ_z = 1, with FRBs according to the CDF. The method is the following, where our random variable X is the FRB source count:

1. Define a random variable, X, whose distribution is described by the CDF, F_X.

2. Generate a random number u from a uniform distribution in the interval $[0, 1]$. This number will be interpreted as a probability.

3. Compute the inverse of of the CDF, that is $F_X^{-1}(u)$.

4. Compute $X = F_X^{-1}(u)$. Now the random variable X with distribution F_X has been generated.

Using this method, we in fact draw a distribution of DM counts per DM bin. Then, using our fiducial DM-z relation, convert this to counts per redshift bin. We simply proceed to use the probability distribution in 7.2 to draw the given number of DMs per redshift bin. This method guarantees that our sample has line of sight fluctuations, ensuring that every FRB has a unique DM, even when in the same redshift bin.

It may be noted that we only account for fluctuations in the DM distribution of FRBs. The spacial distribution of FRBs is not accounted for here, that is, the sources are taken to have random positions. In actuality, the spacial distribution of FRBs will be positively correlated with the underlying matter distribution and so one my posit that FRBs emitted inside an ionized region would acquire considerable DM from the host bubble. We find that the contribution of the host bubble, or lack there of, to the total DM from the line of sight during reionization is negligible and we proceed without populating halos with sources. At this point, we are ready to move on to performing the MCMC on the sample.

7.4.3 MCMC setup

We place the mean of the individual sightline DMs of our mock FRB catalogue into a vector $\overline{\mathrm{DM}}_{\mathbf{S}}$ corresponding to the mean of the sample FRBs for each redshift z. For such a measurement, the uncertainties on $\overline{\mathrm{DM}}_{\mathbf{S}}$ are the sum of the instrumental systematic errors in measuring the individual sightline DMs and the uncertainties in $\overline{\mathrm{DM}}_{S}$ due to sample variance. The instrument errors on the individual DM are assumed to be small and so we do not model the instrumental errors and only include the errors due to sample variance. The uncertainties due to sample variances on $\overline{\mathrm{DM}}_{S}$ are

$$\sigma_s = \frac{s_{N-1}}{\sqrt{N}} \tag{7.12}$$

where N are the number of FRBs comprising the sample and s_{N-1} is the measured sample variance given by

$$s_{N-1}^2 = \frac{1}{N-1}\sum_{i=0}^{N}(\mathrm{DM_i} - \overline{\mathrm{DM}}_{\mathrm{S}})^2 \tag{7.13}$$

where $\mathrm{DM_i}$ are the individual sightline DMs sampled from the probability density functions generated by our fiducial model, and $\overline{\mathrm{DM}}$ is the mean of such a sample. Our forecasts consider different cases of σ_S by considering different total number N of FRBs observed. To place constraints on the on the EoR parameters $\boldsymbol{\theta} = \beta, \zeta, M_{\rm turn}, R_{\rm mfp}$, we evaluate the probability of θ given measurement of the mean DM from the samples from our fiducial EoR model defined in Section 7.4.2. This is the posterior $p(\boldsymbol{\theta}|\overline{\rm DM}_S)$. We can evaluate the posterior $p(\boldsymbol{\theta}|\overline{DM}_{\rm S})$ through Bayes theorem:

$$p(\boldsymbol{\theta}|\overline{\rm DM}_S) \propto p(\overline{\rm DM}_S|\boldsymbol{\theta})p(\boldsymbol{\theta}), \tag{7.14}$$

where $p(\overline{\rm DM}_S|\boldsymbol{\theta})$ is the likelihood function and $p(\boldsymbol{\theta})$ is the prior on the EoR parameters $\boldsymbol{\theta}$. Since the likelihood function is non-analytic in the EoR parameters $\boldsymbol{\theta}$, we use `21cmFAST` to generate a model density and ionization field representative of the IGM with parameters β, ζ, $M_{\rm turn}$, $R_{\rm mfp}$. To generate the density and ionization field with the morphology indicative of the model β, we use the same procedure described in [116]. From this model reionization and density field, we generate a lightcone for each line of sight, and evaluate $\rm DM$ for each of these lines of sight. We then average all sightlines together to evaluate $\overline{\rm DM}$ for this reionization model. The mean DM of all sightlines for this model is compared to the fiducial mean DM of the mock FRBs through the χ^2 statistic. The likelihood $p(\boldsymbol{\theta}|\overline{DM}_{\rm S})$ is then computed as:

$$p(\overline{\rm DM}_{\mathbf{S}}|\boldsymbol{\theta}) \propto \exp\left[-\frac{1}{2}\sum_z \frac{\left(\overline{\rm DM}_{\rm model} - \overline{\rm DM}_{\mathbf{S}}\right)^2}{\sigma_S^2}\right], \tag{7.15}$$

where we have assumed the errors on $\overline{\rm DM}_{\mathbf{S}}$ to be Gaussian and independent. The Gaussianity of the likelihood is a valid assumption since for larger samples of $\rm DM$, the mean $\overline{\rm DM}$, of these samples tend to be Gaussian distributed according to the central limit theorem. However since there are indeed correlations between redshift bins, the independence of the likelihood in terms of z serves as an approximation. We consider the mean DM of FRBs measured from redshifts $z = 8$ to $z = 10$ in steps of $\Delta z = 1$ corresponding to the redshifts that contain the largest sensitivity to the EoR parameters. Inclusion of more redshifts do not significantly alter our conclusions and so for computational simplicity we exclude them from our forecasts. We place uniform priors on each of the EoR parameters $\boldsymbol{\theta}$ within $p(\boldsymbol{\theta})$. Since β is only defined from $-1 \leq \beta \leq 1$, we place the prior $-1 \leq \beta \leq 1$ which covers the entire possible physical range of EoR morphologies. For $R_{\rm mfp}$ we use

$5\,\mathrm{Mpc} < R_{\mathrm{mfp}} < 160\,\mathrm{Mpc}$ which spans the all possible sizes consistent with the length of our simulation boxes. For ζ, we place the range $5 < \zeta < 100$ which encapsulates the entire physically allowed duration of reionization histories [100]. Finally for M_{turn}, we use values of $10^7 M_\odot < M_{\mathrm{turn}} < 10^{10} M_\odot$, which are physically motivated by the atomic cooling threshold and by constraints on the faint end of UV luminosity functions [117]. Using the sampling discussed in Section 7.4.1, we generate mock data and fit to them via the likelihood

$$p(\overline{\mathrm{DM}}_{\mathbf{S_z}}|\boldsymbol{\theta}) \propto \exp\left[-\frac{1}{2}\sum_z \frac{\left(\overline{\mathrm{DM}}_{\mathrm{model}} - \overline{\mathrm{DM}}_{\mathbf{S_z}}\right)^2}{\sigma^2_{S_z}}\right]. \tag{7.16}$$

where here we are summing over redshift bins, $z = \{8, 9, 10\}$. To sample our posterior distribution, we use a Markov Chain Monte Carlo (MCMC) approach, as implemented by the affine invariant MCMC package `emcee` [49].

7.5 Results

Here we present the MCMC results of our forecast discussed in Section 7.4.3 corresponding to measurement of N high redshift FRBs observed between $z = 8$ to $z = 10$, and distributed in z according to the CDF described in Section 7.4.1. We repeat this mock observation for three different total number of measured FRBs. We use $N = 10^2, 10^4, 10^5$, where these observed FRB counts span a reasonable range of sample variances. In each case we assume that the $\overline{\mathrm{DM}}$ of these FRBs is dominated by the contribution of the IGM. As discussed in Section 7.2.3, we neglect the contributions due to the CGM and ISM and leave their inclusion for future work. The fiducial reionization scenario has parameters $\beta = 1$, $\zeta = 25$, $\mathrm{M}_{\mathrm{turn}} = 5\times10^8\mathrm{M}_\odot$ and $R_{\mathrm{mfp}} = 30\mathrm{Mpc}$.

7.5.1 Larger Sample Sizes

In this scenario we detect N FRBs, distributed across the redshift bins $z = 8 - 10$ according to the theoretically motivated source count distribution discussed in Section 7.4.1. Figure 7.5 and 7.6 show the results of this forecast for cases corresponding to $N = 10^4$ and

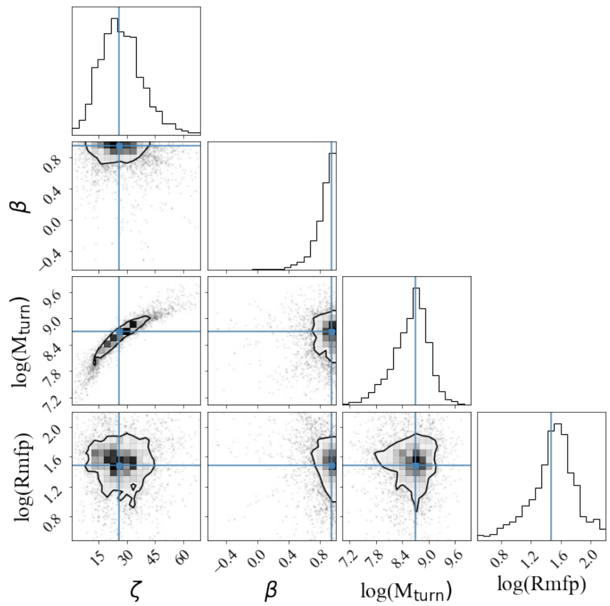

Figure 7.5: Posterior distributions for measurement of $\overline{\mathrm{DM}}$ for 10^4 FRBs distributed between redshifts $8 \leq z \leq 10$ according to the source count distribution in Section 7.4.1. The 68% credibility regions are shown. Such a measurement can rule out uncorrelated $\beta = 0$ and outside-in reionization $\beta < 0$ at 68%CR.

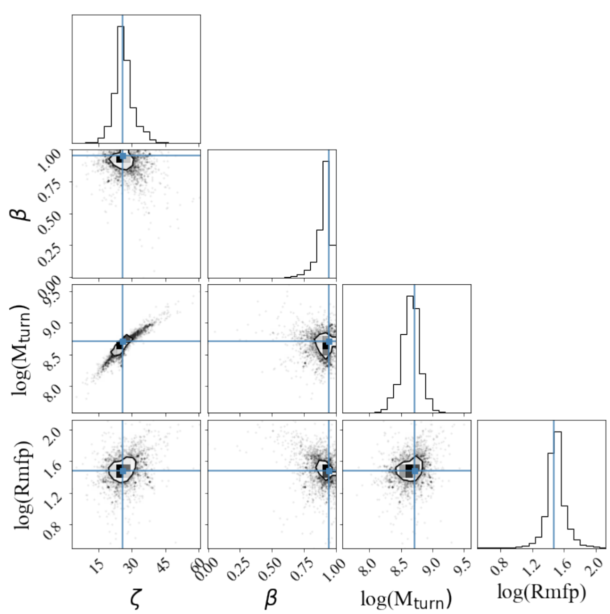

Figure 7.6: Posterior distributions for measurement of $\overline{\mathrm{DM}}$ for 10^5 FRBs distributed between redshifts $8 \leq z \leq 10$ according to the source count distribution in Section 7.4.1. Using such a measurement, we can rule out uncorrelated and outside-in reionization scenarios at 68%CR.

$N = 10^5$ respectively. From the posterior of both Figures, we see that there are clear degeneracies between ζ and $M_{\rm turn}$. This is due to both parameters establishing the redshift in which the flattening of $\overline{\rm DM}$ occurs. This degeneracy is pronounced in Figure 7.3 where changing the values of ζ and $M_{\rm turn}$ result in translating the distribution along the horizontal axis. By examining the 68% credibility regions (CR) in Figure 7.5, we can see that measurement of $N = 10^4$ FRBs within these redshift bins can constrain ζ to $\zeta = 25.5^{+11.5}_{-10.5}$ and $\log(\rm M_{turn}) = 8.65^{+0.29}_{-0.49}$. By placing constraints on these parameters (the ionizing efficiency and the halo mass scale of the UV sources), one can place constraints on the timing and duration of reionization. We find that with $N = 10^4$ FRBs in these redshift ranges, we can constrain the duration, Δz, of reionization (duration between $0.25 \leq \overline{\rm x}_{\rm HII} \leq 0.75$) to $\Delta z = 2.1^{+0.50}_{-0.30}$, and the midpoint $z_{\rm mid} = 7.8^{+0.20}_{-0.20}$, at 68% credibility. Referring to the posterior in Figure 7.6, the constraints on ζ and $M_{\rm turn}$ are tighter for the extreme case of $N = 10^5$ FRBs where we can constrain ζ to within $\zeta = 25^{+7}_{-9}$ at 95%CR and $\log(\rm M_{turn}) = 8.76^{+0.14}_{-0.46}$ at 95%CR. With constraints on these parameters we can place constraints on the duration of reionization, $\Delta z = 2.0^{+0.5}_{-0.4}$, at %95CR and the midpoint of reionization, $z = 7.8^{+0.4}_{-0.2}$ at 95%CR.

The correlation parameter β does not share degeneracies with these parameters since it does not affect the timing of reionization, rather it affects the mean density, $\overline{n}_e$, of free electrons in the ionized region. We find from the posterior that measurement of 10^4 FRBs can distinguish between the sign of β. Since the sign of β corresponds to the type of correlation between δ and $x_{\rm HII}$, we find that measurement of $\overline{\rm DM}$ using 10^4 FRBs can rule out $\beta < 0$ (outside-in) scenarios and $\beta = 0$ (uncorrelated scenarios) at 95% CR. In the more extreme case of $N = 10^5$ FRBs, we can further rule out uncorrelated and outside-in scenarios at 99% CR. Measurement of 10^4 FRBs between $8 < z < 10$ is sufficient to constrain the order of magnitude of $R_{\rm mfp}$ at 68%CR. For the case of $N = 10^5$ FRBs, our models can constrain the order of magnitude of $R_{\rm mfp}$ at 95%CR.

7.5.2 Smaller Sample Sizes

In this scenario we measure 100 FRBs distributed across redshift bins between $8 \leq z \leq 10$, again using the source count distribution outlined in section 7.4.1. We show the posterior of such a measurement in Figure 7.7. Our interpretation of the degeneracy between the parameters is identical to 7.5.1. We see from the posterior of Figure 7.7 that smaller samples of FRBs lead to biased fits due to cosmic variance. However even with such small sample sizes, 68% of the contours lie within $\beta > 0$ suggesting that we can still rule out both uncorrelated and outside-in reionization scenarios at 68%CR. We see from the posterior that we can rule out models with ζ and $\mathrm{M}_{\mathrm{turn}}$ outside the range $23 \leq \zeta \leq 55$ and $4 \times 10^9 \mathrm{M}_{\odot} \leq M_{\mathrm{turn}} \leq 3 \times 10^9 \mathrm{M}_{\odot}$ at 68%CR. Ruling out this region of parameter space is tantamount to setting broad constraints on the timeline of reionization. For example, this region excludes scenarios where the Universe is still neutral at redshift $z = 10$, which would severely flatten $\overline{\mathrm{DM}}(z)$ between $8 \leq z \leq 10$. We can rule these models out at 68%CR. Similarly this region excludes models where the Universe is more than 60% ionized by redshift $z = 8$, which would reduce the flattening of $\overline{\mathrm{DM}}$ between $8 \leq z \leq 10$. We can rule out these scenarios at 68%CR.

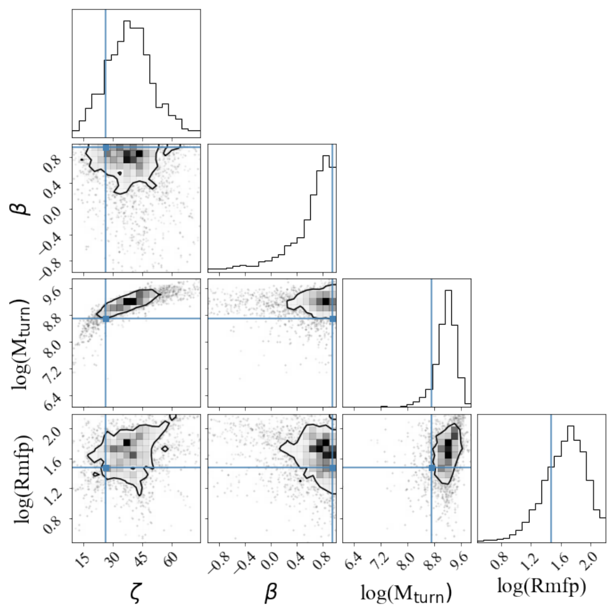

Figure 7.7: Posterior distributions for measurement of $\overline{\mathrm{DM}}$ for 100 FRBs distributed between $8 \leq z \leq 10$ according to the source count distribution in Section 7.4.1. The 68% credibility regions of our measurements are shown. This measurement can rule out extreme EoR models, for example, scenarios where the Universe is ionized by $z = 8$.

Chapter 8

Conclusion

In this thesis, we explored how direct probes of the IGM can help us learn about the epoch of reionization and address the challenges raised in Chapters 1, 2, and 3. In Chapter 6 we presented an end-to-end simulation and analysis pipeline to cross-correlate 21 cm and [CII] line intensity maps. This is done in the hopes of extracting a correlated signal from data dominated by systematics. We create a mock cosmology with a peaked spectrum at $k = 0.075$. We also include realistic foreground contaminants and produce mock observations by simulating the instrumental effects of the HERA array and the CCAT-prime telescope. We expect to find a negative peak at $k = 0.075$ since the fields are anti-correlated at this mode. We study three scenarios: one where only instrumental noise is added to the cosmological signal, one where the cosmological signal is observed over one night and has both foregrounds and noise added to it, and one where the second scenario is averaged over 100 signal realisations. In studying both the auto- and the cross-spectra of these fields, we find that the negative peak is recovered in the cross-spectrum of these fields while the 21 cm auto-spectrum is heavily biased by foregrounds and instrumental noise. In performing a basic null test, we find that this negative peak is indeed due to the anti-correlation between the cosmological fields and not due to anti-correlated foregrounds. These results are promising and serve as an initial proof of concept for this technique.

Still, this effort can be improved upon. To begin, the input cosmological fields can be made more realistic by generating density fields and producing correlated line intensity maps from them using analytic and semi-empirical relations between the density field and the intensity of the line being simulated. In addition, it is of paramount importance to extend this pipeline to produce and analyse 3-dimensional data cubes in order to have access to line-of-sight modes. Moreover, it is clear from the results of the null test that improved foreground modelling would be advantageous. In particular, one can make use of clustering information to create a more realistic spatial distribution of [CII] line interlopers. There were also certain contaminants that were omitted completely, such as radio frequency interference (RFI) and extended sources, which can be included in updated versions of this pipeline. And of course, a long term goal for this research program is to extend this framework to involve other probes, such as CMB observations and near-infrared observations, which can also be cross-correlated with the 21 cm line.

In Chapter 7 we study how the astrophysics and morphology of the EoR affects the mean DM of high redshift FRBs. We use a parametrization, β, that tracks the density-ionization correlation in the EoR and common astrophysical parameters to bracket the range of physical EoR scenarios. We find that $\overline{\mathrm{DM}}$ is sensitive to the astrophysics and morphology of reionization and can influence fluctuations in $\overline{\mathrm{DM}}$ up to $1000\mathrm{pc\ cm}^{-2}$. In particular, the ionizing efficiency and mass scale of the ionizing sources cause the greatest fluctuations in $\overline{\mathrm{DM}}$, which we physically attribute to being caused by the modified timing of reionization. The EoR morphology impacts $\overline{\mathrm{DM}}$ by changing the density of free electrons within the ionized regions. We find that inside-out reionization scenarios produce the greatest density of free electrons within the ionized bubbles which increases the mean DM of high redshift FRBs with respect to outside-in reionization scenarios. To gauge the viability of such a probe, we perform numerical forecasts to study the types of constraints that can be placed on the astrophysical and correlation parameters using measurements of highly dispersed FRBs. Using a fiducial inside-out reionization scenario with midpoint of reionziation, $z = 2.0$ and duration $\Delta z = 7.8$, we find that samples of 100 FRBs can rule out uncorrelated reionization at 68%CR. Using samples of 10^4 FRBs in the same redshift range can rule out uncorrelated and outside-in reionization at 95%CR. We also find that samples of 100 FRBs between $8 \leq z \leq 10$ can rule out scenarios where the Universe is entirely neutral at $z = 10$ with 68%CR. Further, this measurement can also rule out EoR scenarios where the IGM is more than 60% ionized at $z = 8$. Larger sample sizes ($\geq 10^4$), of high redshift FRBs, distributed in redshift from $8 \leq z \leq 10$ according to the theoretically motivated source count distributions, can constrain the duration of reionization (duration between mean ionized fractions 0.25 to 0.75) to $\Delta z = 2.1^{+0.50}_{-0.30}$ and midpoint $z = 7.8^{+0.20}_{-0.20}$ at 68%CR. Finally, we find that samples of $\geq 10^5$ high redshift FRBs can constrain the duration of reionization (duration between mean ionized fractions 0.25 to 0.75) to $\Delta z = 2.0^{+0.5}_{-0.4}$ and midpoint $z = 7.8^{+0.4}_{-0.2}$ at 95%CR.

For future work, we would like to further this proof of concept by using the full distribution of DMs at each z in our forecasts, and by making use of observational constraints as well as the intrinsic constraints outlined in this paper. There are, most obviously, observational constraints that play a role in the feasibility of such parameter fitting with real data. While high-DM (DM $\geq$ 4000) events have not yet been observed, [27] notes that one can design an experiment that has a higher detection rate of highly dispersed events by trading time resolution for higher frequency resolution. [166] note that FAST and SKA will have the capability of making such detections and most recently [56] show that observations from SKA phase 2 will indeed reveal our reionization history. It must be noted, however, that the FRB progenitor will ultimately dictate whether there exists an FRB population during the EoR. In addition, a more sophisticated simulation would allow one to explore correlations between $\mathrm{M}_{\mathrm{turn}}$, ζ, and the FRB source count distribution since these three parameters ultimately depend on the stellar population. Folding everything into one framework would allow one to study such correlations as well as take clustering of FRBs into account.

Cosmic dawn did not occur as a single bright event, but rather individual stars, one by one, lit our dark universe. Similarly, we will likely not understand cosmic dawn and the epoch of reionization from one observation alone, but rather we will need to make use of many tools which, one by one, will illuminate our understanding of this mysterious time in our universe's history. In this thesis, we explored three such probes: the 21 cm line, the [CII] line, and the DMs of highly dispersed FRBs. These observations can all serve as tools which will, along with others, help us understand the epoch of reionization.

Bibliography

[1] Abbott, B., Abbott, R., Abbott, T., Abernathy, M., Acernese, F., Ackley, K., Adams, C., Adams, T., Addesso, P., Adhikari, R., and et al. Observation of gravitational waves from a binary black hole merger. *Physical Review Letters 116*, 6 (Feb 2016).

[2] Aravena, M., Austermann, J., Basu, K., Battaglia, N., Beringue, B., Bertoldi, F., Bond, J. R., Breysse, P., Bustos, R., Chapman, S., Choi, S., Chung, D., Cothard, N., Dober, B., Duell, C., Duff, S., Dunner, R., Erler, J., Fich, M., Fissel, L., Foreman, S., Gallardo, P., Gao, J., Giovanelli, R., Graf, U., Haynes, M., Herter, T., Hilton, G., Hlozek, R., Hubmayr, J., Johnstone, D., Keating, L., Komatsu, E., Magnelli, B., Mauskopf, P., McMahon, J., Meerburg, P. D., Meyers, J., Murray, N., Niemack, M., Nikola, T., Nolta, M., Parshley, S., Puddu, R., Riechers, D., Rosolowsky, E., Simon, S., Stacey, G., Stevens, J., Stutzki, J., Engelen, A. V., Vavagiakis, E., Viero, M., Vissers, M., Walker, S., and Zou, B. The ccat-prime submillimeter observatory, 2019.

[3] Bandura, K., Addison, G. E., Amiri, M., Bond, J. R., Campbell-Wilson, D., Connor, L., Cliche, J.-F., Davis, G., Deng, M., Denman, N., Dobbs, M., Fandino, M., Gibbs, K., Gilbert, A., Halpern, M., Hanna, D., Hincks, A. D., Hinshaw, G., Höfer, C., Klages, P., Landecker, T. L., Masui, K., Mena Parra, J., Newburgh, L. B., Pen, U.-l., Peterson, J. B., Recnik, A., Shaw, J. R., Sigurdson, K., Sitwell, M., Smecher, G., Smegal, R., Vanderlinde, K., and Wiebe, D. Canadian Hydrogen Intensity Mapping Experiment

(CHIME) pathfinder. In *Ground-based and Airborne Telescopes V* (July 2014), L. M. Stepp, R. Gilmozzi, and H. J. Hall, Eds., vol. 9145 of *Society of Photo-Optical Instrumentation Engineers (SPIE) Conference Series*, p. 914522.

[4] BARKANA, R. Possible interaction between baryons and dark-matter particles revealed by the first stars. *Nature 555*, 7694 (Mar 2018), 71–74.

[5] BASU, K., HERNÁNDEZ-MONTEAGUDO, C., AND SUNYAEV, R. A. CMB observations and the production of chemical elements at the end of the dark ages. *416* (Mar. 2004), 447–466.

[6] BENIAMINI, P., KUMAR, P., MA, X., AND QUATAERT, E. Exploring the epoch of hydrogen reionization using frbs. *Monthly Notices of the Royal Astronomical Society* (Feb 2021).

[7] BHATTACHARYA, M., KUMAR, P., AND LINDER, E. V. Fast radio burst dispersion measure distribution as a probe of helium reionization, 2020.

[8] BOWMAN, J. D., CAIRNS, I., KAPLAN, D. L., MURPHY, T., OBEROI, D., STAVELEY-SMITH, L., ARCUS, W., BARNES, D. G., BERNARDI, G., BRIGGS, F. H., BROWN, S., BUNTON, J. D., BURGASSER, A. J., CAPPALLO, R. J., CHATTERJEE, S., COREY, B. E., COSTER, A., DESHPANDE, A., DESOUZA, L., EMRICH, D., ERICKSON, P., GOEKE, R. F., GAENSLER, B. M., GREENHILL, L. J., HARVEY-SMITH, L., HAZELTON, B. J., HERNE, D., HEWITT, J. N., JOHNSTON-HOLLITT, M., KASPER, J. C., KINCAID, B. B., KOENIG, R., KRATZENBERG, E., LONSDALE, C. J., LYNCH, M. J., MATTHEWS, L. D., MCWHIRTER, S. R., MITCHELL, D. A., MORALES, M. F., MORGAN, E. H., ORD, S. M., PATHIKULANGARA, J., PRABU, T., REMILLARD, R. A., ROBISHAW, T., ROGERS, A. E. E., ROSHI, A. A., SALAH, J. E., SAULT, R. J., SHANKAR, N. U., SRIVANI, K. S., STEVENS, J. B., SUBRAHMANYAN, R., TINGAY, S. J., WAYTH, R. B., WATERSON, M., WEBSTER, R. L., WHITNEY, A. R., WILLIAMS, A. J., WILLIAMS, C. L., AND WYITHE, J. S. B. Science with the Murchison Widefield Array. *30* (Apr. 2013), e031.

[9] BOWMAN, J. D., ROGERS, A. E. E., AND HEWITT, J. N. Toward Empirical Constraints on the Global Redshifted 21 cm Brightness Temperature During the Epoch of Reionization. *676*, 1 (Mar. 2008), 1–9.

[10] BOWMAN, J. D., ROGERS, A. E. E., MONSALVE, R. A., MOZDZEN, T. J., AND MAHESH, N. Reply to Hills et al. *564*, 7736 (Dec. 2018), E35–E35.

[11] BRADLEY, R. F., TAUSCHER, K., RAPETTI, D., AND BURNS, J. O. A ground plane artifact that induces an absorption profile in averaged spectra from global 21 cm measurements, with possible application to edges. *The Astrophysical Journal 874*, 2 (Apr 2019), 153.

[12] BREYSSE, P. C., AND ALEXANDROFF, R. M. Observing agn feedback with co intensity mapping. *arXiv* (2019).

[13] BULL, P., FERREIRA, P. G., PATEL, P., AND SANTOS, M. G. Late-time cosmology with 21 cm intensity mapping experiments. *The Astrophysical Journal 803*, 1 (Apr 2015), 21.

[14] BUNDY, K., BERSHADY, M. A., LAW, D. R., YAN, R., DRORY, N., MACDONALD, N., WAKE, D. A., CHERINKA, B., SÁNCHEZ-GALLEGO, J. R., WEIJMANS, A.-M., THOMAS, D., TREMONTI, C., MASTERS, K., COCCATO, L., DIAMOND-STANIC, A. M., ARAGÓN-SALAMANCA, A., AVILA-REESE, V., BADENES, C., FALCÓN-BARROSO, J., BELFIORE, F., BIZYAEV, D., BLANC, G. A., BLAND-HAWTHORN, J., BLANTON, M. R., BROWNSTEIN, J. R., BYLER, N., CAPPELLARI, M., CONROY, C., DUTTON, A. A., EMSELLEM, E., ETHERINGTON, J., FRINCHABOY, P. M., FU, H., GUNN, J. E., HARDING, P., JOHNSTON, E. J., KAUFFMANN, G., KINEMUCHI, K., KLAENE, M. A., KNAPEN, J. H., LEAUTHAUD, A., LI, C., LIN, L., MAIOLINO, R., MALANUSHENKO, V., MALANUSHENKO, E., MAO, S., MARASTON, C., MCDERMID, R. M., MERRIFIELD, M. R., NICHOL, R. C., ORAVETZ, D., PAN, K., PAREJKO, J. K., SANCHEZ, S. F., SCHLEGEL, D., SIMMONS, A., STEELE, O., STEINMETZ, M., THANJAVUR, K., THOMPSON, B. A., TINKER, J. L., VAN DEN BOSCH, R. C. E., WESTFALL, K. B., WILKINSON, D., WRIGHT, S., XIAO, T., AND ZHANG,

K. Overview of the SDSS-IV MaNGA Survey: Mapping nearby Galaxies at Apache Point Observatory. *798*, 1 (Jan. 2015), 7.

[15] Burns, J. O., Hallinan, G., Lux, J., Teitelbaum, L., Kocz, J., MacDowall, R., Bradley, R., Rapetti, D., Wu, W., Furlanetto, S., Austin, A., Romero-Wolf, A., Chang, T.-C., Bowman, J., Kasper, J., Anderson, M., Zhen, Z., Pober, J., and Mirocha, J. NASA Probe Study Report: Farside Array for Radio Science Investigations of the Dark ages and Exoplanets (FARSIDE). *arXiv e-prints* (Nov. 2019), arXiv:1911.08649.

[16] Burns, J. O., Lazio, J., Bale, S., Bowman, J., Bradley, R., Carilli, C., Furlanetto, S., Harker, G., Loeb, A., and Pritchard, J. Probing the first stars and black holes in the early universe with the dark ages radio explorer (dare). *Advances in Space Research 49*, 3 (Feb 2012), 433–450.

[17] Caleb, M., Flynn, C., and Stappers, B. W. Constraining the era of helium reionization using fast radio bursts. *Monthly Notices of the Royal Astronomical Society 485*, 2 (Feb 2019), 2281–2286.

[18] Cheng, Y.-T., Chang, T.-C., and Brock, J. J. Phase-space spectral line deconfusion in intensity mapping.

[19] Cheung, K., Kuo, J.-L., Ng, K.-W., and Tsai, Y.-L. S. The impact of edges 21-cm data on dark matter interactions. *Physics Letters B 789* (Feb 2019), 137–144.

[20] Chianese, M., Di Bari, P., Farrag, K., and Samanta, R. Probing relic neutrino radiative decays with 21 cm cosmology. *Phys. Lett. B 790* (2019), 64–70.

[21] CHIME/FRB Collaboration, Andersen, B. C., Bandura, K. M., Bhardwaj, M., Bij, A., Boyce, M. M., Boyle, P. J., Brar, C., Cassanelli, T., Chawla, P., Chen, T., Cliche, J. F., Cook, A., Cubranic, D., Curtin, A. P., Denman, N. T., Dobbs, M., Dong, F. Q., Fandino, M., Fonseca, E., Gaensler, B. M., Giri, U., Good, D. C., Halpern, M., Hill, A. S., Hinshaw, G. F., Höfer, C., Josephy, A., Kania, J. W., Kaspi, V. M., Landecker,

T. L., LEUNG, C., LI, D. Z., LIN, H. H., MASUI, K. W., MCKINVEN, R., MENA-PARRA, J., MERRYFIELD, M., MEYERS, B. W., MICHILLI, D., MILUTINOVIC, N., MIRHOSSEINI, A., MÜNCHMEYER, M., NAIDU, A., NEWBURGH, L. B., NG, C., PATEL, C., PEN, U. L., PINSONNEAULT-MAROTTE, T., PLEUNIS, Z., QUINE, B. M., RAFIEI-RAVANDI, M., RAHMAN, M., RANSOM, S. M., RENARD, A., SANGHAVI, P., SCHOLZ, P., SHAW, J. R., SHIN, K., SIEGEL, S. R., SINGH, S., SMEGAL, R. J., SMITH, K. M., STAIRS, I. H., TAN, C. M., TENDULKAR, S. P., TRETYAKOV, I., VANDERLINDE, K., WANG, H., WULF, D., AND ZWANIGA, A. V. A bright millisecond-duration radio burst from a Galactic magnetar. *587*, 7832 (Nov. 2020), 54–58.

[22] CHOUDHURY, T. R., HAEHNELT, M. G., AND REGAN, J. Inside-out or outside-in: the topology of reionization in the photon-starved regime suggested by Lyα forest data. *394*, 2 (Apr. 2009), 960–977.

[23] CHUNG, D. T., VIERO, M. P., CHURCH, S. E., AND WECHSLER, R. H. Forecasting [C II] Line-intensity Mapping Measurements between the End of Reionization and the Epoch of Galaxy Assembly. *892*, 1 (Mar. 2020), 51.

[24] CLARK, S. J., DUTTA, B., GAO, Y., MA, Y.-Z., AND STRIGARI, L. E. 21 cm limits on decaying dark matter and primordial black holes. *Phys. Rev. D 98* (Aug 2018), 043006.

[25] CONCERTO COLLABORATION, ADE, P., ARAVENA, M., BARRIA, E., BEELEN, A., BENOIT, A., BÉTHERMIN, M., BOUNMY, J., BOURRION, O., BRES, G., DE BREUCK, C., CALVO, M., CAO, Y., CATALANO, A., DÉSERT, F. X., DURÁN, C. A., FASANO, A., FENOUILLET, T., GARCIA, J., GARDE, G., GOUPY, J., GROPPI, C., HOARAU, C., LAGACHE, G., LAMBERT, J. C., LEGGERI, J. P., LEVY-BERTRAND, F., MACÍAS-PÉREZ, J., MANI, H., MARPAUD, J., MAUSKOPF, P., MONFARDINI, A., PISANO, G., PONTHIEU, N., PRIEUR, L., RONI, S., ROUDIER, S., TOURRES, D., AND TUCKER, C. A wide field-of-view low-resolution spectrometer at APEX: Instrument design and scientific forecast. *642* (Oct. 2020), A60.

[26] CONDON, J. J., AND RANSOM, S. M. *Essential Radio Astronomy*. 2016.

[27] Connor, L. Interpreting the distributions of FRB observables. *487*, 4 (Aug. 2019), 5753–5763.

[28] Connor, L., and Ravi, V. A detection of circumgalactic gas with fast radio bursts, 2021.

[29] Costa, A. A., Landim, R. C. G., Wang, B., and Abdalla, E. Interacting dark energy: possible explanation for 21-cm absorption at cosmic dawn. *The European Physical Journal C 78*, 9 (Sep 2018).

[30] Crites, A. T., Bock, J. J., Bradford, C. M., Chang, T. C., Cooray, A. R., Duband, L., Gong, Y., Hailey-Dunsheath, S., Hunacek, J., Koch, P. M., Li, C. T., O'Brient, R. C., Prouve, T., Shirokoff, E., Silva, M. B., Staniszewski, Z., Uzgil, B., and Zemcov, M. The TIME-Pilot intensity mapping experiment. In *Millimeter, Submillimeter, and Far-Infrared Detectors and Instrumentation for Astronomy VII* (Aug. 2014), W. S. Holland and J. Zmuidzinas, Eds., vol. 9153 of *Society of Photo-Optical Instrumentation Engineers (SPIE) Conference Series*, p. 91531W.

[31] Cyburt, R. H., Fields, B. D., Olive, K. A., and Yeh, T.-H. Big bang nucleosynthesis: Present status. *Reviews of Modern Physics 88*, 1 (Feb 2016).

[32] de Lera Acedo, E. Reach: Radio experiment for the analysis of cosmic hydrogen. In *2019 International Conference on Electromagnetics in Advanced Applications (ICEAA)* (2019), pp. 0626–0629.

[33] de Oliveira-Costa, A., Tegmark, M., Gaensler, B. M., Jonas, J., Landecker, T. L., and Reich, P. A model of diffuse galactic radio emission from 10 mhz to 100 ghz. *Monthly Notices of the Royal Astronomical Society 388*, 1 (Jul 2008), 247–260.

[34] DeBoer, D. R., Parsons, A. R., Aguirre, J. E., Alexander, P., Ali, Z. S., Beardsley, A. P., Bernardi, G., Bowman, J. D., Bradley, R. F., Carilli, C. L., Cheng, C., de Lera Acedo, E., Dillon, J. S., Ewall-Wice, A., Fadana, G., Fagnoni, N., Fritz, R., Furlanetto, S. R., Glendenning, B., Greig, B.,

Grobbelaar, J., Hazelton, B. J., Hewitt, J. N., Hickish, J., Jacobs, D. C., Julius, A., Kariseb, M., Kohn, S. A., Lekalake, T., Liu, A., Loots, A., MacMahon, D., Malan, L., Malgas, C., Maree, M., Martinot, Z., Mathison, N., Matsetela, E., Mesinger, A., Morales, M. F., Neben, A. R., Patra, N., Pieterse, S., Pober, J. C., Razavi-Ghods, N., Ringuette, J., Robnett, J., Rosie, K., Sell, R., Smith, C., Syce, A., Tegmark, M., Thyagarajan, N., Williams, P. K. G., and Zheng, H. Hydrogen Epoch of Reionization Array (HERA). *129*, 974 (Apr. 2017), 045001.

[35] DeBoer, D. R., Parsons, A. R., Aguirre, J. E., Alexander, P., Ali, Z. S., Beardsley, A. P., Bernardi, G., Bowman, J. D., Bradley, R. F., Carilli, C. L., and et al. Hydrogen epoch of reionization array (hera). *Publications of the Astronomical Society of the Pacific 129*, 974 (Mar 2017), 045001.

[36] Dewdney, P. E., Hall, P. J., Schilizzi, R. T., and Lazio, T. J. L. W. The square kilometre array. *Proceedings of the IEEE 97*, 8 (2009), 1482–1496.

[37] Di Matteo, T., Perna, R., Abel, T., and Rees, M. J. Radio Foregrounds for the 21 Centimeter Tomography of the Neutral Intergalactic Medium at High Redshifts. *564*, 2 (Jan. 2002), 576–580.

[38] Dolag, K., Gaensler, B. M., Beck, A. M., and Beck, M. C. Constraints on the distribution and energetics of fast radio bursts using cosmological hydrodynamic simulations. *451*, 4 (Aug. 2015), 4277–4289.

[39] Dumitru, S., Kulkarni, G., Lagache, G., and Haehnelt, M. G. Predictions and sensitivity forecasts for reionization-era [cii] line intensity mapping. *Monthly Notices of the Royal Astronomical Society 485*, 3 (2019), 3486–3498.

[40] Ewall-Wice, A., Chang, T.-C., Lazio, J., Doré, O., Seiffert, M., and Monsalve, R. A. Modeling the radio background from the first black holes at cosmic dawn: Implications for the 21 cm absorption amplitude. *The Astrophysical Journal 868*, 1 (Nov 2018), 63.

[41] Ewall-Wice, A., Chang, T.-C., and Lazio, T. J. W. The radio scream from black holes at cosmic dawn: a semi-analytic model for the impact of radio-loud black holes on the 21cm global signal. *Monthly Notices of the Royal Astronomical Society 492*, 4 (Dec 2019), 6086–6104.

[42] Ewall-Wice, A., Hewitt, J., Mesinger, A., Dillon, J. S., Liu, A., and Pober, J. Constraining high-redshift X-ray sources with next generation 21-cm power spectrum measurements. *458*, 3 (May 2016), 2710–2724.

[43] Fabjan, C. W., Pipkin, F. M., and Silverman, M. Radiofrequency spectroscopy of hydrogen fine structure in $n = 3, 4, 5$. *Phys. Rev. Lett. 26* (Feb 1971), 347–350.

[44] Falkowski, A., and Petraki, K. 21cm absorption signal from charge sequestration, 2018.

[45] Feng, C., and Holder, G. Enhanced global signal of neutral hydrogen due to excess radiation at cosmic dawn. *The Astrophysical Journal 858*, 2 (May 2018), L17.

[46] Fialkov, A., and Barkana, R. Signature of excess radio background in the 21-cm global signal and power spectrum. *Monthly Notices of the Royal Astronomical Society 486*, 2 (Mar 2019), 1763–1773.

[47] Fialkov, A., and Loeb, A. A fast radio burst occurs every second throughout the observable universe. *The Astrophysical Journal 846*, 2 (sep 2017), L27.

[48] Field, G. B. Excitation of the hydrogen 21-cm line. *Proceedings of the IRE 46*, 1 (1958), 240–250.

[49] Foreman-Mackey, D., Hogg, D. W., Lang, D., and Goodman, J. emcee: The MCMC Hammer. *125*, 925 (Mar. 2013), 306.

[50] Friedman, A. On the Possibility of a World wih Constant Negative Curvature of Space. *General Relativity and Gravitation 31* (Dec. 1999), 31–2009.

[51] Furlanetto, S. R., and Oh, S. P. Taxing the rich: recombinations and bubble growth during reionization. *363*, 3 (Nov. 2005), 1031–1048.

[52] Furlanetto, S. R., Peng Oh, S., and Briggs, F. H. Cosmology at low frequencies: The 21cm transition and the high-redshift universe. *Physics Reports 433*, 4-6 (Oct 2006), 181–301.

[53] Furlanetto, S. R., Zaldarriaga, M., and Hernquist, L. The Growth of H II Regions During Reionization. *613*, 1 (Sept. 2004), 1–15.

[54] Gong, Y., Cooray, A., Silva, M., Santos, M. G., Bock, J., Bradford, C. M., and Zemcov, M. Intensity mapping of the [c ii] fine structure line during the epoch of reionization. *The Astrophysical Journal 745*, 1 (Dec 2011), 49.

[55] Gould, R. J. Radiative Hyperfine Transitions. *423* (Mar. 1994), 522.

[56] Hashimoto, T., Goto, T., Lu, T.-Y., On, A. Y. L., Santos, D. J. D., Kim, S. J., Kilerci Eser, E., Ho, S. C. C., Hsiao, T. Y. Y., and Lin, L. Y. W. Revealing the cosmic reionisation history with fast radio bursts in the era of Square Kilometre Array. *arXiv e-prints* (Jan. 2021), arXiv:2101.08798.

[57] Hernandez-Monteagudo, C., Haiman, Z., Jimenez, R., and Verde, L. Oxygen Pumping: Mapping the Reionization Epoch with the CMB. *arXiv e-prints* (Dec. 2006), astro–ph/0612363.

[58] Hills, R., Kulkarni, G., Meerburg, P. D., and Puchwein, E. Concerns about modelling of the edges data. *Nature 564*, 7736 (Dec 2018), E32–E34.

[59] Hirano, S., and Bromm, V. Baryon-dark matter scattering and first star formation. *Monthly Notices of the Royal Astronomical Society: Letters 480*, 1 (Jul 2018), L85–L89.

[60] Hurley-Walker, N., Callingham, J. R., Hancock, P. J., Franzen, T. M. O., Hindson, L., Kapińska, A. D., Morgan, J., Offringa, A. R., Wayth, R. B., Wu, C., Zheng, Q., Murphy, T., Bell, M. E., Dwarakanath, K. S., For, B., Gaensler, B. M., Johnston-Hollitt, M., Lenc, E., Procopio, P., Staveley-Smith, L., Ekers, R., Bowman, J. D., Briggs, F., Cappallo, R. J., Deshpande,

A. A., Greenhill, L., Hazelton, B. J., Kaplan, D. L., Lonsdale, C. J., McWhirter, S. R., Mitchell, D. A., Morales, M. F., Morgan, E., Oberoi, D., Ord, S. M., Prabu, T., Shankar, N. U., Srivani, K. S., Subrahmanyan, R., Tingay, S. J., Webster, R. L., Williams, A., and Williams, C. L. GaLactic and Extragalactic All-sky Murchison Widefield Array (GLEAM) survey - I. A low-frequency extragalactic catalogue. *464*, 1 (Jan. 2017), 1146–1167.

[61] Ioka, K. The Cosmic Dispersion Measure from Gamma-Ray Burst Afterglows: Probing the Reionization History and the Burst Environment. *598*, 2 (Dec. 2003), L79–L82.

[62] Jana, R., Nath, B. B., and Biermann, P. L. Radio background and igm heating due to pop iii supernova explosions. *Monthly Notices of the Royal Astronomical Society 483*, 4 (Dec 2018), 5329–5333.

[63] Janssen, M. A., and Gulkis, S. Mapping the Sky with the COBE Differential Microwave Radiometers. In *The Infrared and Submillimetre Sky after COBE* (Jan. 1992), M. Signore and C. Dupraz, Eds., vol. 359 of *NATO Advanced Study Institute (ASI) Series C*, p. 391.

[64] Jia, L.-B. Dark photon portal dark matter with the 21-cm anomaly. *The European Physical Journal C 79*, 1 (Jan 2019).

[65] Johnston, S., Taylor, R., Bailes, M., Bartel, N., Baugh, C., Bietenholz, M., Blake, C., Braun, R., Brown, J., Chatterjee, S., Darling, J., Deller, A., Dodson, R., Edwards, P., Ekers, R., Ellingsen, S., Feain, I., Gaensler, B., Haverkorn, M., Hobbs, G., Hopkins, A., Jackson, C., James, C., Joncas, G., Kaspi, V., Kilborn, V., Koribalski, B., Kothes, R., Landecker, T., Lenc, E., Lovell, J., Macquart, J. P., Manchester, R., Matthews, D., McClure-Griffiths, N., Norris, R., Pen, U. L., Phillips, C., Power, C., Protheroe, R., Sadler, E., Schmidt, B., Stairs, I., Staveley-Smith, L., Stil, J., Tingay, S., Tzioumis, A., Walker, M., Wall, J., and Wolleben, M. Science with ASKAP.

The Australian square-kilometre-array pathfinder. *Experimental Astronomy 22*, 3 (Dec. 2008), 151–273.

[66] KAPAHI, V. K., AND ANANTHAKRISHNAN, S. Astronomy with the Giant Metrewave Radio Telescope (GMRT). *Bulletin of the Astronomical Society of India 23* (Sept. 1995), 265.

[67] KATZ, J. I. Inferences from the Distributions of Fast Radio Burst Pulse Widths, Dispersion Measures, and Fluences. *818*, 1 (Feb. 2016), 19.

[68] KEATING, L. C., AND PEN, U.-L. Exploring the dispersion measure of the Milky Way halo. *496*, 1 (July 2020), L106–L110.

[69] KERN, N. S., LIU, A., PARSONS, A. R., MESINGER, A., AND GREIG, B. Emulating Simulations of Cosmic Dawn for 21 cm Power Spectrum Constraints on Cosmology, Reionization, and X-Ray Heating. *848*, 1 (Oct. 2017), 23.

[70] KOVETZ, E. D. Line-intensity mapping: 2017 status report. include fig 2 in thesis!!

[71] KOVETZ, E. D. Line-intensity mapping: 2017 status report. include fig 2 in thesis!!

[72] KOVETZ, E. D., CHOLIS, I., AND KAPLAN, D. E. Bounds on ultralight hidden-photon dark matter from observation of the 21 cm signal at cosmic dawn. *Phys. Rev. D 99* (Jun 2019), 123511.

[73] KOVETZ, E. D., POULIN, V., GLUSCEVIC, V., BODDY, K. K., BARKANA, R., AND KAMIONKOWSKI, M. Tighter limits on dark matter explanations of the anomalous edges 21 cm signal. *Phys. Rev. D 98* (Nov 2018), 103529.

[74] KRAMIDA, A. A critical compilation of experimental data on spectral lines and energy levels of hydrogen, deuterium, and tritium. *Atomic Data and Nuclear Data Tables 96*, 6 (2010), 586–644.

[75] KUMAR, P., LU, W., AND BHATTACHARYA, M. Fast radio burst source properties and curvature radiation model. *468*, 3 (July 2017), 2726–2739.

[76] LAWSON, K., AND ZHITNITSKY, A. The 21 cm absorption line and the axion quark nugget dark matter model. *Physics of the Dark Universe 24* (Mar 2019), 100295.

[77] LEHNER, N., WAKKER, B. P., AND SAVAGE, B. D. C II Radiative Cooling of the Diffuse Gas in the Milky Way. *615*, 2 (Nov. 2004), 767–793.

[78] LEMAÎTRE, G. Expansion of the universe, The expanding universe. *91* (Mar. 1931), 490–501.

[79] LEWIS, A., AND CHALLINOR, A. 21 cm angular-power spectrum from the dark ages. *Physical Review D 76*, 8 (Oct 2007).

[80] LINDER, E. V. Detecting helium reionization with fast radio bursts. *Physical Review D 101*, 10 (May 2020).

[81] LINE, J. L. B., MITCHELL, D. A., PINDOR, B., RIDING, J. L., MCKINLEY, B., WEBSTER, R. L., TROTT, C. M., HURLEY-WALKER, N., AND OFFRINGA, A. R. Modelling and peeling extended sources with shapelets: a fornax a case study. *arXiv* (2020).

[82] LIU, A., AND PARSONS, A. R. Constraining cosmology and ionization history with combined 21 cm power spectrum and global signal measurements. *457*, 2 (Apr. 2016), 1864–1877.

[83] LIU, A., AND SHAW, J. R. Data Analysis for Precision 21 cm Cosmology. *132*, 1012 (June 2020), 062001.

[84] LIU, A., AND SHAW, J. R. Data Analysis for Precision 21 cm Cosmology. *132*, 1012 (June 2020), 062001.

[85] LIU, A., AND TEGMARK, M. How well can we measure and understand foregrounds with 21-cm experiments? *Monthly Notices of the Royal Astronomical Society 419*, 4 (2012), 3491–3504.

[86] LIU, A., AND TEGMARK, M. How well can we measure and understand foregrounds with 21-cm experiments? *Monthly Notices of the Royal Astronomical Society 419*, 4 (2012), 3491–3504.

[87] LOEB, A., AND FURLANETTO, S. R. *The First Galaxies in the Universe*. Princeton University Press, 2013.

[88] LOEB, A., AND ZALDARRIAGA, M. Measuring the small-scale power spectrum of cosmic density fluctuations through 21 cm tomography prior to the epoch of structure formation. *Phys. Rev. Lett. 92* (May 2004), 211301.

[89] LORIMER, D. R., BAILES, M., MCLAUGHLIN, M. A., NARKEVIC, D. J., AND CRAWFORD, F. A Bright Millisecond Radio Burst of Extragalactic Origin. *Science 318*, 5851 (Nov. 2007), 777.

[90] LU, W., KUMAR, P., AND ZHANG, B. A unified picture of Galactic and cosmological fast radio bursts. *498*, 1 (Aug. 2020), 1397–1405.

[91] MACQUART, J.-P. Probing the universe's baryons with fast radio bursts, 2018.

[92] MADAU, P., FERGUSON, H. C., DICKINSON, M. E., GIAVALISCO, M., STEIDEL, C. C., AND FRUCHTER, A. High-redshift galaxies in the Hubble Deep Field: colour selection and star formation history to z~4. *283*, 4 (Dec. 1996), 1388–1404.

[93] MADAU, P., AND HAARDT, F. Cosmic Reionization after Planck: Could Quasars Do It All? *813*, 1 (Nov. 2015), L8.

[94] MADAU, P., POZZETTI, L., AND DICKINSON, M. The Star Formation History of Field Galaxies. *498*, 1 (May 1998), 106–116.

[95] MALHOTRA, S., KAUFMAN, M. J., HOLLENBACH, D., HELOU, G., RUBIN, R. H., BRAUHER, J., DALE, D., LU, N. Y., LORD, S., STACEY, G., CONTURSI, A., HUNTER, D. A., AND DINERSTEIN, H. Far-Infrared Spectroscopy of Normal Galaxies: Physical Conditions in the Interstellar Medium. *561*, 2 (Nov. 2001), 766–786.

[96] Mao, Y., Tegmark, M., McQuinn, M., Zaldarriaga, M., and Zahn, O. How accurately can 21 cm tomography constrain cosmology? *Phys. Rev. D 78* (Jul 2008), 023529.

[97] McQuinn, M., Lidz, A., Zahn, O., Dutta, S., Hernquist, L., and Zaldarriaga, M. The morphology of h ii regions during reionization. *Monthly Notices of the Royal Astronomical Society 377*, 3 (May 2007), 1043–1063.

[98] Mesinger, A., Ferrara, A., and Spiegel, D. S. Signatures of X-rays in the early Universe. *431*, 1 (May 2013), 621–637.

[99] Mesinger, A., Furlanetto, S., and Cen, R. 21CMFAST: a fast, seminumerical simulation of the high-redshift 21-cm signal. *411*, 2 (Feb. 2011), 955–972.

[100] Mesinger, A., McQuinn, M., and Spergel, D. N. The kinetic Sunyaev-Zel'dovich signal from inhomogeneous reionization: a parameter space study. *422*, 2 (May 2012), 1403–1417.

[101] Mirabel, I. F., Dijkstra, M., Laurent, P., Loeb, A., and Pritchard, J. R. Stellar black holes at the dawn of the universe. *528* (Apr. 2011), A149.

[102] Miralda-Escudé, J., Haehnelt, M., and Rees, M. J. Reionization of the Inhomogeneous Universe. *530*, 1 (Feb. 2000), 1–16.

[103] Mirocha, J., and Furlanetto, S. R. What does the first highly redshifted 21-cm detection tell us about early galaxies? *Monthly Notices of the Royal Astronomical Society 483*, 2 (Nov 2018), 1980–1992.

[104] Mitridate, A., and Podo, A. Bounds on dark matter decay from 21 cm line. *Journal of Cosmology and Astroparticle Physics 2018*, 05 (May 2018), 069–069.

[105] Morales, M. F., and Wyithe, J. S. B. Reionization and Cosmology with 21-cm Fluctuations. *48* (Sept. 2010), 127–171.

[106] Moroi, T., Nakayama, K., and Tang, Y. Axion-photon conversion and effects on 21 cm observation. *Physics Letters B 783* (Aug 2018), 301–305.

[107] Muñoz, J. B., Ali-Haïmoud, Y., and Kamionkowski, M. Primordial non-gaussianity from the bispectrum of 21-cm fluctuations in the dark ages. *Phys. Rev. D 92* (Oct 2015), 083508.

[108] Muñoz, J. B., Dvorkin, C., and Loeb, A. 21-cm fluctuations from charged dark matter. *Phys. Rev. Lett. 121* (Sep 2018), 121301.

[109] Muñoz, J. B., and Loeb, A. A small amount of mini-charged dark matter could cool the baryons in the early Universe. *Nature 557*, 7707 (2018), 684.

[110] Nan, R., Li, D., Jin, C., Wang, Q., Zhu, L., Zhu, W., Zhang, H., Yue, Y., and Qian, L. The Five-Hundred Aperture Spherical Radio Telescope (fast) Project. *International Journal of Modern Physics D 20*, 6 (Jan. 2011), 989–1024.

[111] Newburgh, L. B., Bandura, K., Bucher, M. A., Chang, T. C., Chiang, H. C., Cliche, J. F., Davé, R., Dobbs, M., Clarkson, C., Ganga, K. M., Gogo, T., Gumba, A., Gupta, N., Hilton, M., Johnstone, B., Karastergiou, A., Kunz, M., Lokhorst, D., Maartens, R., Macpherson, S., Mdlalose, M., Moodley, K., Ngwenya, L., Parra, J. M., Peterson, J., Recnik, O., Saliwanchik, B., Santos, M. G., Sievers, J. L., Smirnov, O., Stronkhorst, P., Taylor, R., Vanderlinde, K., Van Vuuren, G., Weltman, A., and Witzemann, A. HIRAX: a probe of dark energy and radio transients. In *Ground-based and Airborne Telescopes VI* (Aug. 2016), H. J. Hall, R. Gilmozzi, and H. K. Marshall, Eds., vol. 9906 of *Society of Photo-Optical Instrumentation Engineers (SPIE) Conference Series*, p. 99065X.

[112] Niino, Y. Fast Radio Bursts' Recipes for the Distributions of Dispersion Measures, Flux Densities, and Fluences. *858*, 1 (May 2018), 4.

[113] Osterbrock, D. E. *Astrophysics of gaseous nebulae and active galactic nuclei*. 1989.

[114] Ota, K., Iye, M., Kashikawa, N., Konno, A., Nakata, F., Totani, T., Kobayashi, M. A. R., Fudamoto, Y., Seko, A., Toshikawa, J., and et al. A new constraint on reionization from the evolution of the lyluminosity function atz

6–7 probed by a deep census ofz= 7.0 lyemitter candidates to 0.3l*. *The Astrophysical Journal 844*, 1 (Jul 2017), 85.

[115] PAGANO, M., AND FRONENBERG, H. Constraining the epoch of reionization with highly dispersed fast radio bursts. *Monthly Notices of the Royal Astronomical Society 505*, 2 (May 2021), 2195–2206.

[116] PAGANO, M., AND LIU, A. Quantifying density-ionization correlations with the 21-cm power spectrum. *498*, 1 (Aug. 2020), 373–384.

[117] PARK, J., MESINGER, A., GREIG, B., AND GILLET, N. Inferring the astrophysics of reionization and cosmic dawn from galaxy luminosity functions and the 21-cm signal. *484*, 1 (Mar. 2019), 933–949.

[118] PARSONS, A., POBER, J., MCQUINN, M., JACOBS, D., AND AGUIRRE, J. A SENSITIVITY AND ARRAY-CONFIGURATION STUDY FOR MEASURING THE POWER SPECTRUM OF 21 cm EMISSION FROM REIONIZATION. *The Astrophysical Journal 753*, 1 (jun 2012), 81.

[119] PEEBLES, P. J. E. The natural science of cosmology. *Journal of Physics: Conference Series 484* (Mar 2014), 012001.

[120] PERLMUTTER, S., ALDERING, G., GOLDHABER, G., KNOP, R. A., NUGENT, P., CASTRO, P. G., DEUSTUA, S., FABBRO, S., GOOBAR, A., GROOM, D. E., HOOK, I. M., KIM, A. G., KIM, M. Y., LEE, J. C., NUNES, N. J., PAIN, R., PENNYPACKER, C. R., QUIMBY, R., LIDMAN, C., ELLIS, R. S., IRWIN, M., MCMAHON, R. G., RUIZ-LAPUENTE, P., WALTON, N., SCHAEFER, B., BOYLE, B. J., FILIPPENKO, A. V., MATHESON, T., FRUCHTER, A. S., PANAGIA, N., NEWBERG, H. J. M., COUCH, W. J., AND PROJECT, T. S. C. Measurements of Ω and Λ from 42 High-Redshift Supernovae. *517*, 2 (June 1999), 565–586.

[121] PETROFF, E., BARR, E. D., JAMESON, A., KEANE, E. F., BAILES, M., KRAMER, M., MORELLO, V., TABBARA, D., AND VAN STRATEN, W. FRBCAT: The Fast Radio Burst Catalogue. *33* (Sept. 2016), e045.

[122] Philip, L., Abdurashidova, Z., Chiang, H. C., Ghazi, N., Gumba, A., Heilgendorff, H. M., Hickish, J., Jáuregui-García, J. M., Malepe, K., Nunhokee, C. D., Peterson, J., Sievers, J. L., Simes, V., and Spann, R. Probing radio intensity at high-z from marion: 2017 instrument, 2018.

[123] Planck Collaboration, Ade, P. A. R., Aghanim, N., Arnaud, M., Ashdown, M., Aumont, J., Baccigalupi, C., Banday, A. J., Barreiro, R. B., Bartlett, J. G., Bartolo, N., Battaner, E., Battye, R., Benabed, K., Benoît, A., Benoit-Lévy, A., Bernard, J. P., Bersanelli, M., Bielewicz, P., Bock, J. J., Bonaldi, A., Bonavera, L., Bond, J. R., Borrill, J., Bouchet, F. R., Boulanger, F., Bucher, M., Burigana, C., Butler, R. C., Calabrese, E., Cardoso, J. F., Catalano, A., Challinor, A., Chamballu, A., Chary, R. R., Chiang, H. C., Chluba, J., Christensen, P. R., Church, S., Clements, D. L., Colombi, S., Colombo, L. P. L., Combet, C., Coulais, A., Crill, B. P., Curto, A., Cuttaia, F., Danese, L., Davies, R. D., Davis, R. J., de Bernardis, P., de Rosa, A., de Zotti, G., Delabrouille, J., Désert, F. X., Di Valentino, E., Dickinson, C., Diego, J. M., Dolag, K., Dole, H., Donzelli, S., Doré, O., Douspis, M., Ducout, A., Dunkley, J., Dupac, X., Efstathiou, G., Elsner, F., Ensslin, T. A., Eriksen, H. K., Farhang, M., Fergusson, J., Finelli, F., Forni, O., Frailis, M., Fraisse, A. A., Franceschi, E., Frejsel, A., Galeotta, S., Galli, S., Ganga, K., Gauthier, C., Gerbino, M., Ghosh, T., Giard, M., Giraud-Héraud, Y., Giusarma, E., Gjerløw, E., González-Nuevo, J., Górski, K. M., Gratton, S., Gregorio, A., Gruppuso, A., Gudmundsson, J. E., Hamann, J., Hansen, F. K., Hanson, D., Harrison, D. L., Helou, G., Henrot-Versillé, S., Hernández-Monteagudo, C., Herranz, D., Hildebrand t, S. R., Hivon, E., Hobson, M., Holmes, W. A., Hornstrup, A., Hovest, W., Huang, Z., Huffenberger, K. M., Hurier, G., Jaffe, A. H., Jaffe, T. R., Jones, W. C., Juvela, M., Keihänen, E., Keskitalo, R., Kisner, T. S., Kneissl, R., Knoche, J., Knox, L., Kunz, M., Kurki-Suonio, H., Lagache, G., Lähteenmäki, A., Lamarre, J. M., Lasenby, A., Lattanzi, M.,

Lawrence, C. R., Leahy, J. P., Leonardi, R., Lesgourgues, J., Levrier, F., Lewis, A., Liguori, M., Lilje, P. B., Linden-Vørnle, M., López-Caniego, M., Lubin, P. M., Macías-Pérez, J. F., Maggio, G., Maino, D., Mandolesi, N., Mangilli, A., Marchini, A., Maris, M., Martin, P. G., Martinelli, M., Martínez-González, E., Masi, S., Matarrese, S., McGehee, P., Meinhold, P. R., Melchiorri, A., Melin, J. B., Mendes, L., Mennella, A., Migliaccio, M., Millea, M., Mitra, S., Miville-Deschênes, M. A., Moneti, A., Montier, L., Morgante, G., Mortlock, D., Moss, A., Munshi, D., Murphy, J. A., Naselsky, P., Nati, F., Natoli, P., Netterfield, C. B., Nørgaard-Nielsen, H. U., Noviello, F., Novikov, D., Novikov, I., Oxborrow, C. A., Paci, F., Pagano, L., Pajot, F., Paladini, R., Paoletti, D., Partridge, B., Pasian, F., Patanchon, G., Pearson, T. J., Perdereau, O., Perotto, L., Perrotta, F., Pettorino, V., Piacentini, F., Piat, M., Pierpaoli, E., Pietrobon, D., Plaszczynski, S., Pointecouteau, E., Polenta, G., Popa, L., Pratt, G. W., Prézeau, G., Prunet, S., Puget, J. L., Rachen, J. P., Reach, W. T., Rebolo, R., Reinecke, M., Remazeilles, M., Renault, C., Renzi, A., Ristorcelli, I., Rocha, G., Rosset, C., Rossetti, M., Roudier, G., Rouillé d'Orfeuil, B., Rowan-Robinson, M., Rubiño-Martín, J. A., Rusholme, B., Said, N., Salvatelli, V., Salvati, L., Sandri, M., Santos, D., Savelainen, M., Savini, G., Scott, D., Seiffert, M. D., Serra, P., Shellard, E. P. S., Spencer, L. D., Spinelli, M., Stolyarov, V., Stompor, R., Sudiwala, R., Sunyaev, R., Sutton, D., Suur-Uski, A. S., Sygnet, J. F., Tauber, J. A., Terenzi, L., Toffolatti, L., Tomasi, M., Tristram, M., Trombetti, T., Tucci, M., Tuovinen, J., Türler, M., Umana, G., Valenziano, L., Valiviita, J., Van Tent, F., Vielva, P., Villa, F., Wade, L. A., Wandelt, B. D., Wehus, I. K., White, M., White, S. D. M., Wilkinson, A., Yvon, D., Zacchei, A., and Zonca, A. Planck 2015 results. XIII. Cosmological parameters. *594* (Sept. 2016), A13.

[124] PLATTS, E., WELTMAN, A., WALTERS, A., TENDULKAR, S., GORDIN, J., AND KANDHAI, S. A living theory catalogue for fast radio bursts. *Physics Reports 821* (Aug 2019), 1–27.

[125] PLEUNIS, Z., MICHILLI, D., BASSA, C. G., HESSELS, J. W. T., NAIDU, A., ANDERSEN, B. C., CHAWLA, P., FONSECA, E., GOPINATH, A., KASPI, V. M., KONDRATIEV, V. I., LI, D. Z., BHARDWAJ, M., BOYLE, P. J., BRAR, C., CASSANELLI, T., GUPTA, Y., JOSEPHY, A., KARUPPUSAMY, R., KEIMPEMA, A., KIRSTEN, F., LEUNG, C., MARCOTE, B., MASUI, K., MCKINVEN, R., MEYERS, B. W., NG, C., NIMMO, K., PARAGI, Z., RAHMAN, M., SCHOLZ, P., SHIN, K., SMITH, K. M., STAIRS, I. H., AND TENDULKAR, S. P. Lofar detection of 110-188 mhz emission and frequency-dependent activity from frb 20180916b, 2020.

[126] POBER, J. C., LIU, A., DILLON, J. S., AGUIRRE, J. E., BOWMAN, J. D., BRADLEY, R. F., CARILLI, C. L., DEBOER, D. R., HEWITT, J. N., JACOBS, D. C., AND ET AL. What next-generation 21 cm power spectrum measurements can teach us about the epoch of reionization. *The Astrophysical Journal 782*, 2 (Jan 2014), 66.

[127] POBER, J. C., LIU, A., DILLON, J. S., AGUIRRE, J. E., BOWMAN, J. D., BRADLEY, R. F., CARILLI, C. L., DEBOER, D. R., HEWITT, J. N., JACOBS, D. C., MCQUINN, M., MORALES, M. F., PARSONS, A. R., TEGMARK, M., AND WERTHIMER, D. J. What Next-generation 21 cm Power Spectrum Measurements can Teach us About the Epoch of Reionization. *782*, 2 (Feb. 2014), 66.

[128] POPPING, G., KAMPEN, E. V., DECARLI, R., SPAANS, M., SOMERVILLE, R. S., AND TRAGER, S. C. Sub-mm emission line deep fields: Co and [cii] luminosity functions out to z = 6. *arXiv 461*, 1 (2016), 93–110.

[129] PRICE, D., GREENHILL, L., FIALKOV, A., BERNARDI, G., GARSDEN, H., BARSDELL, B., KOCZ, J., ANDERSON, M., BOURKE, S., DEXTER, M., DOWELL, J., CRAIG, J., EASTWOOD, M., EFTEKHARI, T., ELLINGSON, S., HALLINAN, G., HARTMAN, J., LAZIO, T., MACMAHON, D., AND WOODY, D. Design and charac-

terization of the large-aperture experiment to detect the dark age (leda) radiometer systems. *Monthly Notices of the Royal Astronomical Society 478* (09 2017).

[130] PRITCHARD, J. R., AND LOEB, A. 21 cm cosmology in the 21st century. *Reports on Progress in Physics 75*, 8 (Jul 2012), 086901.

[131] PROCHASKA, J. X., AND NEELEMAN, M. The astrophysical consequences of intervening galaxy gas on fast radio bursts. *474*, 1 (Feb. 2018), 318–325.

[132] ROBERTSON, H. P. Relativistic Cosmology. *Reviews of Modern Physics 5*, 1 (Jan. 1933), 62–90.

[133] SAFARZADEH, M., SCANNAPIECO, E., AND BABUL, A. A limit on the warm dark matter particle mass from the redshifted 21 cm absorption line. *The Astrophysical Journal 859*, 2 (May 2018), L18.

[134] SCHECHTER, P. An analytic expression for the luminosity function for galaxies. *203* (Jan. 1976), 297–306.

[135] SCHNEIDER, A. Constraining noncold dark matter models with the global 21-cm signal. *Phys. Rev. D 98* (Sep 2018), 063021.

[136] SCOTT, D., AND REES, M. J. The 21-cm line at high redshift: a diagnostic for the origin of large scale structure. *247* (Dec. 1990), 510.

[137] SHARMA, P. Astrophysical radio background cannot explain the edges 21-cm signal: constraints from cooling of non-thermal electrons. *Monthly Notices of the Royal Astronomical Society: Letters 481*, 1 (Aug 2018), L6–L10.

[138] SILK, J. Cosmic Black-Body Radiation and Galaxy Formation. *151* (Feb. 1968), 459.

[139] SINGH, S., AND SUBRAHMANYAN, R. The redshifted 21 cm signal in the edges low-band spectrum. *The Astrophysical Journal 880*, 1 (Jul 2019), 26.

[140] SINGH, S., SUBRAHMANYAN, R., SHANKAR, N. U., RAO, M. S., GIRISH, B. S., RAGHUNATHAN, A., SOMASHEKAR, R., AND SRIVANI, K. S. Saras 2: a spectral ra-

diometer for probing cosmic dawn and the epoch of reionization through detection of the global 21-cm signal. *Experimental Astronomy 45*, 2 (Apr 2018), 269–314.

[141] SLATYER, T. R., AND WU, C.-L. Early-universe constraints on dark matter-baryon scattering and their implications for a global 21 cm signal. *Phys. Rev. D 98* (Jul 2018), 023013.

[142] SOBACCHI, E., AND MESINGER, A. The clustering of Lyman α emitters at z $\approx$ 7: implications for reionization and host halo masses. *453*, 2 (Oct. 2015), 1843–1854.

[143] SOKOLOWSKI, M., TREMBLAY, S. E., WAYTH, R. B., TINGAY, S. J., CLARKE, N., ROBERTS, P., WATERSON, M., EKERS, R. D., HALL, P., LEWIS, M., AND ET AL. Bighorns - broadband instrument for global hydrogen reionisation signal. *Publications of the Astronomical Society of Australia 32* (2015).

[144] SPITZER, L. *Physical processes in the interstellar medium*. 1978.

[145] SUGINOHARA, M., SUGINOHARA, T., AND SPERGEL, D. N. Detecting z¿10 Objects through Carbon, Nitrogen, and Oxygen Emission Lines. *512*, 2 (Feb. 1999), 547–552.

[146] SUN, G., HENSLEY, B. S., CHANG, T.-C., DORÉ, O., AND SERRA, P. A self-consistent framework for multiline modeling in line intensity mapping experiments. *The Astrophysical Journal 887*, 2 (Dec 2019), 142.

[147] SUNYAEV, R. A., AND ZELDOVICH, Y. B. Small-Scale Fluctuations of Relic Radiation. *7*, 1 (Apr. 1970), 3–19.

[148] TAYAL, S. S. Electron impact excitation collision strength for transitions in C II. *486*, 2 (Aug. 2008), 629–636.

[149] TEGMARK, M. How to Make Maps from Cosmic Microwave Background Data without Losing Information. *480*, 2 (May 1997), L87–L90.

[150] TEGMARK, M., EISENSTEIN, D. J., HU, W., AND DE OLIVEIRA-COSTA, A. Foregrounds and forecasts for the cosmic microwave background. *The Astrophysical Journal 530*, 1 (Feb 2000), 133–165.

[151] TEGMARK, M., EISENSTEIN, D. J., STRAUSS, M. A., WEINBERG, D. H., BLANTON, M. R., FRIEMAN, J. A., FUKUGITA, M., GUNN, J. E., HAMILTON, A. J. S., KNAPP, G. R., AND ET AL. Cosmological constraints from the sdss luminous red galaxies. *Physical Review D 74*, 12 (Dec 2006).

[152] TEGMARK, M., AND ZALDARRIAGA, M. Fast fourier transform telescope. *Phys. Rev. D 79* (Apr 2009), 083530.

[153] TENDULKAR, S. P., BASSA, C. G., CORDES, J. M., BOWER, G. C., LAW, C. J., CHATTERJEE, S., ADAMS, E. A. K., BOGDANOV, S., BURKE-SPOLAOR, S., BUTLER, B. J., DEMOREST, P., HESSELS, J. W. T., KASPI, V. M., LAZIO, T. J. W., MADDOX, N., MARCOTE, B., MCLAUGHLIN, M. A., PARAGI, Z., RANSOM, S. M., SCHOLZ, P., SEYMOUR, A., SPITLER, L. G., VAN LANGEVELDE, H. J., AND WHARTON, R. S. The Host Galaxy and Redshift of the Repeating Fast Radio Burst FRB 121102. *834*, 2 (Jan. 2017), L7.

[154] VAN HAARLEM, M. P., WISE, M. W., GUNST, A. W., HEALD, G., MCKEAN, J. P., HESSELS, J. W. T., DE BRUYN, A. G., NIJBOER, R., SWINBANK, J., FALLOWS, R., AND ET AL. Lofar: The low-frequency array. *Astronomy Astrophysics 556* (Jul 2013), A2.

[155] VANDERLINDE, K., LIU, A., GAENSLER, B., BOND, D., HINSHAW, G., NG, C., CHIANG, C., STAIRS, I., BROWN, J.-A., SIEVERS, J., MENA, J., SMITH, K., BANDURA, K., MASUI, K., SPEKKENS, K., BELOSTOTSKI, L., DOBBS, M., TUROK, N., BOYLE, P., RUPEN, M., LANDECKER, T., PEN, U.-L., AND KASPI, V. The Canadian Hydrogen Observatory and Radio-transient Detector (CHORD). In *Canadian Long Range Plan for Astronomy and Astrophysics White Papers* (Oct. 2019), vol. 2020, p. 28.

[156] VOYTEK, T. C., NATARAJAN, A., JÁUREGUI GARCÍA, J. M., PETERSON, J. B., AND LÓPEZ-CRUZ, O. Probing the dark ages at z 20: The sci-hi 21 cm all-sky spectrum experiment. *The Astrophysical Journal 782*, 1 (Jan 2014), L9.

[157] WALKER, A. G. On Milne's Theory of World-Structure. *Proceedings of the London Mathematical Society 42* (Jan. 1937), 90–127.

[158] WALTERS, A., MA, Y.-Z., SIEVERS, J., AND WELTMAN, A. Probing diffuse gas with fast radio bursts. *100*, 10 (Nov. 2019), 103519.

[159] WALTERS, A., WELTMAN, A., GAENSLER, B. M., MA, Y.-Z., AND WITZEMANN, A. Future cosmological constraints from fast radio bursts. *The Astrophysical Journal 856*, 1 (2018), 65.

[160] WANG, X., TEGMARK, M., SANTOS, M. G., AND KNOX, L. 21 cm Tomography with Foregrounds. *650*, 2 (Oct. 2006), 529–537.

[161] WATKINSON, C. A., MESINGER, A., PRITCHARD, J. R., AND SOBACCHI, E. 21-cm signatures of residual H I inside cosmic H II regions during reionization. *449*, 3 (May 2015), 3202–3211.

[162] WATKINSON, C. A., AND PRITCHARD, J. R. Distinguishing models of reionization using future radio observations of 21-cm 1-point statistics. *443*, 4 (Oct. 2014), 3090–3106.

[163] WIESE, W. L., AND FUHR, J. R. Accurate atomic transition probabilities for hydrogen, helium, and lithium. *Journal of Physical and Chemical Reference Data 38*, 3 (2009), 565–720.

[164] WOUTHUYSEN, S. A. On the excitation mechanism of the 21-cm (radio-frequency) interstellar hydrogen emission line. *57* (Jan. 1952), 31–32.

[165] YOSHIURA, S., AND TAKAHASHI, K. The variance of dispersion measure of high-redshift transient objects as a probe of ionized bubble size during reionization. *473*, 2 (Jan. 2018), 1570–1575.

[166] ZHANG, Z. J., YAN, K., LI, C. M., ZHANG, G. Q., AND WANG, F. Y. Intergalactic Medium Dispersion Measures of Fast Radio Bursts Estimated from IllustrisTNG Simulation and Their Cosmological Applications. *906*, 1 (Jan. 2021), 49.

[167] ZHENG, H., TEGMARK, M., DILLON, J. S., KIM, D. A., LIU, A., NEBEN, A. R., JONAS, J., REICH, P., AND REICH, W. An improved model of diffuse galactic radio

emission from 10 mhz to 5 thz. *Monthly Notices of the Royal Astronomical Society 464*, 3 (Oct 2016), 3486–3497.

[168] ZHENG, Z., OFEK, E. O., KULKARNI, S. R., NEILL, J. D., AND JURIC, M. Probing the intergalactic medium with fast radio bursts. *The Astrophysical Journal 797*, 1 (Nov 2014), 71.